Different approaches to determine the composition of the ultra-high energy cosmic rays in the Pierre Auger Observatory

Miguel Blanco Otano

Thèse de doctorat
de l'**Université Pierre et Marie Curie (UPMC)**

Laboratoire de Physique Nucléaire et des Hautes Énergies (LPNHE)

presenté par
Miguel Blanco Otano

Pour obtenir le grade de
DOCTEUR DÈS SCIENCES DE L'UNIVERSITÉ PIERRE ET MARIE CURIE (UPMC)

Different approaches to determine the composition of the ultra-high energy cosmic rays in the Pierre Auger Observatory

Directeur de thèse: **Antoine Letessier-Selvon**
Codirectrice de thèse: **Piera Luisa Ghia**

Membres du jury de soutenance:

Corinne Berat	(rapporteuse)
Sergio Navas Concha	(rapporteur)
Jean-Pierre Lees	(examinateur)
Jean-Paul Tavernet	(examinateur)
Antoine Letessier-Selvon	(invité, directeur de thèse)

Edition for the PhD thesis defense (12/12/2014). Paris. Friday 5th December, 2014.

Para Helia.
Para Abel.

Acknowledgements

This PhD thesis is the final stage of a process that has known many different stages. It is impossible to thank as they deserve to all the people that have carried me here, but it is worthy to try.

Je veux remercier Antoine Letessier-Selvon qui m'a donné l'opportunité de connaître en profondeur une profession intéressante, libre, et qui nous permet de maintenir la tête active. Sans peut être même le savoir, il m'a appris aussi la passion avec laquelle on doit aimer ce travail. Je ne suis probablement pas le doctorant qui est arrivé le plus loin, mais peut être celui qui a parcouru le plus de chemin.

Un grand merci à Pierre Billoir. J'ai appris de chaque pas qu'il fait, de chacun de ses raisonnements, de chaque code, de chaque conversation à la cantine, et de sa pensée fraiche, intuitive, et courageuse. Merci aussi à Piera Luisa Ghia, pour le dernier sprint qu'elle a courru avec moi pour arriver à temps et améliorer ce manuscrit.

Merci à mes collegues Mariangela, Ioana et Romain avec lesquels j'ai été ravi de travailler et de qui j'ai appris tous les jours. Merci à Moritz, Lorenzo, Julien et Carla de faire partie de cette belle famille. Et merci aussi à Jules et Tania pour votre soutien ces derniers mois.

Es fundamental agradecer a mis padres el apoyo y empuje que de ellos he recibido en cada momento, ayudándome a mantener el objetivo claro y la brújula siempre bien calibrada, durante estos últimos tres años, pero sobre todo también durante los 30 previos.

Por último, unas gracias infinitas a mi editora personal en este trabajo, compañera y, sobre todo, amiga. Sin ella y sus enormes sacrificios, estos tres años en el exilio se hubieran hecho infinitamente más difíciles. Espero poder devolverte todo esto algún día. Gracias Noelia de todo corazón.

In any case, even if this is the final stage of a period in my life, it is just the beginning a new period. I am sure that I will widely benefit from the many lessons I am taking from here. Nothing less than to thank again those that have been by my side in these three years, far or near, at the office or at home, in France, Spain, or Argentina.

Miguel Blanco Otano.
París, 29 de octubre de 2014.

Summary

"Millions of dollars and years of experimental physics can ruin a theory that took a whole afternoon to develop".
Rocky Kolb, ISAAP 2012.

The ultra-high energy cosmic rays are particles that, coming from outside the solar system, arrive at Earth with energies up to 10^{20} eV. The study of these particles can help to disentangle their origin, knowing more about distant objects that create or accelerate them, and the interactions in their path to the Earth. Besides, as they arrive at Earth with enormous energy, they are also relevant in the field of particle physics.

Cosmic rays are charged nuclei, although their by-products, like photons and neutrinos produced in their interactions at the source or with interstellar radiation and matter, are also a subject of study. The number of these particles arriving at Earth decreases dramatically with the energy. At the highest energies, those of interest in this study, only $1\,\mathrm{km}^{-2}\mathrm{century}^{-1}$ are observed. When one of these cosmic rays enters in the atmosphere of the Earth, it interacts with the atoms or nuclei in the air generating a lot of secondary particles. These secondary particles constitute an extensive air shower. This effect blurs the characteristics of the primary particle making difficult the analysis to determine its energy, mass and arrival direction. At the same time, this is the only way by which this scarce and energetic natural phenomenon can be measured, as the atmosphere plays the role of a calorimeter and spreads the effect from a single point to a large area, allowing its detection.

To detect the extensive air showers and, finally, the ultra-high energy cosmic rays, with a significantly large statistic, large observatories have been constructed in the last decades. The Pierre Auger Observatory, on which this PhD thesis is focused, is the largest in the world. It is located in Argentina, province of Mendoza, near the town of Malargüe, and it is placed at 1400 m above sea level. It was completed in 2008 but the data collection started in 2004. It is the first observatory combining two techniques for measuring cosmic rays, collecting data both with a surface detector array and a fluorescence detector. The former is an array of water Cherenkov detectors spread over a flat surface of $3000\,\mathrm{km}^2$ and the latter are 4 buildings at the edges of the array, facing the interior, with 6 fluorescence telescopes in each one. These two techniques measure the two profiles of the extensive air showers: the lateral profile, that samples the shower at a determined height, and the longitudinal profile, that tracks the development of the shower through the atmosphere. Different techniques of detection are explored. These techniques allow to determine different characteristics of the extensive air shower and, consequently, of the primary cosmic ray that enters in the atmosphere. Despite the great evolution in the last century concerning these techniques, the complete description

of the arriving particles has not yet been achieved. The composition of the primary particle is currently based on measurements of the longitudinal profile, and the atmospheric depth of maximum ($X_{\max}$) observed in this profile. These measurements are done with the fluorescence technique, that needs special luminosity conditions that reduce the exposure time to about 10% of the time. In a full duty cycle, the mass of the primary particle (composition) is difficult to infer. Other methods, based on the measure of $X_{\max}$ or related observables, like the muonic atmospheric depth of maximum ($X^{\mu}_{\max}$), by alternative methods, or the measure of the muon number (also related with the mass of the primary) are not, up to now, developed enough to resolve the question. Furthermore, the step from the measured $X_{\max}$ to the mass of the primary is based on hadronic interaction models at energies higher than those reached in accelerator experiments, like the Large Hadron Collider (LHC).

The measurements done by the Pierre Auger Observatory and similar observatories have shed some light on some of the questions mentioned above. A suppression in the cosmic rays spectrum has been found at the energy of 4×10^{19} eV. Nevertheless, an agreement in the interpretation of this suppression has not yet been achieved. Although interactions of the travelling particles with the cosmic microwave background has been proposed as a cause, other interpretations, like the exhaustion of sources, is still possible. Other features in the energy spectrum have been observed, and different interpretations are also in dispute. In addition, different studies have been carried out searching for anisotropy in the arrival directions at different scales, but still no statistically significant evidence has been found. The composition measurements done by Auger, based on the measure of the $X_{\max}$ by the fluorescence telescopes, reveal a heavy component in the ultra-high energy part of the spectrum, that is in some tension with the composition previously measured by other observatories.

The different interpretations for the suppression, the other features in the spectrum, and a better evaluation of the origin needs more precise measurements of the composition of the cosmic rays. The short duty cycle of the fluorescence technique is the main limitation.

Motivation

The main motivation of this PhD thesis is to improve the capabilities to determine the mass composition of the ultra-high energy cosmic rays in the Pierre Auger Observatory, and other cosmic rays observatories. Very important results and unique information about ultra-high energy cosmic rays have been published by Auger in the last decade, but a correct interpretation of these results needs for a measurement of the composition of the detected cosmic rays. We certainly consider that an improvement in the composition identification capabilities of the Pierre Auger Observatory is achievable, so three different approaches to this challenge are proposed in this PhD thesis. They do not cover all the possibilities for the future of the Pierre Auger Observatory and other cosmic ray experiments, but they cover the three main ways this challenge can be faced.

New analysis

The first approach is to use the Auger data collected so far to make new analysis that can yield new results. Horizontal air showers are composed mostly by muons, as other components of the shower, like the electromagnetic one, are absorbed in the atmosphere. Muons, in their

trajectory to the ground, are deviated by the magnetic field of the Earth. This deflection is reflected in the shape of the ground footprint of the shower and it can be measured. The measured deflection is found to be related with different characteristics of the extensive air shower, like the $X^{\mu}_{\max}$ and the transverse momentum of the muons in their development in the atmosphere. It is possible, then, to construct an estimator to obtain, with this alternative method, another measure of $X^{\mu}_{\max}$. Besides, the hadronic interaction models can be checked and compared with the data, by analysing the transverse momentum.

This new analysis is detailed in chapter 4.

Detector improvement

The second approach is to improve the actual observatory, by adding a detector that can obtain information about the longitudinal profile of the extensive air shower with a 100% duty cycle. This can give the Pierre Auger Observatory (and similar observatories) the capability to measure mass sensitive parameters for the whole data set. The detection of the radio emission produced in the extensive air showers has been suggested as a possible technique. Different processes of emission are described, and some of them are explored. Among them, the detection of the Molecular Bremsstrahlung Radiation (MBR) emission is found as the most promising technique. Different tests have been and are being done by the EASIER group, in which part of this PhD thesis is framed. The Extensive Air Shower Identification using Electron Radiometer (EASIER) project aims to detect the radio emissions of the extensive air showers by installing antennae in the water Cherenkov detectors of the surface detector array of the Pierre Auger Observatory.

The possibilities of the radio detection technique are discussed in chapter 5.

A new detector

The third approach is to reconsider the Pierre Auger Observatory from the scratch, by changing the used detector in the surface array. A modification to the surface detector array is proposed, by dividing the water Cherenkov detectors into two different water volumes. This new detector obtains different responses in each volume to different components of the extensive air shower: electromagnetic and muonic. The access to the muonic component is another way to access the composition of the primary particle, and different observables can be obtained to this purpose. The performance of this new detector and a preliminary idea of its achievements in the discrimination between different primaries are described.

This new detector is described in chapter 6.

Outlook

The main purpose of this PhD thesis was to explore new helpful ways to identify the composition of the cosmic rays at the highest energies. The results shown in this work prove the validity of the methods and the detectors proposed, and they do not have the intention to establish any new description of the characteristics of the ultra-high energy cosmic rays. Nevertheless, we believe that a future application of the described methods and the development on large scale

of the proposed detectors can yield very promising results. However, this application needs deeper work that goes beyond the scope of this PhD thesis in terms of both time and human resources.

Contents

Historical prologue

At the beginning of this PhD thesis, in 2012, the 100th anniversary of the discovery of cosmic rays was being celebrated in several countries. The knowledge of the cosmic rays has strongly grown since the earliest experiments. However, many questions remain still open.

During the first years of the 20th century, the ionization of the air was attributed to an effect of the fascinating new discovery of the radioactive elements in the Earth. Some experiments in that first decade supported this theory. But in 1909 Theodor Wulf used his own electrometer to measure the levels of radiation both at the top of the Eiffel Tower and at its base: he did find a decrease at the top, but not as big as predicted [1]. Two years later, Domenico Pacini also measured the ionization rates over a lake, over the sea, and at 3 m depth under the surface, finding different ionization rates at each place [2]. The decrement of the ionization found under the water led him to think about other possible sources rather than the radioactivity of the Earth.

Victor Hess followed the Wulf and Pacini ideas, but increasing the height of the measurements up to 5 km. In 1912, Hess published a study in the Proceedings of the Viennese Academy of Sciences [3] describing the measurements done with three Wulf electrometers shipped in a hot air balloon. The main conclusion of this study was that it existed a radiation which was originated outside the Earth. Besides, this radiation was present day and night, discarding the sun as possible source. Robert A. Millikan confirmed the conclusions presented by Hess a few years later, naming this radiation as cosmic rays, using the term for the first time in a lecture to the British Association at the University of Leeds in 1926 [4].

Despite the great achievements of the time like this discovery or the development of the quantum revolution, not a lot of attention was put in the field of modern physics, taking into account the number of publications in the field [5]. The interest in cosmic rays became intense only in the 1930s. At some point in this decade, different teams were working on identifying a charged particle registered in the cosmic rays experiments, with a mass between the electron and the proton. Even if most of those teams discovered the new particle, named muon a few years later, the team led by Carl D. Anderson and Seth Neddermeyer at Caltech in 1936 took the whole merit [6].

Only two years after the Caltech discovery, Pierre Victor Auger measured different particles of similar characteristics in coincidence in time by means of detectors placed in different positions, indicating that all particles were coming from a single event [7, 8]. Other groups, as those led by Rossi, Bothe or Kolhörster [9] confirmed this finding. The extensive air shower era was born.

Instrumentation and detection techniques

From the electrometer that Wulf invented and used in the Eiffel Tower to the present cosmic rays observatories there has been a long way to walk.

In 1924, Bothe developed the coincidence technique, proposing an instrument to detect secondary particles that come from a single primary [10]. In collaboration with Kohlhörster, he used this coincidence circuit to show coincidences in detectors surrounded by thick walls of lead, proving the existence of penetrating particles coming from cosmic rays. To this purpose they used several Geiger-Müller counters, developed just one year before [11], as an improvement of the Geiger counters [12]. This coincidence technique was the one applied by Pierre Victor Auger to the mentioned discovery of the extensive air showers, a decade later.

In 1948, Williams linked several fast ionization chambers to detect the secondary particles of the extensive air shower, and to derive properties of its shape [13]. A few years later, Rossi and his colleagues used for the first time scintillator material for the same purpose [14]. Porter developed, in 1958, the first water Cherenkov detector [15], surprisingly similar to those currently used in modern observatories. In the 1960s, the combination of different layers of ionization chambers and lead improved the method of measuring the energy of an incoming hadronic particle.

In a parallel line of research concerning the detection of the extensive air showers, Blackett suggested, in 1948, that part of the light of the night-sky could be Cherenkov light produced by the secondary particles in the extensive air shower [16]. Only five years later, light pulses in coincidence with cosmic ray events were measured using a photomultiplier tube with its cathode at the focus of a parabolic mirror [17]. The idea of the Cherenkov emission in the visible wavelength motivated the search of the same emission at other frequencies [18]. Jelley et al. [19] reported strongly pulsed radio emission at frequencies around 40 MHz coming from extensive air showers. The fluorescence detection technique was first pointed out by Suga [20] and Chudakov [21] in 1962. By means of these techniques the atmosphere can be used as a calorimeter, indicating directly the total energy of the shower, and it is possible to record the whole development of the cascade, instead of sampling the shower at a few scattered points in space. They were suggested by Greissen [22], already in 1965, as the best way to pursue the detection of large showers.

A century after the discovery of the cosmic rays by Victor Hess and almost 80 years after the discovery of the extensive air showers by Pierre Victor Auger, many detection techniques have been developed, many observatories have been constructed and operated, one of them being the core of this thesis, and many answers have been given. Nevertheless, many questions remain open, thus these detection techniques still need to be improved.

Chapter 1

Extensive air showers

Nowadays, a cosmic ray is defined as a charged nucleus originated outside the solar system, with energies from 10^6 eV to 10^{20} eV [23], although their by-products, like photons and neutrinos produced in their interactions with source or intergalactic matter, are also subject of study. The number of these particles arriving at Earth decreases dramatically with the energy. This flux varies from $1\,\mathrm{m}^{-2}\,\mathrm{s}^{-1}$ for particles with 10^{11} eV, to $1\,\mathrm{m}^{-2}\,\mathrm{yr}^{-1}$ at 10^{15} eV, and to $1\,\mathrm{km}^{-2}\,\mathrm{century}^{-1}$ at 6×10^{19} eV. This PhD thesis is mainly focused on those with the highest energy. When one of these cosmic ray enters in the atmosphere of the Earth it interacts with the atoms or nuclei in the air generating a lot of secondary particles. These secondary particles define an extensive air shower, and they are mainly photons, electrons, positrons and muons, among others in lesser extent. This effect blurs the characteristics of the primary particle making difficult the analysis to obtain the energy, the mass and the arrival direction of the primary particle. At the same time, this is the only way by which this scarce and energetic natural phenomenon can be measured, as the atmosphere plays the role of a calorimeter and it spreads the effect from a single point to a large area allowing its detection. The description of the extensive air shower is addressed in sections 1.1 and 1.2. The different techniques applied to the detection of extensive air shower are described in section 1.3. A description of the Pierre Auger Observatory is detailed in section 1.4.

1.1 Description of the extensive air showers

After the first interaction between the primary particle and the atoms or nuclei of the atmosphere, the production of secondary particles is initiated. A shower initiated by a vertical proton of 10^{19} eV produces about 3×10^{10} particles [23]. The number of secondary particles in these cascades is enormous, but the fraction that reaches the ground is very reduced. This is, essentially, because the atmosphere of the Earth has a thickness ($1033\,\mathrm{g/cm}^2$) 28 times larger than the electromagnetic radiation length in air ($X_0^{air} = 36.62\,\mathrm{g/cm}^2$) and 11 times larger than the nuclear interaction length in air ($\lambda_I^{air} = 90.1\,\mathrm{g/cm}^2$) [24]. The evolution of the number of secondary particles along the atmosphere is shown in figure 1.1. The number of secondary particles, in this case, decreases for atmospheric depths deeper than $800\,\mathrm{g/cm}^2$. The fluctuations in the development of the shower are large, making that two identical primaries entering in the atmosphere with the same energy and arrival direction can develop differently.

These shower-to-shower fluctuations are important as they limit the process of reconstruction back to the primary particle.

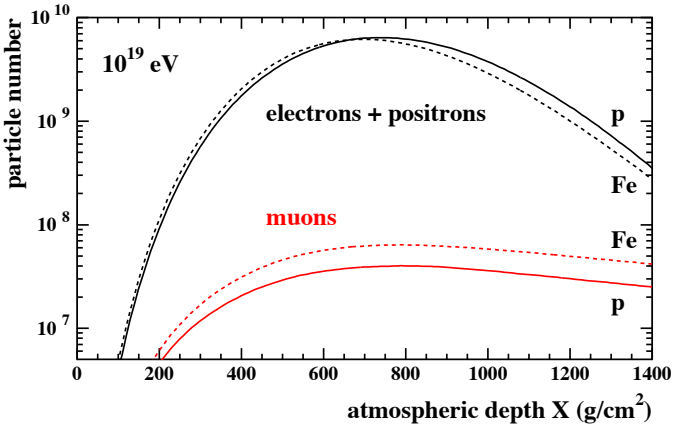

Figure 1.1 Evolution of the number of secondary particles with the traversed atmosphere for a 10^{19} eV simulated proton and iron induced air shower. From [25].

Electromagnetic showers

Extensive air showers induced by photons contain, essentially, only the electromagnetic component (e^-, e^+ and γ). The two main interaction mechanisms that develop this kind of extensive air showers are the Bremsstrahlung for electrons and positrons and pair production for photons. Both processes alternate between them in the production of new particles. As the energy loss due to Bremsstrahlung depends on the energy of the particle, this process is important at high energies and, consequently, at the first steps of the shower. Electrons lose about 60% of their energy in every interaction length. After some steps of multiplication, the energy of the particle decreases, therefore the energy loss due to Bremsstrahlung becomes lower, and the energy loss due to ionization becomes important. The ionization process dissipates the energy of the shower into the atmosphere, stopping the multiplication. The critical energy is defined by Rossi [26] as the energy at which the ionization loss per radiation length is equal to the particle energy [27]. The value of the critical energy for electrons in air ($E_c^{em} = 81.4\,\mathrm{MeV}$) indicates where the multiplication of secondary particles in the extensive air shower stops.

The whole development of the extensive air shower is too complex to be followed particle by particle, but Heitler [29] proposed a model to follow the electromagnetic cascade. The Heitler model divides the process of development of the electromagnetic cascade in layers of length $d = X_0^{air} \ln 2$. After the first layer the photon has split by pair production into an $e^- e^+$ pair. Each of them, after another layer, produce a photon via Bremsstrahlung (figure 1.2, left). After n layers, the distance $X[\mathrm{g/cm^2}]$ and the total number of electrons and photons (shower

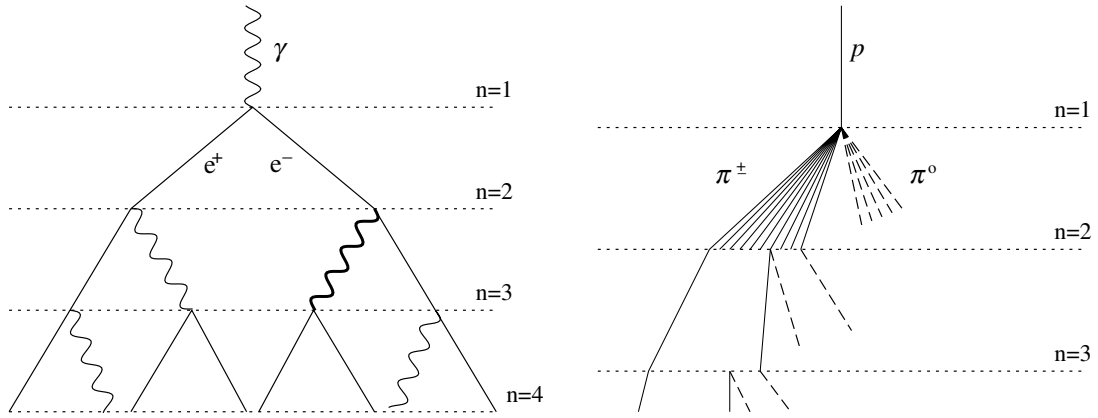

Figure 1.2 Left: evolution of the electromagnetic component of an extensive air shower as described by the Heitler model. Right: evolution of the hadronic cascade as described by the extended Heitler model. From [28].

size) N can be calculated as:

$$\begin{aligned} X &= nX_0^{air} \ln 2 \\ N &= 2^n = \mathrm{e}^{X/X_0^{air}} \end{aligned} \tag{1.1}$$

This multiplication of particles lasts until the energy of the individual particles drops below the critical energy. At this point, the shower reaches its maximum size, and the initial energy (E_0) is shared by $N_{\max}$ particles with E_c^{em}.

$$E_0 = E_c^{em}\ N_{\max} \tag{1.2}$$

The position of the shower at this point of maximum size is called the atmospheric depth of maximum ($X_{\max}$). It can be calculated knowing the number of steps or layers crossed (n) in the process until this point.

$$X_{\max} = nX_0^{air} \ln 2 \tag{1.3}$$

Since n can be extracted from equation 1.1, being related with $N_{\max}$, and this with the initial energy, the $X_{\max}$ for the photon initiated extensive air shower is:

$$X_{\max} = X_0^{air} \ln \left(E_0/E_c^{em}\right) \tag{1.4}$$

The change of $X_{\max}$ per decade of energy is called elongation rate (D_{10}), and it is defined as:

$$D_{10} = \frac{\mathrm{d}X_{\max}}{\mathrm{d}\log_{10} E_0} = 2.3X_0^{air} = 85\,\mathrm{g/cm^2} \tag{1.5}$$

In spite of the simplicity of the model, two very important predictions are given. First, the maximum size of the shower is proportional to the energy of the primary particle (equation 1.2). Second, the depth of the maximum shower development grows logarithmically with this energy (equation 1.4).

Hadronic showers

The Heitler model for the electromagnetic cascade has been extended by Matthews [28] to be applied to the hadronic cascade. In this model the atmosphere is divided in layers of fixed thickness $d = \lambda_\pi \ln 2$, with λ_π being the pion interaction length ($122\,\mathrm{g/cm^2}$). The primary hadron interacts after traversing one layer, producing $2N_\pi$ charged pions and N_π neutral pions, where N_π is called the pion multiplicity. Neutral pions immediately decay into photons generating an electromagnetic cascade. Charged pions produce new pions after travelling another layer (figure 1.2, right). As in the Heitler model, the process continues until the critical energy for pions (E_c^π) is reached, then the charged pions begin to decay into the muons observed at ground. The critical energy for pions can be estimated as the energy at which the decay length of a charged pion becomes less than the distance to the next interaction point ($E_\mathrm{c}^\pi = 20\,\mathrm{GeV}$ in air). The model assumes an equal repartition of the energy in the production of secondary pions. For the energies between 1 GeV and 10 TeV a value of $N_\pi = 5$ is appropriate.

A proton with energy E_0 entering the atmosphere creates, after n layers, a total of $(2N_\pi)^n$ charged pions. Assuming that all of them decay into muons after they reach E_c^π, this number of pions gives directly the muon number (N_μ) in the shower. The number of layers is calculated from the number of steps the pions need to reach the critical energy, that is $n = \ln(E_0/E_\mathrm{c}^\pi)/\ln(3N_\pi)$. Introducing $\beta = \ln(2N_\pi)/ln(3N_\pi)$, where $\beta = 0.85$ for $N_\pi = 5$, the number of muons in the proton shower is:

$$N_\mu^p = \left(\frac{E_0}{E_\mathrm{c}^\pi}\right)^\beta \tag{1.6}$$

The charged pions keep the energy in the hadronic cascade, that at the step n is $(2/3)^n E_0$. The neutral pions transfer the rest, one third of the energy at each layer, to the electromagnetic cascade. The energy measured in the electromagnetic component ($\sim E_0(1-(2/3)^n)$) is called calorimetric energy (E_cal) and it tends quickly to E_0 when the number of steps increases, so E_cal is a good approximation for the primary energy.

At this point, the cascade is made of three main components: electromagnetic, muonic and hadronic. The electromagnetic component is dominant in number and in energy (figure 1.1). It carries in average 98% of the total energy, whereas the muonic component represents about 1.7% of it. The rest is the hadronic component, not numerous enough to appear in figure 1.1. The atmospheric depth of maximum is then, essentially, the maximum of the electromagnetic component. A proper evaluation of X_max would need to account for the points of origin of the subshowers at every step. This is beyond the scope of a simple model. Nevertheless, it is still possible to assume that the shower maximum is dominated by the electromagnetic subshower produced in the interaction with the largest inelasticity, which is usually the first interaction. The X_max of the hadronic cascade is then given by the interaction length of the primary

particle plus the depth of the electromagnetic cascade produced in the first interaction:

$$X^{p}_{\max} \approx \lambda^{air}_{I} + \ln \frac{E_0}{2N_\pi E^{em}_{c}} \tag{1.7}$$

The factor 2 takes into account that the neutral pions decay into two photons.

When the incoming particle is a nucleus with atomic number A and energy E, the cascade process can be studied by considering individual single nucleons with energy E/A, each acting independently. The resulting shower is treated as the sum of A separated proton air showers all starting at the same point. This is called the superposition model. The superposition model can be applied to see the differences in the evolution of the cascades initiated by protons or heavier primaries.

The first result is that, from equation 1.6, the number of muons for a nucleus of atomic number A can be expressed as:

$$N^{A}_{\mu} = A \left(\frac{E_0/A}{E^{\pi}_{\mathrm{c}}} \right)^{\beta} \tag{1.8}$$

The ratio between the number of muons for a nucleus and a proton then depends exclusively on the pion multiplicity expressed in β:

$$\frac{N^{A}_{\mu}}{N^{p}_{\mu}} = A^{1-\beta} \tag{1.9}$$

From the equation 1.7, repeating the process, the difference between the atmospheric depth of maximum of a proton and of a nucleus with atomic number A is:

$$X^{A}_{\max} - X^{p}_{\max} = X^{air}_{0} \ln A \tag{1.10}$$

Both Heitler model and the extension proposed by Matthews can be improved by Monte Carlo (MC) simulations that take into account individual hadronic processes in the atmosphere. Nevertheless, the results obtained by the model are qualitatively confirmed by the simulations. For ultra-high energy cosmic rays, the energies involved in the very few first steps of the process are far from those reached in accelerator physics, so the hadronic interaction models used in the MC simulations, for these first steps, can only extrapolate from the accelerator measurements. Whereas this is a source of uncertainty, the ultra-high energy cosmic rays experiments are useful to constrain the hadronic interaction models by measuring the muon content and muon production depth of air showers and the proton-air cross section for particle production. In particular, several hadronic interaction models are mentioned in this work: Sybill 2.1 [30], QGSJet01, QGSJet-II-03, QGSJet-II-04 [31–33], EPOS 1.99 and EPOS LHC [34]. The different versions of the models have been updated to match with the latest results from the Large Hadron Collider (LHC). AIR shower Extended Simulations (AIRES) [35] and COsmic Ray SImulations for KAscade (CORSIKA) [36] are packages that uses the cited models to simulate the development of the cascade in the atmosphere from the primary particle to the secondary particle at ground. Whereas A Multi-Particle Transport

Code (FLUKA) [37] and GEANT4 [38, 39] are more general toolkits for the simulation of the passage of particles through matter.

1.2 Phenomenology of extensive air showers

The extensive air showers are described by two profiles: the longitudinal and the lateral ones. The longitudinal profile is the number of particles as a function of the amount of crossed matter (atmospheric depth), shown in figure 1.1. In general, after a few steps, all showers have similar global characteristics. In particular, the shape of the shower is universal except for a translation depending logarithmically on energy and a global factor roughly linear in energy. The Gaisser-Hillas function [40] parameterizes the number of secondary particles as a function of traversed atmospheric depth (X):

$$N(X) = X_{\max} \left(\frac{X - X_{\text{first}}}{X_{\max} - X_{\text{first}}} \right)^{(X_{\max} - X_{\text{first}})/\lambda} \exp\left(\frac{X_{\max} - X}{\lambda} \right) \tag{1.11}$$

where X_{first} is the depth of the first interaction, $N_{\max}$ the number of particles observed at $X_{\max}$, and λ a parameter describing the attenuation of the shower.

The lateral profile is the number of particles as a function of the distance to the axis (r), at a specified atmospheric depth, shown in figure 1.3. While the shower develops, secondary particles begin to spread from the shower axis. The scale of the transverse development is given by the Molière radius (R_{M}) [27]. The lateral profile is described by the lateral distribution function (LDF), that describes the deviation of the particles from the shower axis. The density of particles decreases rapidly with the distance to the axis as $1/r^b$, generally with $2 \leq b \leq 4$ [41]. The commonly used Nishimura-Kamata-Greisen (NKG) lateral distribution function [42] is a good approximation:

$$LDF(r) = C(s) \left(\frac{r}{R_{\text{M}}} \right)^{s-2} \left(1 + \frac{r}{R_{\text{M}}} \right)^{s-4.5} \tag{1.12}$$

where s is a parameter related with the age of the shower and $C(s)$ is a normalization factor.

The main ingredients of the extensive air showers at ground are electrons (and positrons), photons and muons. Muons, as they appear in several points of this work, are worthy to be discussed in some detail. They are created, as seen above, from pions in, mainly, the hadronic cascade. With charge equal to that of electrons and approximately 200 times heavier, their ionization in the traversed media is lower. At the muon energies involved in the cascade (few GeV, figure 1.4, right) the energy deposited is about $2\,\text{MeV/g/cm}^2$ [43]: they are minimum ionizing particles. This implies that a muon produced in the extensive air shower with, for example, 5 GeV, can traverse $2500\,\text{g/cm}^2$ (3 times the atmosphere length) before loosing its whole energy, or survive the long path that they have to traverse in inclined air showers. The muonic component survives in the shower much longer than the electromagnetic one. This electromagnetic component, with lower energy (figure 1.4, left) is absorbed with less amount of matter crossed.

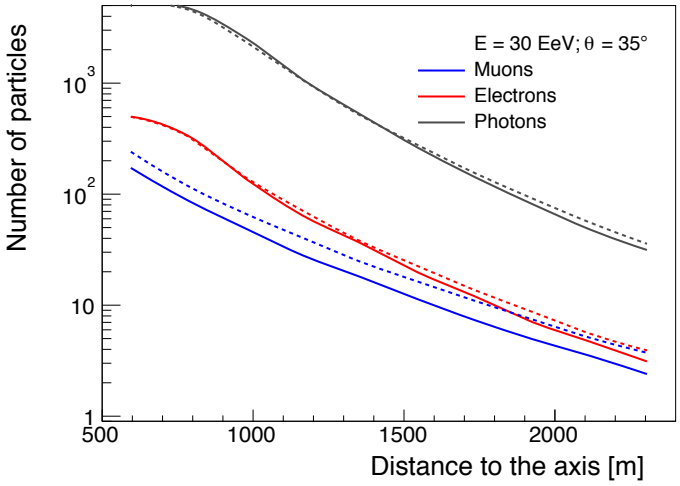

Figure 1.3 Average number of secondary particles hitting a $10\,\mathrm{m}^2$ detector according to the distance to the axis for an extensive air shower induced by a proton (solid line) and iron (dashed line) with 30 EeV of energy ($1\,\mathrm{EeV} = 10^{18}\,\mathrm{eV}$) and 35° zenith angle, simulated with QGSJet01.

1.3 Detecting extensive air showers

Although the range of energies in which the extensive air showers can be detected is large, a general description of the used methods is possible. The detection methods can be separated in two groups: the ground methods and the calorimetric methods.

Ground methods

The first group includes those methods by which the extensive air shower is sampled at a single point in the longitudinal development, as the shower is reconstructed from the characteristics measured at ground. This gives access mainly to the lateral profile. Nevertheless, as it will be seen in chapter 3, different methods can be applied to extract information about the longitudinal profile. The detection is based on the direct interaction of the secondary particles with the detectors spaced at ground, thus the detection is only possible near the shower axis. Due to this necessity of proximity, a set of several detectors has to be spread over a large surface to ensure an observation of this very scarce phenomena. The energy range of the primary particle intended to be detected determines the characteristics of the array, such as spacing, total area and altitude. Two kinds of detector are mainly used:

Water Cherenkov detectors (WCD) are volumes of water with photomultiplier tubes (PMTs) in the interior able to register the Cherenkov light produced by charged particles passing through the detector (see next subsection for the description of the Cherenkov effect). The shape, with 1.2 m height in the Pierre Auger Observatory (Auger) [44] case or 4.7 m in the High Altitude Water Cherenkov (HAWC) [45] observatory gives them special sensitiveness to

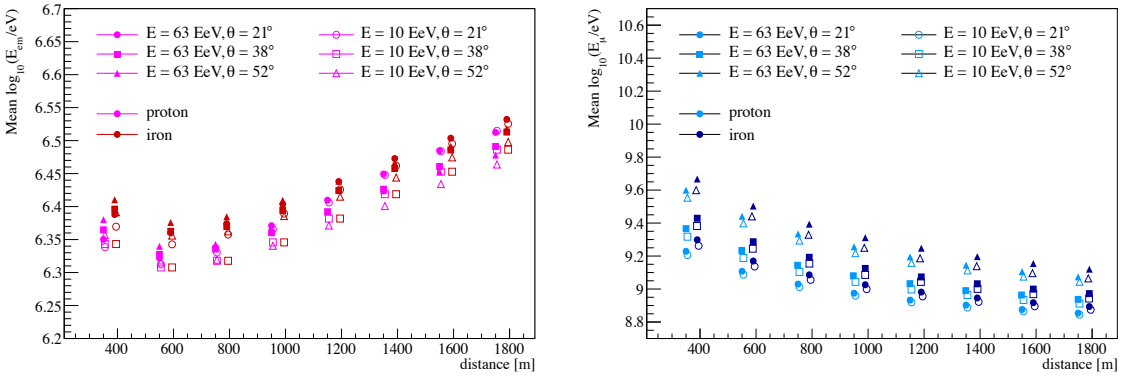

Figure 1.4 Energy of the secondary particles of extensive air showers at ground level for different distances from the shower axis. For electrons and positrons (left) the average energy is of the order of MeV ($1\,\text{MeV} = 10^6\,\text{eV}$), whereas for muons (right) the average energy is of the order of GeV ($1\,\text{GeV} = 10^9\,\text{eV}$). Different primaries (proton and iron) and different primary energies (10 EeV and 63 EeV) are considered. Simulated with EPOS LHC.

the muon component (even if it is mixed with the electromagnetic part) and, consequently, to horizontal air shower.

Scintillators: particles such electrons, alpha particles, ions, or high energy photons (by pair production) passing through a transparent material, can produce a deexcitation after ionization. This effect, called scintillation, is the base of the scintillator detectors. It was the method chosen for Akeno Giant Air Shower Array (AGASA) [46] and for the surface detector array in Telescope Array [47], that has been collecting data since 2008. Future observatories like the Large High Altitude Air Shower Observatory (LHAASO) [48] will also have, among other kinds of detectors, a scintillators array and a WCD array.

Calorimetric methods

The second group includes those by which the extensive air shower can be detected via their electromagnetic emissions produced by the secondary particles, like fluorescence, Cherenkov or radio emissions. They have access to the longitudinal development profile of the extensive air shower, using the atmosphere as a gigantic calorimeter. Both Cherenkov and fluorescence radiation have a wavelength that is in the visible region of the spectrum, near ultraviolet (UV). Nights with little moonlight are required to observe them, thus reducing the exposure time. The fraction of time the detector is able to work is called the duty cycle. The radio emission does not suffer this limitation. A main difference between the two techniques is that whereas the Cherenkov emission is beamed, needing a detection near the shower axis, the fluorescence emission is isotropic, and the detection can be achieved from larger distances. Concerning the radio, both beamed and isotropic emissions are expected, although the latter has not been yet detected.

The Cherenkov light is an emission produced in a dielectric by the passage of charged secondary

particles of the extensive air shower [49]. Most secondary particles in the shower have ultra-relativistic speeds, larger than the local phase velocity of light. When this happens for a charged particle in a dielectric medium, an electromagnetic shock wave that takes the form of a cone of light is emitted towards the front. The angle of this cone is given by $\cos\theta_c = 1/(n\beta)$, where n is the refractive index of the medium and $\beta = v/c$ is the ratio between the speed of the particle and the speed of light, that for ultra-relativistic particles is close to 1. This makes θ_c be around 1° in the air. This angle makes that for vertical extensive air showers a circle with a diameter of about 250 m at ground is illuminated. For large zenith angles the area can increase considerably. This cone of light can be detected at ground either directly with PMT pointing directly to the atmosphere, as the case of Tunka-133 [50], or by the means of parabolic mirrors that concentrate the collected light, as the case of High Energy Stereoscopic System (HESS) [51], Very Energetic Radiation Imaging Telescope Array System (VERITAS) [52], Major Atmospheric Gamma-ray Imaging Cherenkov Telescopes (MAGIC) [53] or the future Cherenkov Telescope Array (CTA) project [54], all those dedicated to detect γ-rays in the energy range of the GeV and TeV. Ice-Cube [55] and Astronomy with a Neutrino Telescope and Abyss environmental RESearch project (ANTARES) [56] deserve a special mention as they have transformed part of the Antarctic ice and the Mediterranean sea, respectively, into enormous ice or water Cherenkov calorimeter detectors, by installing a three-dimensional array of PMTs, dedicated both to the detection of neutrinos in a very wide range of energies.

The fluorescence light is emitted by air molecules after some energy is deposited. The electrons produced in the extensive air shower passing through the atmosphere lose energy by inelastic collisions with nitrogen molecules of the air. A small fraction of the deposited energy is reemitted as UV fluorescence radiation in the spectral range from 290 nm to 430 nm. This fluorescence spectrum in dry air is well known. The number of these emitted photons is proportional to the energy deposited in the atmosphere by the electromagnetic component [57]. This technique is used by the Auger, Telescope Array, All-sky Survey High Resolution Air-shower Detector (ASHRA) [58], and in the past by Fly's Eye [59] and its enlarged and improved version High Resolution Fly's Eye (HiRes) [60]. The future Extreme Universe Space Observatory (JEM-EUSO) [61], oriented to the atmosphere from the International Space Station, will be also based on this technique.

The third calorimetric method is the detection of extensive air showers through their *radio emissions*. The radio emission processes can be separated in isotropic emissions, allowing a detection from the distance, and beamed emission, allowing only the detection near the shower axis. Several experiments have detected radio pulses in coincidence with extensive air showers at different frequencies (MHz and GHz). COsmic ray Detection Array with Logarithmic ElectroMagnetic Antennas (CODALEMA) [62], LOFAR PrototypE Station (LOPES) [63] and Auger Engineering Radio Array (AERA) [64] have confirmed recently this technique, and some work has also been done in RICE [65], Antarctic Impulsive Transient Antenna (ANITA) [66], ARIANNA [67] and Askaryan Radio Array (ARA) [68]. Extensive Air Shower Identification using Electron Radiometer (EASIER) [69] has reported measurements of radio signals at both MHz and GHz ranges. The different processes of radio emissions, the EASIER project and the future perspectives of this method constitute one of the subjects of this PhD thesis, and they are detailed in chapter 5.

Hybrid observatories and others

Most of the observatories chose one detection technique, but *hybrid observatories*, like Auger or Telescope Array, combine more than one detection method, profiting from the so called hybrids measurements (those made with both detectors). Telescope Array consists of three buildings with fluorescence telescopes and a scintillators array covering $700\,\mathrm{km}^2$, whereas Auger consists of 4 buildings with fluorescence telescopes and a WCD array, detailed in next section.

1.4 The case of the Pierre Auger Observatory

The Pierre Auger Observatory is the largest cosmic ray observatory in the world. It is dedicated to measure ultra-high energy cosmic rays, covering 4 orders of magnitude in energy, from $10^{16}\,\mathrm{eV}$ to above $10^{20}\,\mathrm{eV}$. The observatory is located in Argentina, province of Mendoza, near the town of Malargüe, at 35° South and 69° West [44]. There the atmospheric conditions (clear sky and low pollution) are appropriate for the fluorescence technique.

It is placed at 1400 m above sea level, which corresponds to $870\,\mathrm{g/cm}^2$, in terms of atmosphere grammage. This height is suitable to measure the extensive air showers at an age close to the maximum of the shower development for the EeV range, favouring a good energy resolution.

It was completed in 2008 but the data collection started in 2004. At the moment of its construction it was the first observatory combining two techniques for measuring cosmic rays, collecting data both with a surface detector array (SD) [70] and a fluorescence detector (FD) [71] (see figure 1.5). The former is an array of WCDs spread over a flat surface of $3000\,\mathrm{km}^2$ and the latter are 4 buildings in the edges of the array with 6 fluorescence telescopes in each one, facing the interior of the array. The low flux expected at the energies intended to measure requires such a large surface to ensure a statistically relevant number of events. In this case, for the highest energies (above $6 \times 10^{19}\,\mathrm{eV}$) and total area of the observatory, only 30 events per year were expected, according to the predicted flux.

Apart from the benefits of the SD and the FD independently, the hybrid design gives the opportunity to detect extensive air showers with both techniques combined. First, as the duty cycle of the SD is 100%, the data recorded can be calibrated with the FD, being used to measure anisotropy and the energy spectrum with enhanced accuracy and larger statistic, avoiding the uncertainties related to the use of Monte Carlo simulated showers. Second, the combination of both detectors can measure lower energy showers better than the two detectors independently. The reason is that three stations are needed to report an event with the SD, and the FD alone could suffer important uncertainties in the geometrical reconstruction, whereas only one triggered station is needed to perform a hybrid reconstruction properly. Finally, a cross check between the reconstruction done by both detectors can be used to identify sources of systematic uncertainties.

The Pierre Auger Observatory was initially designed to accomplish different objectives [72]:

- To investigate with a large number of events the cosmic rays spectrum at energies above $10^{19}\,\mathrm{eV}$.

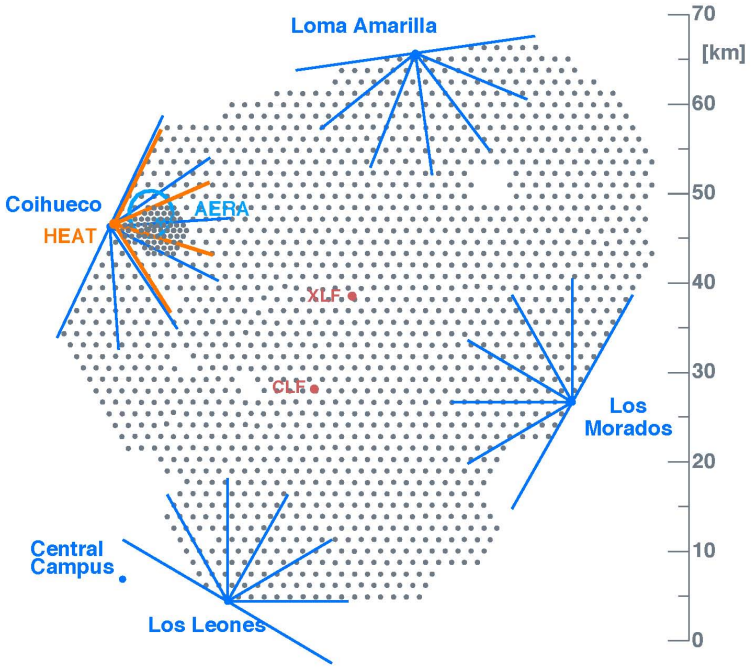

Figure 1.5 Schematic representation of the FD and SD of the Pierre Auger Observatory. The 24 fluorescence telescopes are distributed in four buildings, being located in different sites (Los Leones, Los Morados, Loma Amarilla and Coihueco). They are located at the edges of the SD. The blue and orange lines represent the field of view of each fluorescence telescope, covering the whole area of the observatory. Each black point represents one of the 1660 WCD, 1600 of them spaced 1500 m, and the rest in a denser array near Coihueco FD building. The enhancement High Elevation Auger Telescopes (HEAT), and the Central Laser Facility (CLF) and the eXtreme Laser Facility (XLF), designed to monitor the atmosphere, are represented as orange. The surface of the AERA radio experiment is represented as a blue circle. The distance scale in km is also indicated. Pierre Auger Collaboration.

- To determine with high precision the energy of primary particles with energies above 10^{19} eV, thanks to the hybrid nature of the observatory.
- To determine the arrival direction of the primary ray with an angular precision of 0.2° to 0.35°, using the FD.
- To identify the nature of the particle that gives origin to the extensive air showers distinguishing among showers initiated by protons, photons and heavy nuclei.
- To study the Universe in a yet unexplored energy region, with important consequences in astrophysics and in the theory of elementary particles and their interactions.

During the development of the Observatory, these objectives have evolved. Now cosmic

rays with energies of 0.01 EeV are also investigated, and the arrival of the primary particle is determined also with the SD, not that precise as the FD.

Fluorescence detector

The fluorescence light emitted by the nitrogen molecules is collected by the telescopes of the FD, allowing the measurement of the longitudinal development profiles of air showers in the atmosphere. The integral of this longitudinal profile gives a direct measure of the electromagnetic shower energy, which is approximately 90% of the primary energy. For a given total energy the depth of maximum shower size is correlated with the mass of the primary particle [71].

Four main buildings are located at the edges of the SD overlooking the whole area of the observatory (figure 1.5). Each building has 6 fluorescence telescopes with field of view of 30° in azimuth and 28.1° in elevation, so each building has 180° azimuth range. There is a large UV-passing filter window to select the light entering the telescope. In the inside, a set of mirrors of 12 m^2 with a radius of curvature of 3.4 m concentrates the fluorescence light. Finally, a camera composed by 440 hexagonal PMTs collect the light. A schematic view of the interior of a telescope is shown in the left side of figure 1.6.

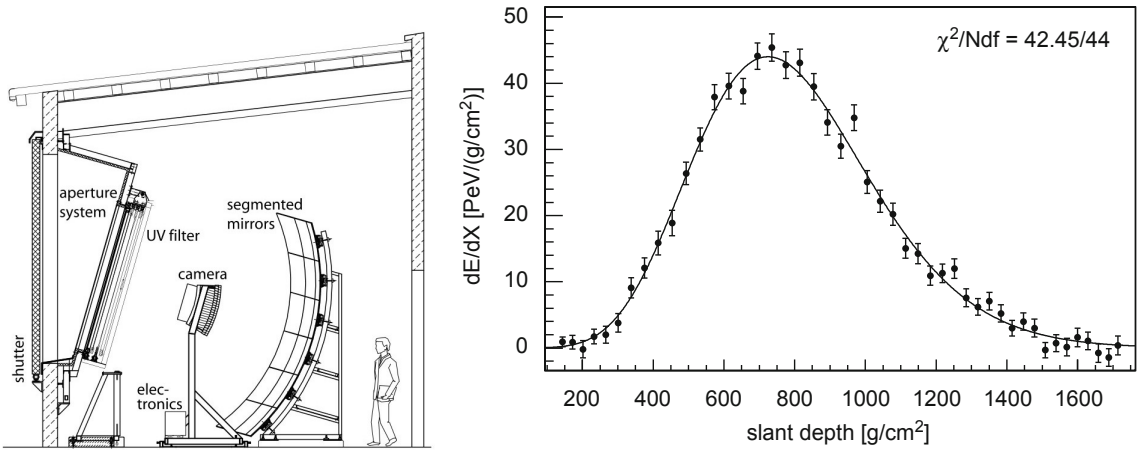

Figure 1.6 Left: schematic view of the inside of a FD telescope of Auger. The camera is composed by the set of PMTs that collect the fluorescence light. The shutter, the aperture system and the UV filter give an idea of the delicacy of the system. Right: example of the reconstruction of the energy deposited over the slant depth in a fluorescence telescope. The points are fitted to a Gaisser-Hillas function (see section 1.2). In the shown case, the integration of the fit gives a reconstructed energy of 3×10^{19} eV. From [71].

The trigger of the FD is designed as a four-level trigger: the first-level trigger works only for individual PMTs; the second is reached when several adjacent pixels have a level-1 trigger in a short period of time; the third is constructed over the time structure of an event; in the fourth trigger a rudimentary event reconstruction of the direction and time of impact on the ground is developed.

The light collected as a function of time is converted to the energy deposited by the shower as a function of atmospheric depth. It is necessary to understand the different sources of light to estimate properly the attenuation of light from the extensive air shower to the FD. These sources are the fluorescence light, the direct and scattered Cherenkov light and the multiple-scattered light. By fitting a Gaisser-Hillas function [73] to the reconstructed deposited energy profile, two important observables are obtained (see figure 1.6, right). First, the integration of the function gives the calorimetric energy. The total energy of the shower is obtained adding the energy carried away by neutrinos and high energy muons, that the FD is not able to measure. This estimation, once done based on MC shower simulations, is now done based on hybrid measurements [74]. And second, the maximum of the fitted function gives $X_{\max}$. This observable is related to the mass of the primary particle (see equation 1.7), giving the FD the capability for composition analysis.

Apart from the sun or moonlight, weather conditions can be also a limit for FD operation (high wind speed, rain or snow), reducing the duty cycle of the FD to approximately 13%. The effect of the atmospheric conditions is also relevant as the atmospheric transmission through aerosols has large time variation. Besides, the atmospheric conditions have influence on the fluorescence yield. This conditions are determined with high accuracy by a set of instruments specifically dedicated. These are the CLF and the XLF [75], represented in figure 1.5.

Surface detector

Charged particles going through the water (its refractive index is 1.33) faster than the speed of light produce Cherenkov radiation [76]. These particles are mainly electrons, positrons and muons. Photons, via pair production, can also generate Cherenkov radiation. Most of the light produced is lost in the interior of the detector, but a sample of it is collected.

The Cherenkov light produced by the particles of the extensive air shower is produced in the interior of the Auger WCD. The WCDs are cylindrical plastic tanks with 1.8 m radius and 1.55 m height. The tanks contain 12 t of pure and deionized water well isolated from exterior sunlight. The water is contained in a bag (the so-called *liners*) internally coated with Tyvek, up to a height of 1.2 m. This material is highly diffusive. The light is smoothly reflected ensuring a homogeneous measure between the PMTs. The shower secondary particles interact with the water when passing through it. The chosen water volume allows the detection at distances from a few hundreds of metres to a few kilometres, well outside the shower core (the Molière radius in air at ground level is around 90 m) [41]. At the top of the interior of the WCD, three large 9 inches PMTs are placed pointing downwards to register the Cherenkov light (figure 1.7). The PMTs signal is collected on an anode and on an amplified dynode. The signal on the dynode is amplified by a nominal factor of 32, to extend the dynamic range of the system. This will provide the data with a high gain signal and a low gain one. The latter will be used when the former is saturated. The signals from anode and dynode are filtered and digitized at 40 MHz using flash analog digital converters (FADCs), achieving a time structure of bins of 25 ns. The station is completed with data acquisition and front-end electronic cards for control and trigger, a solar panel and two batteries for power, a Global Positioning System (GPS) receiver and a system for radio communication.

The SD of Auger is an array of 1660 WCDs spread over 3000 km^2. 1600 of them are spaced 1500 m from each other, with the rest in a denser array, distributed in a regular triangular grid,

as shown in figure 1.5. The spacing between the stations is chosen to allow several stations to be hit for the events above a few EeV. With this distribution, there is almost always one station closer than 750 m from the core (see left panel of figure 1.8).

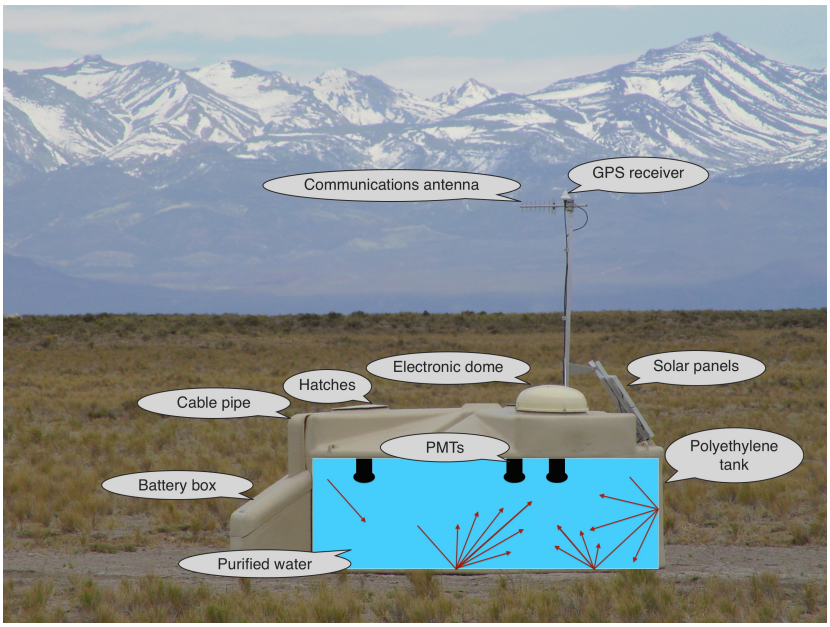

Figure 1.7 An Auger water Cherenkov detector deployed in the field. Three hatches allow the access to the PMTs in the inside, distributed in equidistant positions between them and at 120 cm from the centre. Power and communication devices are also indicated. A schematic representation of the inside is superimposed. The particles passing through the water produce a light (the red lines represent some examples of the traces of the photoelectrons produced) that is collected by the PMTs on the top.

To compare the measurements registered in different stations, a standard unit has been defined to express the measured signal: the vertical equivalent muon (VEM). It represents the signal produced by a vertical muon entering at the center of the detector. As $2\,\mathrm{MeV/g/cm^2}$ is, on average, the energy deposited by a muon, the VEM is equivalent to approximately 240 MeV. Muons coming from different directions leave different amounts of energy, according to the amount of water traversed. Electrons normally leave all their energy that is, in average, a few MeV. The amount of energy deposit by a vertical muon traversing the WCD volume at its centre is also used to obtain a calibration. The constant flux of atmospheric muons (about 3000 go through the Auger WCD each second) is used to this purpose [77, 78].

The time of arrival of the particles to the stations is used to reconstruct the shower front and its axis, and from it to infer the original direction of the primary particle. The size of the signal of the different stations is used to obtain the position of the core, with different corrections derived from the inclination.

The trigger system for the SD is designed as a five level trigger and event selection [70]:

- The first level trigger (T1) acts at the station level and it aims at identifying signals

that could be part of a real shower. Two independent trigger modes are implemented, having been conceived to detect, in a complementary way, the electromagnetic and muonic components. The threshold trigger (TH) searches for a coincidence between the 3 PMTs with more than 1.75 VEM. It is oriented to the muonic component, that normally leaves large signals that are not necessarily spread in time. The time-over-threshold trigger (ToT) searches for at least two PMTs with more than 12 FADC bins with a signal of more than 0.2 VEM in a window of 120 time bins. It is oriented to signals more spread in time, like the electromagnetic ones. The T1 rate is about 100 Hz, nearly all TH. The ToT rate at each detector is lower than 2 Hz and is mainly due to the occurrence of two muons arriving within 3 µs, the duration of the sliding window.

- The second level trigger (T2) acts at station level too. Processed by the local software, it requires either a coincidence of 3 PMTs above 3.2 VEM, or a ToT. The rate is reduced to 20 Hz. This rate is chosen to cope with the bandwidth of the communication system between the detectors and the central campus.

- The central data acquisition system (CDAS) trigger (T3) matches T2 stations in time and space, searching for possible configurations of real events. Different geometrical configurations are considered to account for different kind of events. The T3 triggers the collection of the FADC traces. A FD event can also activate a T3 searching for stations. With the full array configuration, this trigger selects about 1200 events per day, out of which about 10% are real showers.

- The physics trigger (T4) is an off-line one, conceived to distinguish real extensive air showers from random coincidences of atmospheric muons. The T4 asks for the condition that the distance between the stations and the time between the signals is compatible with the time that the speed of light needs to travel between them.

- The quality trigger (T5) is a further off-line one that demands that the station with highest signal be surrounded by 6 functioning stations. T5 rejects events at the edge of the array whose reconstruction may not be reliable.

If the purpose of the FD is to measure the longitudinal profile of the cascade, the SD aims to measure the lateral profile. The lateral profile is expressed by the LDF (see equation 1.12 and figure 1.8, right). The LDF defines the relation between the distance to the axis and the station signals. If the LDF fit is well defined, the average signal at 1000 m (S_{1000}) can be obtained. This value has been proven to be related with the energy of the primary particle for the case of Auger. The distance of 1000 m is the one that makes the estimation independent from the shape of the fitted function [79]. The S_{1000} is used to calibrate in energy the SD against the energy in the FD, with the hybrid events. Previously, the constant intensity cut (CIC) method is applied to compensate for the increasing absorption of the atmosphere as the zenith angle of the shower increases. S_{1000} is transformed into S_{38}, that is, the S_{1000} that the extensive air shower would have produced if it had arrived at the median zenith angle of 38°. Other characteristics of the LDF, such as its slope, also reflect other properties of the extensive air shower, for instance its age. From the analysis of the arrival times of the individual stations, the shower axis direction can be obtained.

The different detectors and the different characteristics of the showers make that the data collected at Auger can be separated in different data sets. The main data set to be considered,

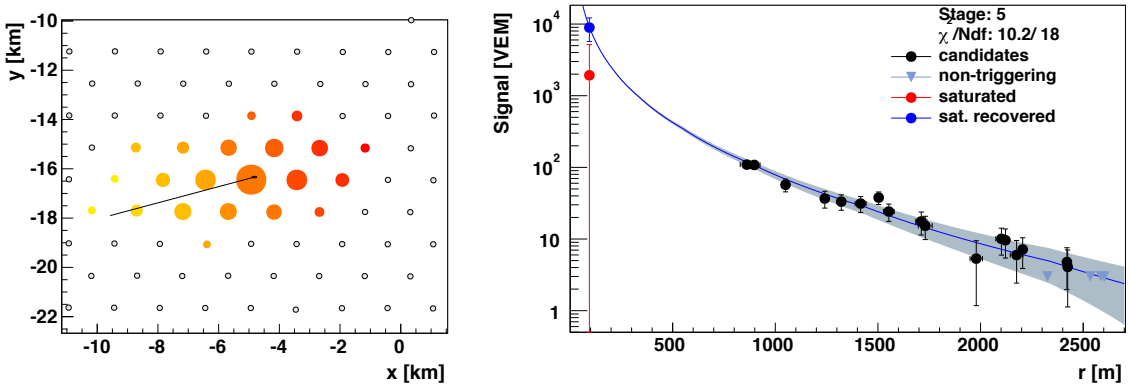

Figure 1.8 Left: representation of an event recorded by the SD with energy $E = 2.56 \times 10^{19}$ eV and zenith angle $\theta = 58.9°$. The detected signals are represented by the size of the marker. The arrival times are represented by the colors. The grid spacing corresponds to 1.5 km between two adjacent stations. Right: the station signal as a function of the distance to the axis. The signal size evaluated at 1000 m (S_{1000}) is used to estimate the primary energy.

as it is the one with largest statistic, is the 1500 m *vertical*, that includes showers with zenith angle lower than 60°, measured in the original array with the indicated spacing. The events with inclination $62° < \theta > 80°$ measured with the same part of the array are considered in the 1500 m *inclined* data set. The vertical showers measured in the part of the array with a denser configuration are the 750 m *vertical*. All three are measured with the SD alone, when the events are also measured with the FD, they are included in the the *hybrid* data set.

Enhancements and R&D

Designed initially to cover higher energies, Auger has dedicated some efforts to extend its energy threshold to lower energies. This extension has been performed with three enhancements:

- Three high elevation fluorescence telescopes observe from 30° to 60°, covering a higher region of the atmosphere. The High Elevation Auger Telescopes (HEAT) [80] are located in one of the fluorescence bays.
- The Infill array is a subarray for the SD with a more dense distribution. This small dense part, with 71 WCDs, is 30 km^2 large, with 750 m spacing between the stations.
- Buried muon counters compose the Auger Muon and Infill for the Ground Array (AMIGA) [81] extension, that will have a counter buried near each of the 71 Infill WCDs. 7 of them are already installed.

Besides this enhancements, new R&D projects are being developed dedicated to the detection of air showers using the radio emission of their electromagnetic component:

- AERA is a subarray of 124 radio antennae, functioning in the MHz frequency range, and covering a surface of 6 km^2.

- EASIER is a subarray of 61 radio antennae, functioning in the GHz frequency range, and covering a surface of $100\,\mathrm{km}^2$.
- Air Shower MicroWave Bremsstrahlung Experimental Radiometer (AMBER) [82] and MIcrowave Detection of Air Showers (MIDAS) [83, 84] are 2 GHz imaging radio telescopes with respectively $14^\circ \times 14^\circ$ and $10^\circ \times 20^\circ$ field of views.

1.5 Summary

The extensive air showers are created by the interactions of the cosmic rays with the atoms in the atmosphere. These showers are made of a dominant electromagnetic component and a muonic one, among other minority components. Several characteristics have been described and found to be correlated with different characteristics of the primary particle, like the energy or the mass. The different components of the showers, result of their development in the atmosphere, can be measured by different detection techniques, sampling their lateral profile at ground or measuring the evolution in the longitudinal profile. The Pierre Auger Observatory combines two different techniques, a SD with WCD and a FD, being the first one to have this hybrid characteristic.

Chapter 2

Ultra-high energy cosmic rays

The measurements of ultra-high energy cosmic rays made by different experiments and observatories described in chapter 1 have discarded some theoretical models, reinforced some others, and open new questions on the subject. Thanks to the tremendous efforts carried out by the community, designing and constructing larger and larger experiments, the knowledge of the cosmic rays has significantly grown.

Their energy spectrum, their possible sources, their propagation, and the different models for the transition region between Galactic and extragalactic cosmic rays are described in section 2.1. The most important results published by the Pierre Auger Collaboration are detailed in section 2.2.

2.1 Ultra-high energy cosmic rays

Very different methods and techniques are applied to measure cosmic rays in the very wide range of energies at which they have been observed. Direct measurements on satellites or balloons are possible for lower energies, but for higher energies large observatories covering large extensions of surface are needed, since the ultra-high energy cosmic rays are studied using the extensive air showers described in chapter 1.

Energy spectrum

Figure 2.1 summarizes the results of the measurements of cosmic rays flux made by numerous observatories in the energy range between 10^{13} eV and 10^{20} eV. The dramatic decrease of flux versus energy anticipated in chapter 1 is evident. In this figure, the differential energy spectrum has been multiplied by $E^{2.6}$ in order to display the features of the steep spectrum.

In the energy spectrum, at 4×10^{15} eV a change in the evolution of the flux is observed. The power index suddenly changes from -2.7 to -3.1. This is the so-called *knee* of the cosmic ray spectrum. At these energies, the cosmic rays are believed to be of Galactic origin, and accelerated by the shock wave produced by Supernova Remnants [85, 86]. The most shared interpretation for the existence of the *knee* is the loss of confinement of lighter cosmic rays by the Galactic magnetic fields [87], but a general consensus does not exist on the chemical

components responsible for this feature, as both proton and helium nuclei are considered as candidates. A different scenario has been proposed, arguing that it might be caused by changes in the hadronic interactions at the energies involved [88]. The idea that the *knee* is a peculiarity of the primary spectrum and not of its observation on Earth was already disfavoured by the agreement of observations done using different components of the extensive air showers and Cherenkov light. Later comparisons of the predictions from hadronic models and LHC data reinforce this conclusion.

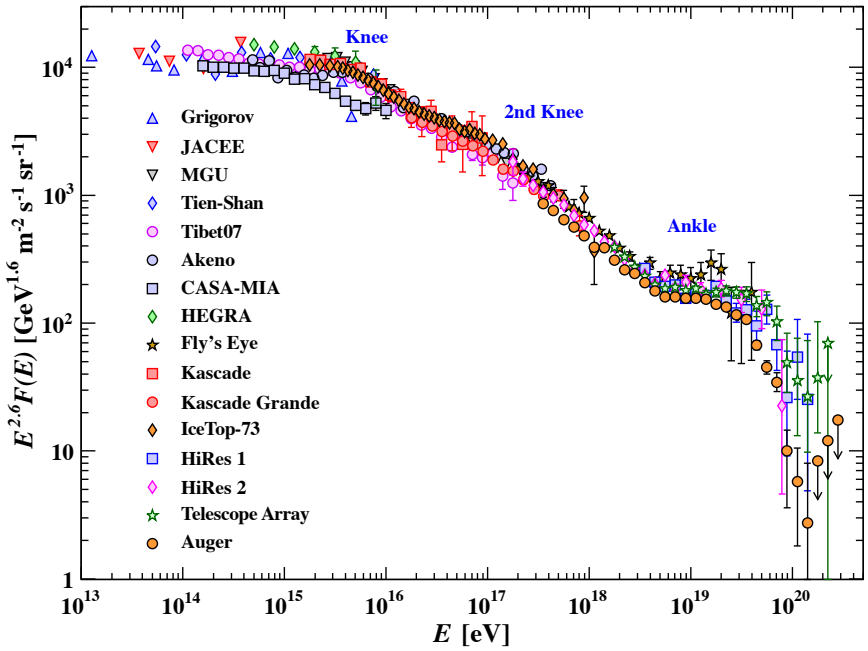

Figure 2.1 Cosmic rays spectrum from 10^{13} eV to more than 10^{20} eV, as measured by different cosmic ray observatories. The main changes in the evolution of the flux are indicated as the *knee*, the *second knee* and the *ankle*. From [89].

A second knee is observed by several experiments in the 10^{17} eV decade, finding different spectral slopes above and below it. However, the differences are compatible and a general agreement gives very high confidence in the existence of a break [90]. This feature is associated with the bending of the iron component [87].

At higher energies, about 4×10^{18} eV, another feature in the evolution of the energy spectrum is observed. The change in the power index, called the *ankle*, happens now in the other sense, going from -3.3 to -2.7 [91]. The transition between a Galactic and extragalactic origin is believed to occur in the energy range between 10^{17} eV and 10^{19} eV. The interpretation of the cause of the *ankle* is in dispute. The spectrum alone is not enough to resolve the question, but composition studies could help. The experiments that could put some light in the topic, as KASCADE-Grande [92, 93], Tunka-133 or IceTop [94] have insufficiently large statistics. Telescope Array and Auger, initially designed to measure cosmic rays at higher energies, are

making some efforts to lower the energy threshold, motivated by the unravelled question of the *ankle* [87].

At even higher energies, above 4×10^{19} eV, some contradictory results were published by AGASA [95, 96] and Fly's Eye [97]. While the former did not observe any change in the index of power law of the flux, the latter observed some indication of a *cut-off*. The dispute ended in the year 2008 with the publication of the results of the measures done by HiRes [98], first, and a little after by Auger [99]. Both observatories observed a suppression of the cosmic ray flux.

Propagation and *cut-off*

A *cut-off* in the energy spectrum was already predicted soon after the discovery of the cosmic microwave background (CMB) [100]. Greisen [101], Zatsepin and Kuzmin [102] (GZK), in 1966, predicted a limit for the spectrum at 5×10^{19} eV. The ultra-high energy protons would interact with CMB photons, through Δ resonances, with the consequent pion production:

$$\gamma_{CMB} + p \rightarrow \Delta^{+} \rightarrow \begin{cases} p + \pi^{0} \\ n + \pi^{+} \end{cases} \tag{2.1}$$

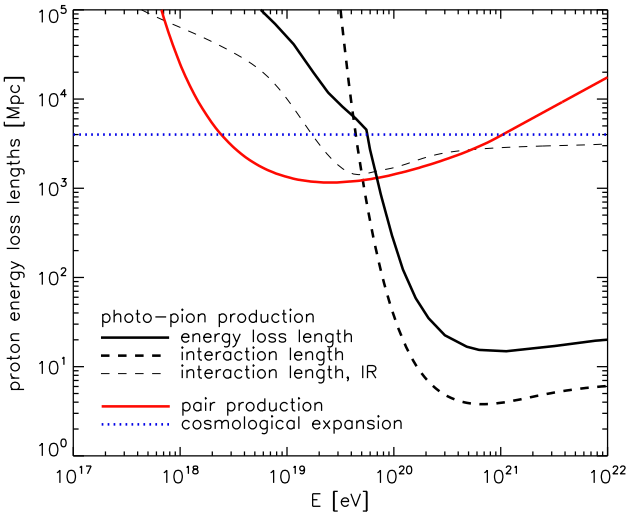

Figure 2.2 Energy loss lengths for different processes affecting protons: black solid line for photo-pion production on CMB and IR-UV photons; red solid line for pair production on CMB photons. Dashed lines represent the interaction length (or mean free path to interaction) for photo-pion production on CMB photons (thick) and IR-UV photons (thin). The dotted blue line indicates the losses due to cosmological expansion. From [103].

The energy loss length is the distance for which the particle loses a fraction $1/e$ of its energy. It is represented for different processes for protons in figure 2.2. The black solid line represents the energy loss length for photo-pion production on CMB and IR-UV photons (equation 2.1).

It goes down to almost 10 Mpc. A proton loses on average 20% of its energy in each interaction, leaving 100 Mpc of path until its energy decreases by one order of magnitude [104]. Due to this effect it exists a maximum distance over which particles with energy greater than the pion production threshold never arrive at Earth. This is called the *GZK horizon*. A second consequence is the production of a large number of very high energy photons and neutrinos, called cosmogenic. The cosmogenic photons and neutrinos could be detected, reinforcing the GZK interpretation of the observed *cut-off*.

Regarding nuclei, the main energy loss process above 10^{19} eV is photodisintegration. It is consequence of the interaction with CMB and infrared background due to giant dipole resonance:

$$A \ + \ \gamma \ \rightarrow \ (A \ - \ 1) \ + \ N \tag{2.2}$$

A is the nucleus with mass number A and N is either a proton or a neutron. The mass number A plays an important role, as it is proportional to the threshold energy of the photodisintegration process. As the nucleus changes its mass in the process (equation 2.2), the direct calculation of the propagation effect is not possible. The whole chain of produced nuclei lighter than the injected one has to be taken into account [23].

$$A \ + \ \gamma_{CMB} \ \rightarrow \ A \ + \ \pi^0 \tag{2.3}$$

where A is the nucleus. Besides, the scattering process, called pair production, affects both protons and heavier nuclei:

$$A \ + \ \gamma \ \rightarrow \ A \ + \ e^- \ + \ e^+ \tag{2.4}$$

The energy threshold for protons is 2×10^{18} eV, while for heavier nuclei the energy is higher. The red solid line in figure 2.2 represent the energy loss length for protons by this process.

The process of pion production is also present in nuclei, but it is not relevant as it is for protons.

Sources and composition

A Galactic origin of the cosmic rays below the *knee* and an extragalactic origin for those above 10^{19} eV is under some level of consensus. If the most accepted scenario for the origin of Galatic cosmic rays is the acceleration in Supernova Remnants, for the extragalactic ones it is not that clear. Hillas [105] proposed an argument about the cosmological structures that can produce particles with such a high energy. The particle can be accelerated to a maximum energy (E_{max}), that is related with the shock velocity (β), the particle mass (Z_e), the magnetic field (B) and the radius of curvature (r_S):

$$E_{max} \ = \ \beta \ Z_e \ B \ r_s \tag{2.5}$$

When B is expressed in µG and r_S in pc, the energy resultant is in EeV. Considering the known astrophysical objects, a limit near 10^{20} eV is found for the maximum energy expected

from a cosmic ray. These objects are represented in the well-known Hillas plot, shown in figure 2.3.

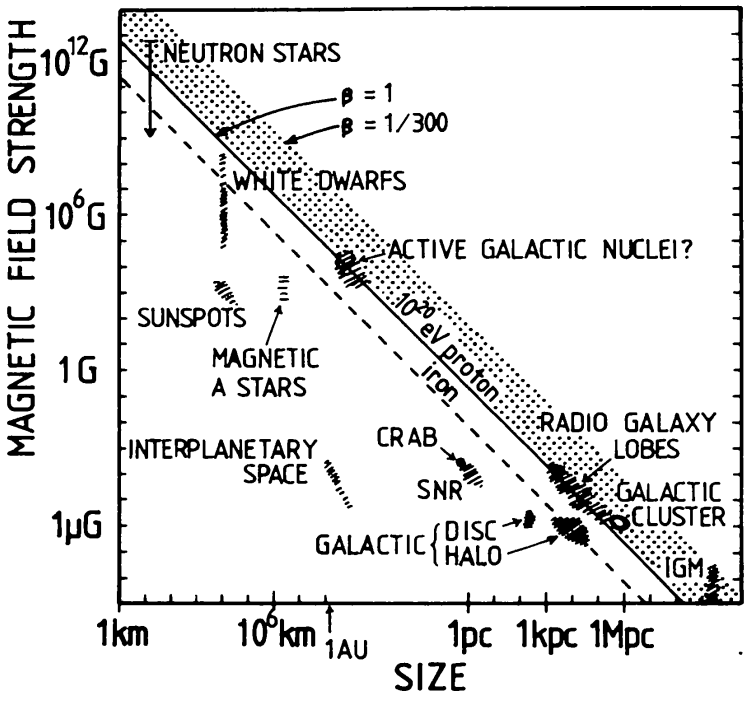

Figure 2.3 Hillas plot: the size and magnetic field strength of possible sources and acceleration candidates are represented. Different shock velocities are considered in the dotted band and different charges (proton and iron) are represented by the different lines. To achieve the energy of 10^{20} eV the object must be above the corresponding line. From [105].

After the Hillas argument is taken into account, three candidates can be remarked as possible sources for extragalactic cosmic rays:

- Galaxies with a nucleus with a strong emission are denominated Active Galactic Nuclei (AGNs). It has been suggested that a supermassive black hole in the centre of a galaxy can generate the energy observed. The accretion disk generated by the mass falling into the black hole can generate jets. These jets, and the core of the AGN, have been proposed as source candidates [86]. They have a typical size of the order of a fraction of a parsec with a magnetic field of the order of a few Gauss [106], leading, in principle, to a maximum energy for protons of a few tens of EeV.

- Gamma-ray bursts (GRBs) are considered as source candidates [107]. Collisions of neutron stars along with supernovae related phenomena have been suggested as interpretation for GRBs. These are the events with the highest known luminosity in the Universe. Although are smaller than the AGNs, their magnetic filed is stronger.

- A third candidate are the pulsars. The pulsars are emitting neutron stars that rotate at high velocity and possess strong magnetic fields. In our Galactic centre, neutron

stars are concentrated. This would lead to a strong anisotropy that is, however, not observed [23].

For a correct identification of the sources, the Galactic and extragalactic magnetic fields must be taken into account. Cosmic rays are scattered by them, thus shifting their arrival direction. This influence is expected to decrease down to a few degrees for energies larger than 10^{20} eV, allowing for a good correlation with the source. Along with the energy, the charge of the particle is a key point in the calculation of the deviation. At the highest energies, the mass composition is still unknown. Last results about composition published by the Auger Collaboration [108] show a compatibility with light mass composition at energies around 10^{18} eV, and a gradual transition to a heavier mass composition at higher energies (see chapter 3). A possibility has been suggested that the sources for ultra-high energy cosmic rays accelerate protons up to only 5×10^{18} eV and iron (if present) up to 10^{20} eV. The other important consequence of this heavier composition would be that the path from the source to the Earth be more affected by deflections, complicating the identification of sources through small scale anisotropies [109].

A suggested exotic possibility is that the particles are not accelerated, but directly produced at energies even higher than those observed [110]. The so called *top-down* models fall in this category. They include the decay of supermassive particles relic of the Big Bang or the collapse of topological defects [111]. Very well considered until some years ago, they were dropped after the limits imposed by Auger in the photon and neutrino fluxes, as these models predict the existence of these particles in a higher proportion than observed (see section 3.3).

Models of the transition region

It is expected that the Galactic magnetic field confines the cosmic rays as long as the size of their Larmor orbit diameter is less than the thickness of the Galactic disk. Since the strength of the magnetic field is of the order of µG, Galactic cosmic rays might be confined in the Galactic disk up to energies of $Z \times 10^{18}$ eV, with Z the charge of the cosmic ray. No significant excess of cosmic rays from the directions to the galactic plane is observed at these energies, so an extragalactic origin is taken as a plausible interpretation. For the transition region between the Galactic and extragalactic cosmic rays, different models are still in dispute.

The ***ankle* transition models** [105, 112] assume that the *ankle* is caused by the overlapping of the Galactic and the extragalactic components of the cosmic rays. The model foresees a flat spectrum for the extragalactic component and a steeper one for the Galactic. These models predict a heavy composition before the *ankle* and a pure proton composition for the extragalactic component. As it will be seen in section 3.2, this expected domination of protons at energies above the transition is in tension with the last composition results published by Auger.

In the **dip model** [113], the transition happens at lower energies, as it shifts the influence of extragalactic protons down to 10^{18} eV. The *ankle* would be then a feature of the extragalactic cosmic rays, caused by pair production losses of protons interacting with the CMB (see equation 2.4). This model expects an almost pure proton composition above 1 EeV (extragalactic) and a pure iron composition below [114]. This would be, again, in contradiction with last Auger results (section 3.2).

The so-called **disappointing model** or **mixed composition model** [115, 116] also places the transition at lower energies than the transition models, as it also shifts the influence of extragalactic protons, foreseeing its dominance below the *ankle*. The maximum energy for extragalactic protons would be the explanation for the *ankle*. Above this energy, heavier nuclei would dominate the spectrum, their limit being proportional to their atomic number. Such a limit in the spectrum would be due to the exhaustion of sources. No GZK suppression and their consequent cosmological photon and neutrinos are predicted by this model.

Taking into account that cosmic rays with higher charge suffer more intensely the effect of the magnetic fields, the regions of the spectrum with a light composition will present some anisotropy in the arrival directions, whereas those regions of the spectrum with a heavy composition will present isotropy in the arrival directions. The anisotropy analyses can also help in this dispute between the models.

2.2 Highlights of the Pierre Auger Observatory

As introduced in the previous section, the Pierre Auger Collaboration has published important results that can help to unravel the mysteries of the ultra-high energy cosmic rays. In this section, some of the most relevant results are summarized. The composition is the main topic of this PhD thesis. The chapter 3 is entirely dedicated to it, where the results relative to the mass, neutrinos, and photons are described.

Energy spectrum

The FD allows for an almost model-independent calorimetric measurement of the energy deposited in the atmosphere by an extensive air shower. The systematic uncertainty on energy is around 14 %. The SD can be calibrated by using hybrid events. The benefits of the hybrid reconstruction of extensive air showers in Auger were already discussed in section 1.4. The correct calculation of the exposure of the detectors is crucial. The data collection in the SD is independent of primary energy or weather conditions, making that the aperture is calculated based purely on geometrical and temporal aspects [70]. On the contrary, the determination of the aperture of the FD is not straightforward, and it needs to take into account, not only geometrical and temporal information, but the weather conditions measured with the specific tools mentioned in section 1.4, and the detector status [117].

The first important result about the energy spectrum was the confirmation in 2008 of a suppression in the flux of cosmic rays at 4×10^{19} eV [99], discussed in the section above. This suppression, measured with the SD alone, had been already pointed out by HiRes in the same year, so the Auger result was published with the comparison against the HiRes result (see figure 2.4).

Two years later, using the hybrid measurements, a combined energy spectrum was presented for the first time by the Pierre Auger Collaboration [118]. The update of the spectrum presented in 2008 was accompanied by a precise location in energy of the *ankle* at $E_{ankle} = 10^{18.61}$ eV as well as by the definition of the change in the spectral index from $\gamma_1(E < E_{ankle}) = -3.26$ to $\gamma_2(E < E_{ankle}) = -2.59$. This was possible because, as introduced in section 1.4, the hybrid measurements allow for a more precise reconstruction of the events with low energy. The most

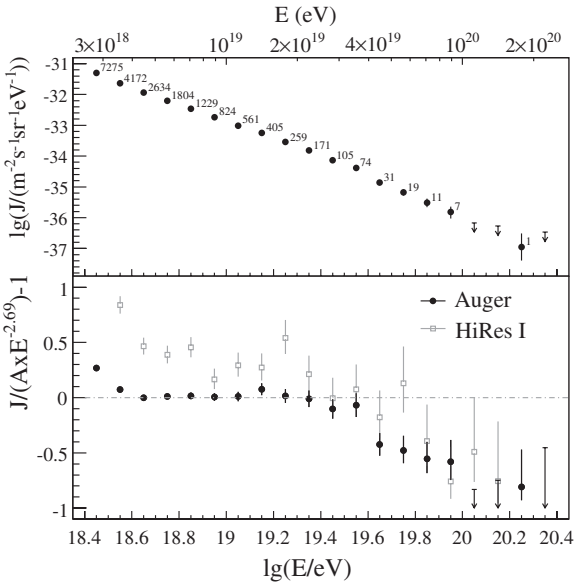

Figure 2.4 Confirmation of the *cut-off* by the Auger Collaboration. In the upper panel the differential flux is shown and in the lower panel the fractional differences between Auger and HiRes are compared with a spectrum with an index of 2.69. From [99].

recent energy spectrum has been presented by the collaboration in the 2013 edition of the International Cosmic Ray Conference (ICRC) [119], where these values have been updated to $E_{ankle} = 10^{18.72}\,\text{eV}$, $\gamma_1(E < E_{ankle}) = -3.23$ and $\gamma_2(E > E_{ankle}) = -2.63$. The spectra measured with the different Auger detectors is shown in the left panel of figure 2.5. The SD has the largest exposure, reaching energies above $10^{20}\,\text{eV}$. The characteristics of the different data sets are summarized in table 2.1. The exposure achieved with SD vertical data in this last spectrum (data until the end of December 2012) is $31\,645\,\text{km}^2\,\text{sr}\,\text{yr}$, whereas in the spectrum published in 2010 (data until the end of December 2008) was $12\,790\,\text{km}^2\,\text{sr}\,\text{yr}$.

Table 2.1 Summary of the experimental parameters of the different data sets of the Auger observatory. From [119].

	Auger SD			**Auger hybrid**
	1500 m vertical	1500 m inclined	750 m vertical	
Data taking period	01/2004-12/2012	01/2004-12/2012	08/2008-12/2012	11/2005-12/2012
Exposure [km^2 sr yr]	31645 ± 950	8027 ± 240	79 ± 4	-
Zenith angles [°]	0-60	62-80	0-55	0-60
Energy threshold [eV]	3×10^{18}	4×10^{18}	3×10^{17}	10^{18}
Number of events	82318	11074	29585	11155

In the right panel of figure 2.5, the combined energy spectrum is shown and compared with the fluxes calculated for different astrophysical scenarios. The models assume pure proton or iron composition. The fluxes result from different assumptions of the spectral index β of the source injection spectrum and the source evolution parameter m, that accounts for different

assumptions in the evolution of the intensity emission of the sources.

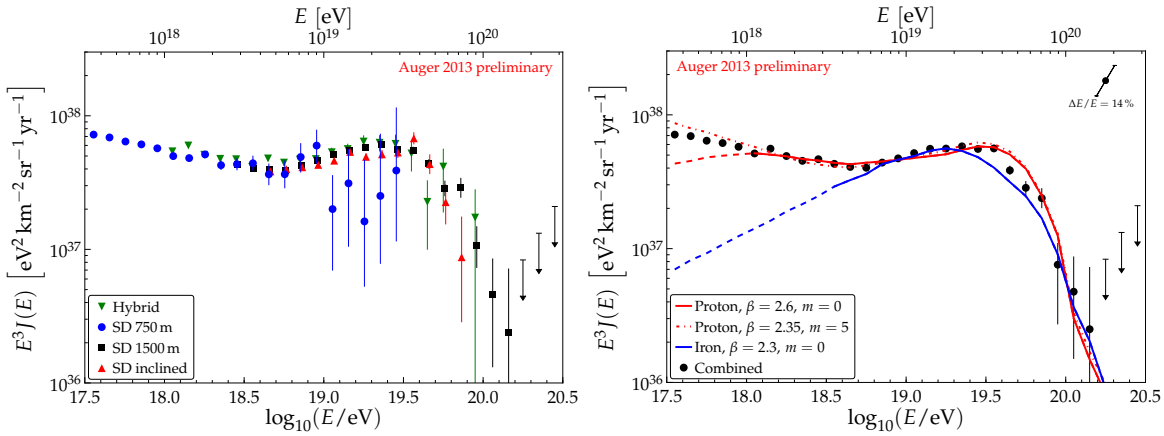

Figure 2.5 Left: energy spectra of ultra-high energy cosmic rays as measured by different detectors at Auger. Right: combined energy spectrum compared to energy spectra from different astrophysical scenarios (see text). The last three arrows represent upper limits at 84 % C.L. From [119].

The suppression is confirmed, but the spectrum alone is not sufficient to clarify its interpretation. This scenario is compatible with the GZK interpretation, but scenarios where protons and nuclei with charge Z can no longer be accelerated at their astrophysical sources above energies of the order of a few times $Z \times 10^{18}$ eV could also explain current observations. Other measurements, being the composition the most relevant, are required to arrive to an unambiguous interpretation of this feature.

Anisotropies

The distribution of extragalactic matter within the GZK horizon is inhomogeneous. Comparison of the arrival directions of cosmic rays with the celestial positions of different populations of relatively nearby astronomical objects may help identifying their origin. A light component of the cosmic rays around and above 4×10^{19} eV is crucial to this purpose, avoiding large deflections of the trajectories by large or uncertain magnetic fields in their way to Earth. Protons with energies around 6×10^{19} eV are expected to deviate by no more than a few degrees from a straight propagation in most parts of the sky, under some assumptions concerning magnetic fields intensity. Instead iron nuclei ($Z = 26$) with the same energy will not preserve a correlation between their arrival directions and the position of their sources [120].

The Auger Collaboration reported in 2007 an evidence for anisotropy in the distribution of the arrival directions of the cosmic rays with highest energies [121, 122]. The arrival directions of the events over the threshold of 55 EeV showed a correlation with the positions of AGNs within 75 Mpc from the Veron-Cetty & Veron (VCV) catalogue [123]. A test with independent data established a confidence level of 99% for the rejection of the isotropic hypothesis. The region of the sky close to the location of the radiogalaxy Cen A gave the largest observed

excess [124]. The evidence of anisotropy has not increased with new data. The expected cosmic ray density is shown in figure 2.6, smoothed over an angular scale of 5°, for a model of cosmic ray origin based on AGNs in the 58-months Swift-BAT catalog, weighted by their X-ray flux and by the GZK attenuation factor for an energy threshold of 6×10^{19} eV, and by the relative exposure of Auger. The 69 events with energy above 55 EeV measured with Auger are also shown [124].

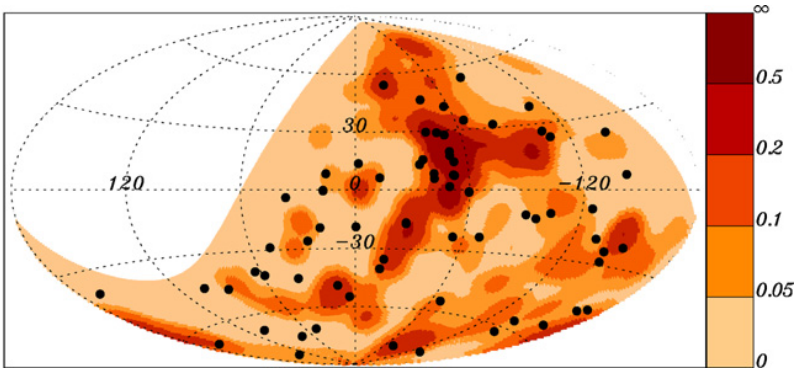

Figure 2.6 Skymap with the arrival directions of 69 Auger events with energy above 55 EeV (filled circles) and with the expected cosmic ray density, smoothed over an angular scale of 5°, derived from a model based on the AGNs in the 58-months Swift-BAT catalog, weighted by their X-ray flux and by the GZK attenuation factor for an energy threshold of 6×10^{19} eV, and by the relative exposure of the observatory. From [124].

The arrival directions of ultra-high energy cosmic rays were also scrutinized in different energy ranges in search for potential large scale patterns. The search for a signature of the escape of galactic cosmic rays is of particular interest, since diffusion and drift motions could imprint dipolar anisotropies at the level of a few percent in the energy range around 10^{18} eV. If instead ultra-high energy cosmic rays at these energies were predominantly of extragalactic origin their arrival directions would be expected to be highly isotropic. Also extragalactic cosmic rays may show a small dipole pattern due to our motion with respect to the frame in which they are isotropic. This has been observed at lower energies, but it is expected to be below the 1% level. A dipole pattern may also be expected at higher energies around and above 10^{19} eV due to the inhomogenous distribution of nearby galaxies.

A powerful tool for the search of large scale patterns is the harmonic analysis in right ascension, that benefits from the almost uniform exposure of any observatory operating with full duty cycle due to the Earth rotation. Subtle detector effects must be under control to perform searches for large scale anisotropies at the percent level, such as the time-dependence of the array exposure, zenithal dependence of the detection efficiency, and atmospheric and geomagnetic effects on energy assignment. This first-harmonic was analysed in right ascension as a function of energy. Upper limits on the amplitudes were obtained, which provided the most stringent bounds at the moment, being below 2% at 99% confidence level (CL) for EeV energies [125, 126].

The search for large scale anisotropies in the distribution of arrival directions of cosmic rays

detected above 10^{18} eV has been carried out also as a function of both the right ascension and the declination [127]. Within the systematic uncertainties, no significant deviation from isotropy is revealed, only updating the upper limits previously established.

The upper limits provided constraint the production of cosmic rays above 10^{18} eV, since they allow to challenge an origin from stationary galactic sources densely distributed in the galactic disk and emitting predominantly light particles in all directions.

At present there is no statistically significant evidence for anisotropy in the distribution of arrival directions at the highest energies that could point to the place of origin of ultra-high energy cosmic rays. There are hints for a dipole pattern in the distribution of arrival directions at energies around 10^{18} eV, and also at higher energies. Upper bounds on dipolar anisotropies at 99% CL were established, that are stringent enough to severely constrain models of galactic origin. It will be important to further scrutinize these hints for a large scale pattern in the distribution of arrival directions with independent data.

Hadronic interaction models

The measurements of extensive air showers in the Pierre Auger Observatory not only can put light in the knowledge of the ultra-high energy cosmic rays, but also can be useful to constrain the hadronic interactions models at these highest energies. As introduced in section 1.1, at the highest energies, the models are a source of uncertainty, as they can only extrapolate from lower energies. This is at the same time an opportunity to test them. The proton-air and proton-proton cross section and the muon content measured at Auger are presented in the following.

The idea of using the tail of the $X_{\max}$ distribution to measure the proton-air cross section was first exploited by Fly's Eye [128, 129]. Auger has also applied this technique by using the hybrid events [130]. Since the major source of systematic uncertainty is the unknown mass composition of cosmic rays, the analysis has been restricted to the energy region between 10^{18} eV to $10^{18.5}$ eV, where the composition found is compatible with a high fraction of protons (see section 3.2). The selection is done by extracting, from the $X_{\max}$ distribution, the most penetrating showers. The average energy of the selected events corresponds to a center of mass energy of $\sqrt{s} = 57$ TeV in proton-proton collisions. Two steps are followed in this analysis. First, the measurement of an air shower observable with high sensitivity to the cross section. Second, this measurement is converted to a value of the proton-air cross section for particle production. The chosen observable is Λ_η, defined via the exponential shape of the tail of the $X_{\max}$ distribution, $dN/dX_{\max} \propto \exp(-X_{\max}/\Lambda_\eta)$, where η denotes the fraction of most deeply penetrating air showers used. For the analysis, $\eta = 0.2$ is used. The lower this value, the higher the contribution of protons in the sample, but the lower number of events are available. Simulations with the four main hadronic interaction models (QGSJet01, QGSJet-II-03, Sybill 2.1 and EPOS 1.99) are conducted. The cross sections in the simulation have been tuned to match the Λ_η found in the data, finding a value for the proton-air cross section. To compare with accelerator data, the calculation of the inelastic and total proton-proton cross section is done using the Glauber model[131, 132]. The values found by the Auger Collaboration for the proton-air cross section and the inelastic proton-proton cross

section are represented in the left panel of figure 2.7 and detailed below:

$$\begin{aligned} \sigma^{prod}_{p-air} &= [505 \pm 22(\text{stat})^{+28}_{-36}(\text{syst})] \text{ mb} \\ \sigma^{inel}_{p\text{-}p} &= [92 \pm 7(\text{stat})^{+9}_{-11}(\text{syst}) \pm 7(Glauber)] \text{ mb} \end{aligned} \tag{2.6}$$

From the result shown in figure 2.7 (left), it is concluded that the evolution of the cross section with the energy of the centre of mass is flatter than the general predictions of the hadronic interaction models.

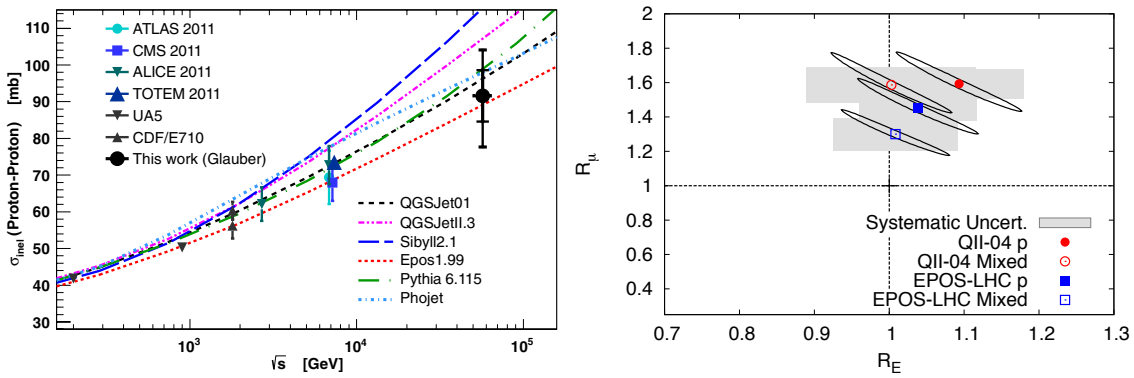

Figure 2.7 Left: proton-proton cross sections as measured by Auger compared with model predictions. From [130]. Right: rescaling factors for the best fit for QGSJet-II-04 and EPOS LHC for pure proton and mixed composition. The ellipses show the $1-\sigma$ statistical uncertainties and grey boxes the estimated systematic uncertainties. From [133].

The Auger Collaboration has explored the possibility to subtract the electromagnetic component from the total signal of the extensive air shower [133]. The former is estimated with the FD, where only the electromagnetic component contributes to the signal in the fluorescence telescopes, whereas the latter is estimated in the SD, where both components are mixed. A set of 411 hybrid events in a narrow range of energy from $10^{18.8}$ to $10^{19.2}$ eV is selected with several quality cuts. For each event in the set, MC simulated events are generated with the same geometry and energy, until 12 of them have similar $X_{\max}$. Out of these 12, and based on the χ^2-fit, the 3 which best reproduce the observed longitudinal profile are selected. For these 3 simulated events the response of the detector is also simulated. This is carried out for different hadronic interaction models (QGSJet-II-04 and EPOS LHC) and for different primaries (proton, helium, nitrogen, and iron). The ground signal is modified in the simulated events to fit the ground signal in the data. Two rescaling factors are introduced: R_E and R_μ. R_E acts as a rescaling of the energy of the primary particle, which rescales the total ground signal of the event uniformly. R_μ rescales only the muonic contribution to the ground signal. A simulated S_{1000} is calculated as function of R_E, R_μ and the primary particle type. R_E and R_μ are fitted to minimize the discrepancy between data and simulation in S_{1000}, for each hadronic interaction model considered. The obtained fitted value for R_E is compatible with 1 for pure proton and mixed composition when considering the systematic uncertainties.

Whereas the rescaling factor R_μ, for the different models and primaries, suggests a deficit in the muonic component in the predictions, as the observed muonic component of the signal in air showers with 10^{19} eV (137 TeV as center of mass energy) is a factor 1.3 to 1.6 larger than predicted by the leading hadronic interaction models tuned to fit LHC and lower energy accelerator data.

This deficit has been also observed in other analyses aiming at determining the muon component in the mass composition studies, that are described in chapter 3.

2.3 Summary

The ultra-high energy cosmic rays that arrive at Earth are defined by three main characteristics: the energy, the arrival direction and the composition (see next chapter for this last item). The results published by the Pierre Auger Observatory have shed some light on the three of them. The confirmation of the suppression at 4×10^{19} eV and the precise measures of other features of the spectrum like the energy of the ankle and the elongation rate have helped to a better definition of the energy spectrum. Different studies have been carried out searching for anisotropy in the arrival directions at different scales, but no statistically significant evidence has been found.

These results can lead to a deeper understanding of the processes involved in the propagation of the cosmic rays through the Universe, to disentangle between the different models proposed for the transition region, or to establish the source of these particles. Besides, the data collected in the Pierre Auger Observatory have been used to explore other topics like the muon component of the extensive air showers or the proton-proton cross section.

Chapter 3

Mass composition

Energy, arrival direction and mass composition of the primary particle are the three main properties that describe an ultra-high energy cosmic ray. The most complicated of the three, from the experimental point of view, is the third one. Two are the most important problems: the large shower-to-shower fluctuations and the uncertainties about the hadronic interaction models at such high energies. The observatories that have measured the composition at the highest energies, until now, do not fully agree on their results.

The ultra-high energy cosmic rays that arrive at Earth are protons, nuclei and, in a very small fraction, neutrons, photons and neutrinos. Extensive air showers induced by photons and neutrinos have singular characteristics that ease their identification. Extensive air showers induced by hadrons also have singular characteristics, and their identification is possible, but assigning a mass to each hadronic primary particle is a very difficult task. The superposition model, applied to the results of the Heitler model extended for hadronic cascades, predicts the dependence of the observables $X_{\max}$ and N_μ on the mass of the primary particle (see section 1.1). Furthermore, to distinguish a neutron from a proton induced shower is simply not possible, but excesses of the arrival directions in a set of events identified as hadrons with light mass could spot a possible neutron source [134].

Regardless of the experimental difficulties, the mass composition is a key point to answer several questions exposed in the precedent chapter. First, the transition models summarized above can be reinforced or discarded with precise composition measurements. Second, the detection (or confirmation of their absence) of cosmogenic photons and neutrinos can confirm (or discard) the GZK interpretation for the observed *cut-off*. It is worthy to remember that the limits imposed over the photon and neutrino fluxes have already discarded the so called *top-down* models. And third, the composition at the highest energy events, where the suppression in the spectrum has been measured, could disentangle if it is caused by the GZK effect or the exhaustion of sources.

The methodology to infer the mass of the primary particle in hadronic cascades, along with its limitations, are described in section 3.1. The current observables and resolutions for their identification, along with the last results published by Auger, are detailed in section 3.2. The specific analysis for the searches of photons and neutrinos, and the identification of possible neutron sources, are discussed in section 3.3. These results and their possible implications in the general framework of the ultra-high energy cosmic rays are discussed in section 3.4.

3.1 Methodology to infer the mass composition in hadronic cascades

Proton and iron nuclei have been classically treated as the main candidates to dominate the flux at the highest energies. The analyses, generally, consider them as the subjet to be compared, and this approach will be used in this work. Two main arguments support this choice. First, as pointed out, for example, by Kotera and Olinto [103], due to the GZK effect, protons and iron nuclei have more chances to arrive at Earth from long distances as they can travel much longer than intermediate mass nuclei (see figure 3.1). And second, supernovae sources are generally iron rich because the final stage of the fusion process produces an iron core. Despite this, some studies have been carried out considering intermediate mass candidates (see section 3.2 and [135]).

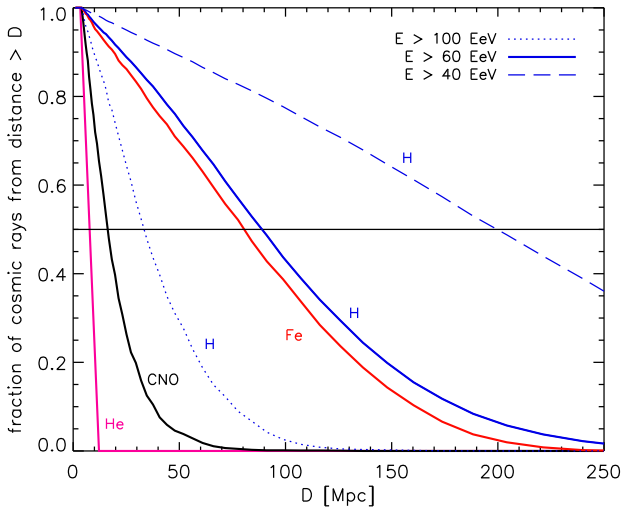

Figure 3.1 Fraction of cosmic rays that survives propagation over a distance larger than D. The different nuclei can travel very different distances in the cosmos. From [103].

Muon number and atmospheric depth of maximum

The two results from the extended Heitler model (chapter 1) concerning the number of muons and the atmospheric depth of maximum can be retrieved here. In equation 1.9, an estimation of the ratio of the muon number between primaries was carried out, obtaining an expression dependent on the atomic number (A) and the pion multiplicity (β). The number of muons for each particle does depend on the energy (see equation 1.8), so to estimate this number in an absolute way, and to use it as a tracer for the mass A, the energy of the primary has to be independently measured with a small systematic uncertainty. In equation 1.10, the difference in $X_{\max}$ for different primaries was calculated, finding a dependence on the atomic number exclusively. The model is applied to the case of proton and iron ($A = 56$). Assuming $\beta = 0.85$ (for a pion multiplicity $N_\pi = 5$), the ratio between the number of muons is ~ 1.8,

that is, according to the model, extensive air showers induced by irons have about 80% more muons that those produced by protons. For $X_{\max}$, being $X_0 = 36.62\,\mathrm{g/cm^2}$, the difference between the two primaries calculated by the model is $\sim 150\,\mathrm{g/cm^2}$. Even if these estimations are based on a simplified model, the dependence of the observables $X_{\max}$ and N_μ on the mass of the primary particle (A) is reliable. This reliability of the extended Heitler model can be tested also through simulations. To deeper investigate the dependence of these two observables on the mass of the primary particle, showers of protons and iron nuclei simulated with EPOS LHC at fixed energy (10 EeV) and fixed zenith angle (38°) have been analyzed. This zenith angle is a particular one because it is the average zenith angle of all the events collected at Auger above a threshold in S_{1000} [136].

The muon number can be expressed, in the case of Auger, as the average muon number at 1000 m (N^{μ}_{1000}), an observable obtained from simulations that indicates the number of muons entering in the WCD at that distance. N_μ and the observable N^{μ}_{1000} rise almost linearly with the energy. This dependence is such that the resolution on the measure of the energy is translated into the resolution of N^{μ}_{1000}. Besides, the Poisson fluctuations limit the resolution achievable, as the mean number of muons entering the tank at 1000 m is lower than 40 for an extensive air shower with 10 EeV (from the MC analysis). The total number of muons itself does not suffer a fluctuation big enough to be taken into account. The Poisson fluctuations of the number of muons arriving at the detector, the resolution on the measure of the energy, and the measure of the observable itself are the limitations. In figure 3.2 (left) the distribution of N^{μ}_{1000} is shown for extensive air showers induced by 10 EeV protons and iron nuclei. A fixed energy is simulated but an energy resolution of 12% (this value is an achievable value for Auger and other observatories) is propagated to N^{μ}_{1000}, spreading the distribution, to account for a more realistic situation. No resolution on the measure of N^{μ}_{1000} is considered. A resolution of about 10 to 20% for the measure of N^{μ}_{1000} would be acceptable, as lower values would be masked by the Poisson fluctuations (15% calculated for 40 muons). It is seen from the distributions that the ratio between the muon mean number for the two primaries is ~ 1.3 (for 1.8 predicted by the extended Heitler model).

In figure 3.2 (right) the distribution of $X_{\max}$ is shown for the same set of showers. The simulations show that the $X_{\max}$ of the two primaries differs by about 80 to $100\,\mathrm{g/cm^2}$ (for $150\,\mathrm{g/cm^2}$ predicted by the extended Heitler model). Because an iron nucleus produces an extensive air shower which is basically a superposition of 56 lower energy proton showers, the fluctuations of $X_{\max}$ around the mean for iron are smaller than for protons. The distribution of $X_{\max}$ for iron primaries has a root mean square (rms) below $30\,\mathrm{g/cm^2}$ ($18\,\mathrm{g/cm^2}$ for this energy), whereas for protons goes up to near $70\,\mathrm{g/cm^2}$. The fluctuations are, thus, of the same magnitude as the difference in the mean $X_{\max}$ of the distribution for both primaries. A resolution of about $20\,\mathrm{g/cm^2}$ for $X_{\max}$ would be acceptable, as lower values would be masked by the shower-to-shower fluctuations. These shower-to-shower fluctuations are the first main difficulty to infer the cosmic ray mass composition and they are expected for any observable related with $X_{\max}$ considered, essentially, because it is a consequence of the intrinsic fluctuations in the shower development. In the represented $X_{\max}$ no resolution from the detector is considered, and as the dependence with the energy is not as strong as in the case of N^{μ}_{1000}, its uncertainty has not been propagated to the $X_{\max}$.

The merit factor (MF) measures the separation between two different distributions, and here it indicates the maximum separation achievable. The MF between the two distributions is

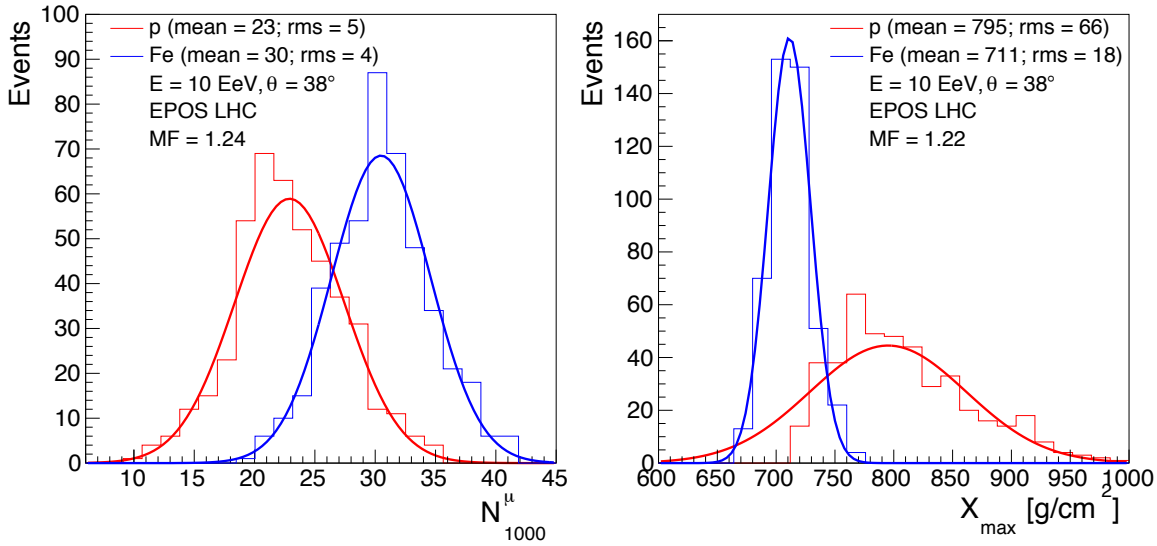

Figure 3.2 Distribution of N^{μ}_{1000} (left) and $X_{\max}$ (right) for protons and iron nuclei (10 EeV and 38°). Showers have been simulated with EPOS LHC. The mean and the rms of the distributions are between parenthesis. The merit factor (MF) is indicated (see text for the definition).

calculated as:

$$\mathrm{MF} = \frac{|\mu_{Fe} - \mu_p|}{\sqrt{\sigma^2_{Fe} + \sigma^2_p}} \tag{3.1}$$

where μ is the mean of the distribution and σ is its root mean square. For the cases exposed in figure 3.2, the merit factor (separation) achieved is 1.22 for $X_{\max}$ and 1.24 for N^{μ}_{1000}.

Combination of muon number and atmospheric depth of maximum

Another aspect must be highlighted. The two observables, $X_{\max}$ and N^{μ}_{1000}, as long as their measurements are derived from different methods, are statistically independent. Then, a two-dimensional analysis would significantly improve the separation power. In figure 3.3 (left) it is shown the distribution of $X_{\max}$ versus N^{μ}_{1000} in a two-dimensional plot. In this scattered plot it can be seen that the correlation between the two parameters is not strong. Furthermore, protons and iron nuclei are easily distinguishable. A linear discriminant analysis (LDA) can be applied to this case. The basis of the analysis is to find a vector such that the projection of the points of the space (N^{μ}_{1000},$X_{\max}$) onto the vector maximizes the separation. The projection creates a new parameter that combines N^{μ}_{1000} and $X_{\max}$. It is carried out onto the vector normal to the discriminant hyperplane ($\vec{w}$), and based on this vector, the new

multi-dimensional parameter (W_m) can be defined as:

$$W_m = \vec{w} \cdot \vec{P} \tag{3.2}$$

where $\vec{P}$ is the vector defined by the points in the (N^{μ}_{1000},X_{max}) space. The separation between the populations can be measured using the Fisher separation coefficient (S_{fisher}) [137], defined as the ratio of the variance between the proton and iron primaries to the variance within the two:

$$S_{fisher} = \frac{\sigma^2_{between}}{\sigma^2_{within}} = \frac{(\vec{w} \cdot \vec{\mu}_p - \vec{w} \cdot \vec{\mu}_{Fe})^2}{\vec{w}^T \Sigma_p \vec{w} + \vec{w}^T \Sigma_{Fe} \vec{w}} = \frac{(\vec{w} \cdot (\vec{\mu}_p - \vec{\mu}_{Fe}))^2}{\vec{w}^T (\Sigma_p + \Sigma_{Fe}) \vec{w}} \tag{3.3}$$

where $\vec{\mu}_p$ and $\vec{\mu}_{Fe}$ are the respective means for proton and iron, defined by the means of the respectives variables. Σ_p and Σ_{Fe} are their respective covariances, always in the two-dimensional space. Then $\vec{w} \cdot \vec{\mu}_p$ and $\vec{w} \cdot \vec{\mu}_{Fe}$ are the means of the projections of the observables onto the direction of $\vec{w}$. Applying this expression, the vector $\vec{w}$ that maximizes S_{fisher} can be found. The maximum separation occurs when:

$$\vec{w} = (\Sigma_p + \Sigma_{Fe})^{-1} (\vec{\mu}_p - \vec{\mu}_{Fe}) \tag{3.4}$$

The discriminant hyperplane is, in this particular case, the dashed line in the scattered plot of figure 3.3 (left). This dashed line, perpendicular to the vector $\vec{w}$, divides the plane into two spaces, and it has been tuned with a y-intercept that leaves almost one kind of primary at each side.

The distributions of W_m for protons and iron nuclei are shown in the right panel of figure 3.3. The projection of the points onto the direction of the vector $\vec{w}$ represents, essentially, the algebraic distance from each point to the dashed line. This distance depends on both observables, as indicated in the label of the X-axis of the histogram, where positive values are iron-like events, and negative values indicate proton-like events. This positive/negative separation is artificial. The discriminant hyperplane could be anywhere, but it has been translated to the intermediate region between the populations. This translation is carried out by choosing the correct y-intercept in the function that defines W_m.

The MF between the two distributions of W_m is calculated. Note that MF and S_{fisher} represent the same reality and they are related by MF $\sim \sqrt{S_{fisher}}$. The value found for MF (1.91), higher than the MF of the observables alone (1.22 and 1.24), indicates that the combination of the observables improves the power of the analysis. The first main difficulty introduced above for the mass composition is the shower-to-shower fluctuation, but this result indicates that despite this, a good separation is, in principle, possible, if both X_{max} and N^{μ}_{1000} are measured with good enough resolution (10 to 20% for N^{μ}_{1000} and 20 g/cm^2 for X_{max}), and independent methods. Different energies, zenith angles and models give different separation values. This value is the maximum separation, obtained from the simulated values of X_{max} and N^{μ}_{1000}. Any analysis based on reconstructed parameters derived from X_{max} or N^{μ}_{1000} gives necessarily lower separation values than those achieved with the simulated observables.

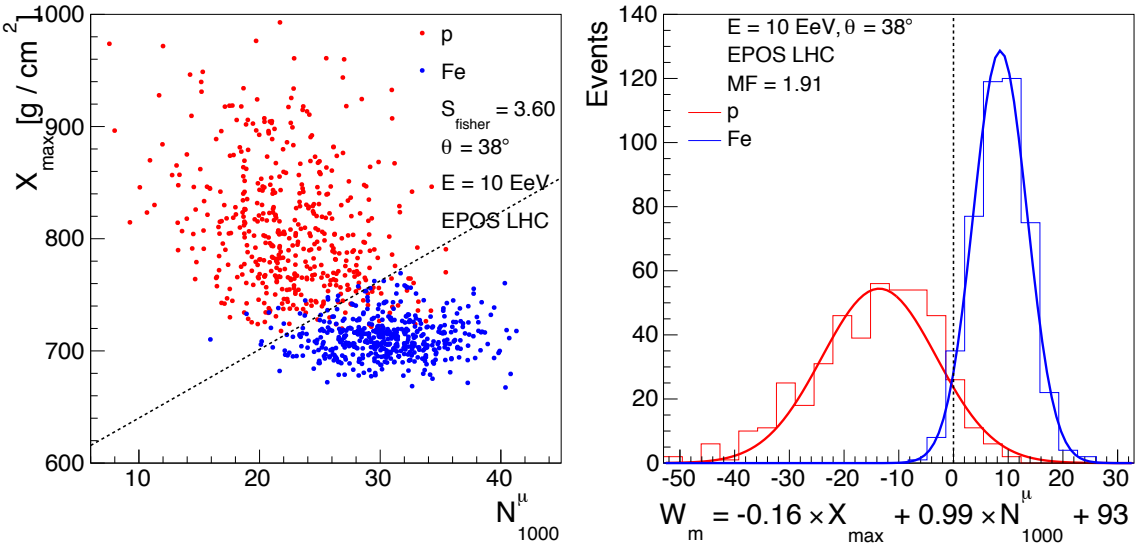

Figure 3.3 Two-dimensional analysis for $X_{\max}$ versus N^{μ}_{1000} for protons and iron nuclei at 10 EeV and 38° zenith angle. Showers simulated with EPOS LHC. Left: distribution of $X_{\max}$ versus N^{μ}_{1000} in a two-dimensional plot. Right: combination of both parameters into the new parameter W_m. The Fisher separation coefficient and the merit factor are indicated.

Extrapolation from hadronic interaction models

The second main difficulty to measure the mass composition of cosmic rays is derived from the uncertainties in the hadronic interaction models. Electromagnetic showers can be modeled without any significant uncertainty. However, for hadronic showers, already at 10^{18} eV, the center of mass energies of the first nucleus-air interactions are beyond those achievable at the LHC. The consequence of this is that the systematic uncertainty introduced by the extrapolation of the hadronic interaction models tuned at much lower energies is extremely difficult to quantify. In addition, a significant discrepancy in the number of muons produced in the extensive air shower development exists between models. This is a major problem, because the number of muons produced in the shower is one of the characteristics that can differentiate a proton induced shower from an iron one. Due to shower-to-shower fluctuations and uncertainties, an event-by-event analysis is not possible, but a statistical approach can be followed. This statement is reinforced when considering that cosmic rays can also be intermediate nuclei, merging the distributions even closer when they are included in the analysis.

3.2 Measuring N_{μ} and $X_{\max}$ at the Pierre Auger Observatory

In this section the different methods used in the Auger to obtain N_{μ} and $X_{\max}$ are discussed, along with the most important findings.

Muon number

The extraction of the muon number in Auger is a difficult task. The current configuration of the observatory does not allow the direct measure of the muon component. This has to be inferred with different indirect methods. As already seen in section 2.2, hybrid events have been exploited to that aim, that allowed the finding of a deficit of the muon content in the hadronic interaction models.

Muon number in inclined events. The hybrid events are also used by the Pierre Auger Collaboration to measure the average muon number in extensive air showers with zenith angles between 62° and 80°, and the evolution of this number between 4×10^{18} eV and 5×10^{19} eV [138]. At this zenithal angles, the electromagnetic component of the cascade is highly absorbed, and the unabsorbed muonic component is dominant.

The muon number is measured using a scale factor, N_{19}, which relates the observed muon densities at the ground to the average muon density profile of simulated extensive air showers induced by a proton of fixed energy 10^{19} eV. With this parameter, the muon density ρ_μ at the ground point $\vec{r}$ is modeled as:

$$\rho_\mu(\vec{r}) = N_{19}\rho_{\mu,19}(\vec{r};\theta,\phi) \tag{3.5}$$

where $\rho_{\mu,19}$ is the parameterized ground density for a proton shower simulated at 10^{19} eV with the hadronic interaction model QGSJet-II-03. The scale factor N_{19} is inferred from measured signals with a maximum-likelihood method based on a probabilistic model of the detector response to muon hits obtained from simulations. A residual electromagnetic signal component is taken into account based on model predictions (typically 20% of the muon signal).

Large sets of protons and irons are simulated with QGSJet01, QGSJet-II-04 and EPOS LHC. For every event in the simulation, the total number of simulated muons N_μ is divided by the total number of muons $N_{\mu,19} = \int \mathrm{d}y \int \rho_{\mu,19}\mathrm{d}x$ obtained by integrating the reference model. This ratio (R_μ^{MC}) is compared with the value of N_{19} obtained from the fit of equation 3.5. The small deviation observed between N_{19} and R_μ^{MC} indicates the universality of the chosen reference profile and validates the reconstruction process. This allows the construction of an unbiased estimator, R_μ, of the total muon number at the ground.

Going back again to the Heitler model, from equation 1.8, it is expected that the average number of muons (proportional to $< R_\mu >$) and the energy have a relation not far from a power law. Therefore a parameterization with the shape $< R_\mu >= a(E/10^{19}\,\mathrm{eV})^b$ can be applied to the data set. The fit is carried out with 174 selected hybrids events, returning values for a and b. $< R_\mu >$ can then be expressed as a function of the energy, and compared with the predictions for the muon content for proton and iron for different models. The result is shown in figure 3.4 (left), where the ratio $< R_\mu > /(E/10^{19}\,\mathrm{eV})$ is shown versus energy: the data suggest a composition heavier than iron. This is not in agreement with the studies based on $X_{\max}$, exposed in the next subsection. Taking into account the Auger $X_{\max}$ measurements, it can be concluded that it exists a deficit of the muon content in simulations of 30 to 80% at 10^{19} eV, depending on the hadronic model.

Muon fraction from the timing information of the SD traces. A different approach to measure the muon content consists in using the FADC traces in the WCDs, by applying

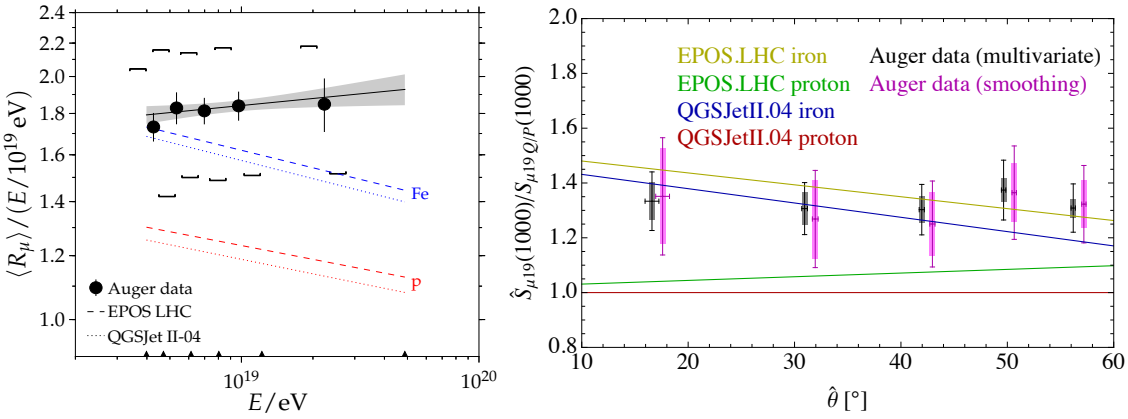

Figure 3.4 Left: average muon content $< R_\mu >$ per shower energy E as a function of the shower energy in double logarithmic scale. The data (black points) are shown with the fit (black solid line) carried out with the parameterization explained in the text. Square brackets indicate the systematic uncertainty of the measurement. The curves for proton and iron showers simulated at zenithal angle 67° (dotted and dashed lines) are also shown. From [138]. Right: the measured muon signal rescaling at 10^{19} eV and at 1000 m from the shower axis versus zenith angle, with respect to QGSJet-II-04 proton as baseline (denoted as $S^{Qp}_{\mu,19}$). The predictions of the hadronic interaction models for proton and iron are also represented. From [139].

different filtering techniques to the temporal distribution of the signals [139]. With these techniques it is possible to separate the electromagnetic and muonic components of air showers. In this study, the muonic component is considered only as the signal in the station produced by muons entering in the detector, leaving as part of the electromagnetic component the electromagnetic halo produced by muon interactions and muon decay in the atmosphere.

The time response profile of individual particles in the WCD is the same for all of them: a quick rise followed by an exponential fall with a decay time of about 60 ns. But other two features can be used to separate traces coming from different particles. The first is the amplitude distribution of the particle response. The amplitude of a muon is close to a Gaussian of mean 1 VEM. The mean amplitude of a single electromagnetic particle is much smaller and the number of them entering the detector is, on average, an order of magnitude larger than the number of muons. The second feature to distinguish between the traces is the time-of-arrival distributions. Muons typically arrive earlier than electromagnetic particles. Analysing both features, it is concluded that muon signals are short and spiky, and the electromagnetic signals are long and smooth. One main source of uncertainty is due to high energy photons (> 300 MeV), as they produce a signal similar to that of a muon.

Two methods have been used. The first is a multivariate method. A large number (~ 50) of FADC signal observables are extracted, and the muon fraction is estimated using a multivariate regressor. The second method is the smoothing method. This consists in applying a low-pass filter a few times on the signal to gradually separate the low-frequency smooth electromagnetic component from the high-frequency component which is assigned to muons.

All the stations in the range between 950 and 1050 m, in events with zenithal angle lower than 60° and with energy between $10^{18.98}$ and $10^{19.02}$ eV are selected. In these stations the muon fraction is estimated and averaged according to the zenithal angle. An increasing muon fraction with increasing zenithal angle is found, as predicted by the models. Afterwards, the total signal of each station can be multiplied by the measured muon fraction to obtain the muon signal. As the station signal depends on the energy, a rescaling procedure is carried out to translate the total signal in the station to the projected signal as if it would be in a 10^{19} eV event. The results of the two methods are in very good agreement. The measured muon signal is represented in figure 3.4 (right), along with the predictions of the models for proton and iron. The measured fraction of the muonic to total signal is bracketed by model predictions for proton and iron primaries obtained with CORSIKA and QGSJet-II-04 and EPOS LHC.

Besides these two analyses, the information that the muons carry is also explored from the point of view of the arrival times to the ground. But this information does not return the muon number, but the origin of the muon, and consequently, to the longitudinal development of the shower. This will be seen in the next subsection.

Atmospheric depth of shower maximum

The correlation of $X_{\max}$ with the mass of the primary has been exploited by the Pierre Auger Collaboration to study the composition of cosmic rays at different energies. The FD measures this observable with a resolution of about 20 g/cm^2, although this value changes with the energy (figure 3.5), going from 26 g/cm^2 at $10^{17.8}$ eV down to about 15 g/cm^2 above $10^{19.3}$ eV. Different individual contributions are responsible for this resolution. The detector itself is the largest source of uncertainty. It accounts for the uncertainties derived from the Poisson fluctuations of the number of photoelectrons detected for each shower. The number of photoelectrons detected increases with energy and, correspondingly, the resolution improves. The alignment of the telescopes and the relative timing between the FD and the SD also affect the resolution of the detector. The other contributions are the measurements of the aerosols and the uncertainties in the atmosphere density profiles as a function of height.

Measurements of $X_{\max}$ with the FD. The first results about the measurements of $X_{\max}$ in Auger were published already in 2010 [108]. The measurements of $< X_{\max} >$ versus energy yielded different elongation rates for energies below and above $10^{18.24}$ eV. Although $X_{\max}$ was already used by other observatories [141, 142], the statistics achieved by these observatories above 10^{19} eV was limited and the measurement of dispersion of the atmospheric depth of maximum ($\sigma(X_{\max})$) was not included. The events collected by Auger until that date already hinted for a change in the composition, pointing at a heavier composition above the cited energy. A careful interpretation of the data, along with the description of the method used for that interpretation was published in 2013 [143]. The two measured observables, $X_{\max}$ and $\sigma(X_{\max})$, were parameterized as functions of the first two moments of the $\ln A$ distribution.

The most recent results for the measurements of $X_{\max}$ and $\sigma(X_{\max})$ are shown in figure 3.6 [140], compared with the predictions of the most recent hadronic interaction models. It suggests that the flux of cosmic rays is composed of predominantly light nuclei at around $10^{18.3}$ eV and that the fraction of heavy nuclei is increasing up to energies of $10^{19.6}$ eV, the maximum observed.

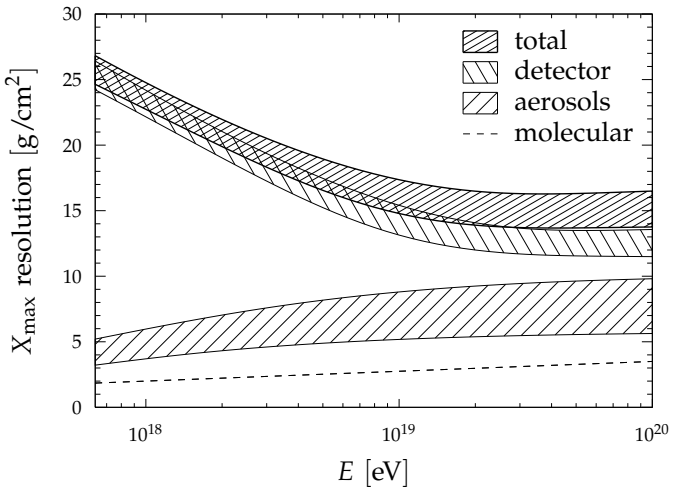

Figure 3.5 Resolution of $X_{\max}$ measured with the FD as a function of the energy. The bands denote the estimated systematic uncertainties. From [140].

Other primaries in the analysis. At the beginning of this chapter a justification was given for the consideration of proton and iron in the analysis. In figure 3.6 the predictions of the models are shown for this two primaries. But as the values of the measured $X_{\max}$ and $\sigma(X_{\max})$ are between both primaries, it is natural to wonder if this is because there is a mix of the two primaries, or because there are other primaries with intermediate masses. The distribution of $X_{\max}$ are compared with the simulated distributions due to mixtures of different primaries, including not only proton and iron, but also helium and nitrogen, as representatives of the intermediate range of nuclear masses [135]. When only proton and iron are included in the mixture, none of the hadronic models can describe the data. However, if intermediate primaries are also included, the models give acceptable fit qualities. The quality of the fit is measured by the p-value, which is defined as the probability of obtaining a worse fit than that obtained with the data, assuming that the distribution predicted by the fit results is correct. Results (see figure 3.7) from EPOS LHC simulations favour a mixture dominated by nitrogen nuclei, whereas the QGSJet-II-04 simulations favour helium nuclei. Sybill 2.1 modeling leads to a mixture of the two. For all models, the observed proton fraction goes from a value of about 60% in the region of the *ankle* ($\sim 10^{18.2}$ eV) to near zero just above 10^{19} eV and a possible resurgence at higher energies. None of these models supports a large contribution from iron nuclei.

Muon production depth (MPD) analysis. Other parameters related with $X_{\max}$ can be measured using the SD. The muonic atmospheric depth of maximum ($X^{\mu}_{\max}$) can be reconstructed from the information in the MPD [144]. The arrival times of the muons, measured using the FADC traces of stations located far from the shower core, allow the reconstruction of their geometrical production heights along the shower axis. This is only possible for showers where the electromagnetic component is highly absorbed before reaching the ground, mostly horizontal air showers (showers with $\theta > 60°$), although the analysis has been extended down to 50°. $X^{\mu}_{\max}$ is defined as the point along the shower axis where the

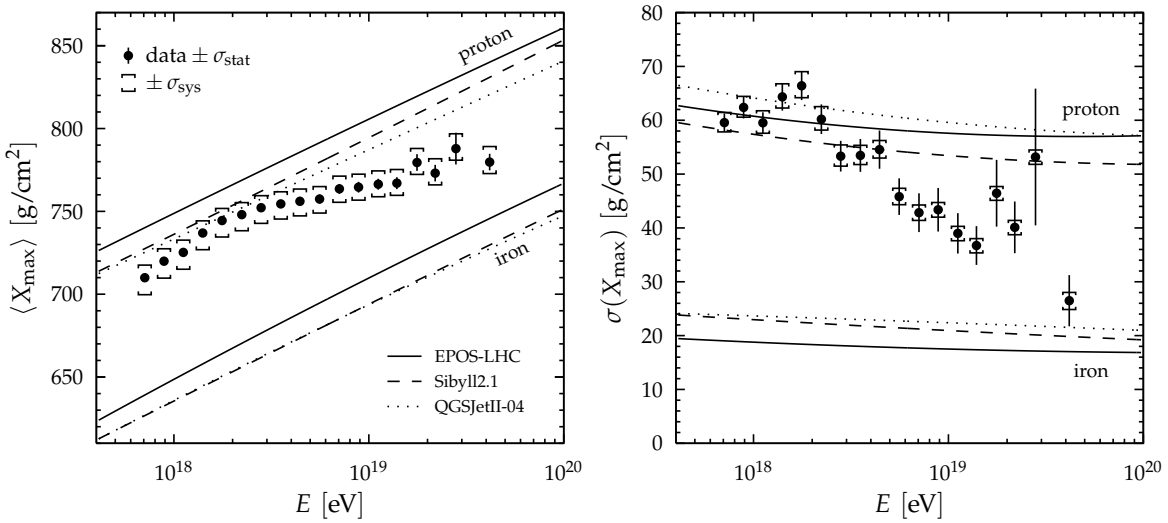

Figure 3.6 $X_{\max}$ and $\sigma(X_{\max})$ measured in the FD of the Pierre Auger Observatory for different energies compared with different hadronic interaction models. From [140].

production of muons reaches its maximum as the shower develops through the atmosphere. This parameter is closely related to $X_{\max}$ (see left panel in figure 3.8). The measured $X^{\mu}_{\max}$ is shown in the right panel of figure 3.8, for events with zenith angle between 55° and 65°. The current level of systematic uncertainties associated with its determination renders difficult any conclusive statement on mass composition. The possibility of its usage for constraining hadronic interaction analysis is also discussed in the cited publication.

Other parameters, related with the shape of the shower front, are also derived from the SD. The resolution achieved with them is not enough to be useful in the analysis for hadronic composition. They are used in the searches for photons and neutrinos, as detailed in the next section.

3.3 Photons, neutrinos and neutrons

The identification of neutral cosmic ray primaries, like photons, neutrinos or neutrons, is of great interest because their arrival directions point directly to the sources. Galactic and extragalactic magnetic fields do not affect their respective paths to the Earth.

Showers induced by photons and neutrinos have singular characteristics and their identification relies on specific analyses. A sketch of the main differences is proposed in figure 3.9, where extensive air showers induced by protons, iron nuclei, photons and neutrinos are schematically represented. In this figure they are summarized the main characteristics of the different showers, that, at this point, are worthy to be listed together. First, the interaction point of protons and photons is about $45\,\mathrm{g/cm^2}$, being a bit shallower for iron nuclei and really deeper for neutrinos. Although the first interaction point of photons is at the grammage level

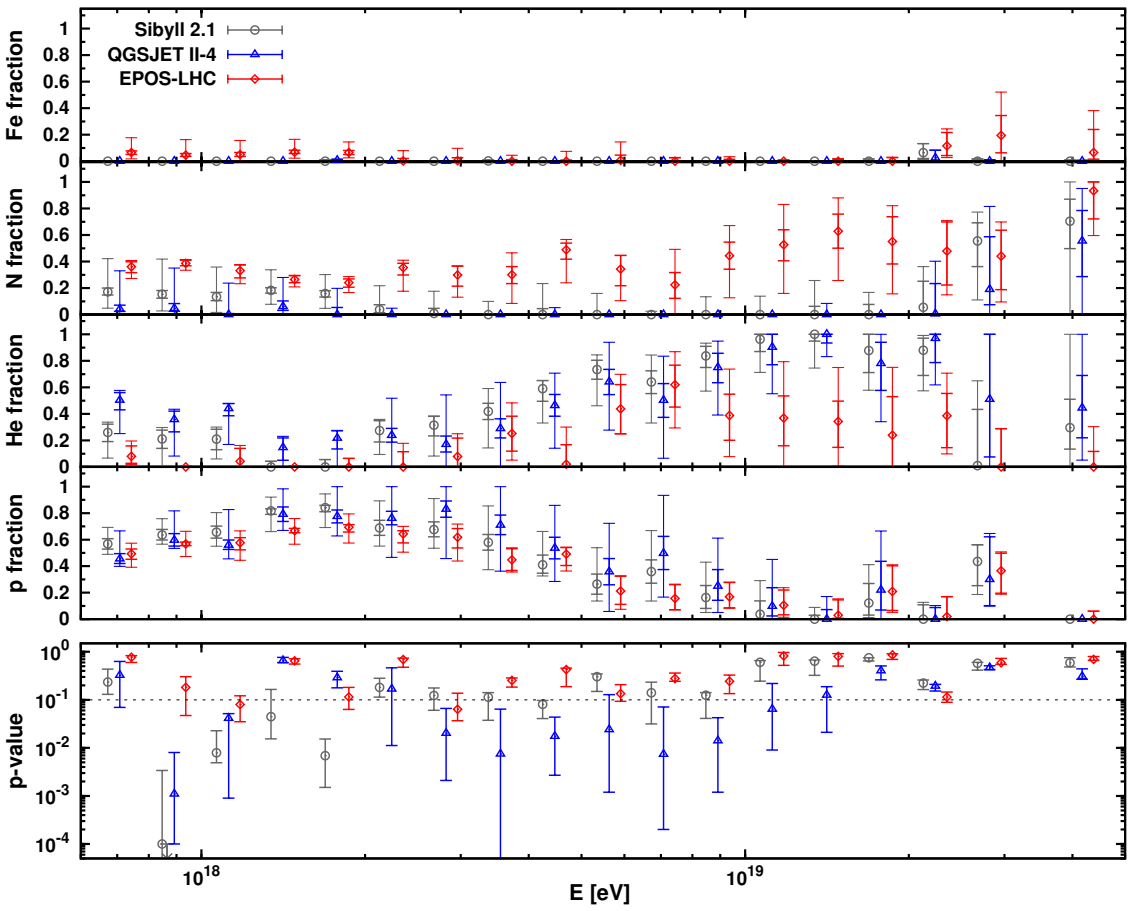

Figure 3.7 Fitted fraction and quality for the scenario of a complex mixture of protons, helium nuclei, nitrogen nuclei, and iron nuclei. The upper panels show the species fractions and the lower panel shows the p-values. From [135].

of protons, they develop much slower, being the maximum deeper than in the proton case. Second, the number of generated muons changes, being really small for photons, higher for protons, and a bit higher for iron nuclei.

Although neither photons or neutrinos have been detected in the Pierre Auger Observatory, the possibility of their detection allows the establishment of upper limits to their respective fluxes.

Photons

Extensive air showers induced by photons have two main characteristics. First, their interaction length is longer than in the hadronic case and the development of the shower is slower because they essentially interact by pair production (electron-positron) and Bremsstrahlung. Both factors favour a very deep $X_{\max}$, distinguishable from the one expected for hadrons. And

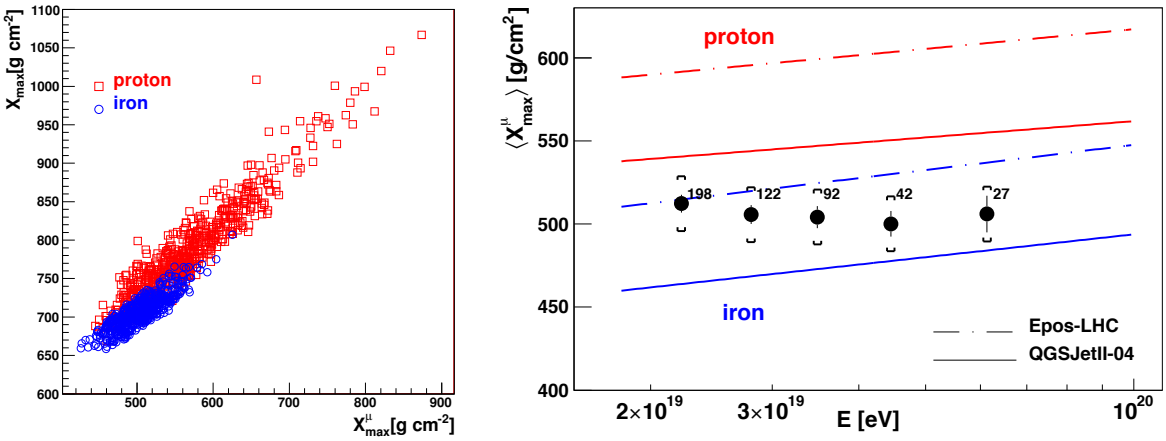

Figure 3.8 Left: $X^{\mu}_{\max}$ versus $X_{\max}$ for simulated proton and iron. Right: the measured $X^{\mu}_{\max}$ presented for different energies compared with different hadronic interaction models. From [144].

second, the cross section expected for processes involving the creation of muons is very low. Then, a smaller number of muons is expected in comparison with the hadronic case [145].

The identification of a photon with the FD is very easy, as the difference in $X_{\max}$ between photon and proton is larger than 100 g/cm^2. However, due to this large difference, some derived methods to extract $X_{\max}$ with SD measurements can also be also exploited. A few characteristics are indicative of the nature of the primary particle.

The curvature of the shower front is due to the delay of the particles far from the shower axis, with respect to those travelling close to it. The particles, while they travel through the atmosphere, form a shower front that, with an oversimplification, can be described as spherical. A relatively planar shower front (large radius of curvature) indicates that the particles were generated high in the atmosphere, whereas particles generated deeper generate a front with a small radius. A large radius of curvature thus indicates a small $X_{\max}$.

The width of the shower front can be measured using the rise time of a single station. The rise time is defined as the time that it takes to increase from 10% to 50% of the total signal deposited in the station. The rise time, evaluated at a fixed distance from the axis, can be calculated, and gives information about the width of the shower front. The width is larger if the shower has a large electromagnetic component compared with the muonic one, as they suffer a bigger scatter in their path through the atmosphere. From a geometrical point of view, particles with origins deep in the atmosphere produce a longer rise time than those that come from the earliest stages of the shower. Small values of the rise time indicate small values for $X_{\max}$ [146]. The rise time is a characteristic of the time structure of the arrival muons (related then with $X^{\mu}_{\max}$, and consequently with $X_{\max}$), but a small and secondary influence of N_{μ} can be appreciated.

Using these observables, the Auger Collaboration has presented upper limits to the fraction of photons [147, 148] and to the flux [146]. An updated photon flux is shown in figure 3.10,

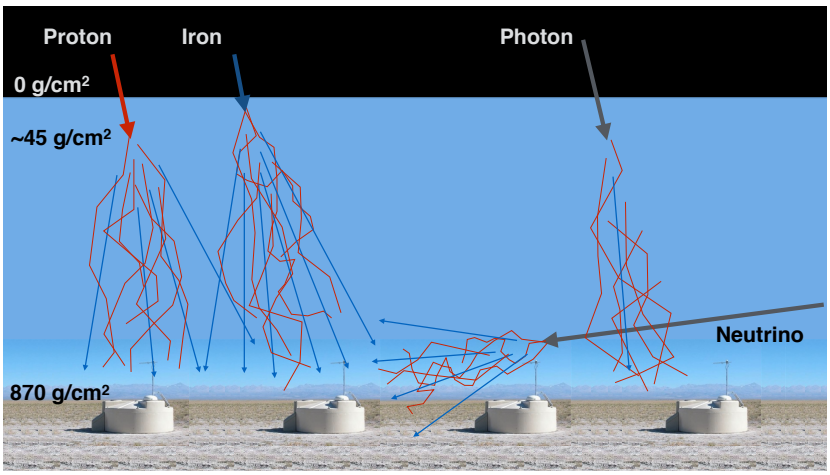

Figure 3.9 Sketch of the evolution of the extensive air showers induced by different primaries: proton, iron, photon and neutrino, represented by the thick arrows. The scattered red lines represent the electromagnetic component, absorbed in a few hundreds of g/cm^2. The straight blue thin arrows represent the muonic component, that can traverse the whole atmosphere. Neither the detector or the components of the extensive air shower are scaled.

with the limits calculated with the hybrid data set and the SD. The photon limit imposed by Auger has discarded the so-called *top-down* models.

The capacity to discriminate photons has also been used by the Collaboration to search for point sources of EeV photons [150]. No photon point source has been detected and an upper limit on the photon flux has been derived for every direction.

Neutrinos

Two analyses have been performed in Auger to search for neutrinos. The first one searches for extensive air showers induced by downward-going neutrinos of all flavours as they interact with the atmosphere. The second one searches for upward-going τ neutrinos as they interact with the rock of the Earth. This is called the Earth-skimming mechanism.

As neutrinos interact very weakly, the search for downward-going neutrinos assumes that extensive air showers with a deep $X_{\rm max}$ are, with high certitude, not a proton or heavier particle, as they interact very early in the atmosphere. This search is focused on arrival zenithal angles higher than 60°, where MC simulations show that the search is more efficient. A precise measure of $X_{\rm max}$ or $X^{\mu}_{\rm max}$ is not needed, because a very horizontal air shower with electromagnetic component still not extinguished would be sufficient to identify it as a neutrino shower. Down-going neutrinos can be detected with SD, as they are easily distinguishable from regular hadronic cosmic rays by the broad time structure of their shower signals in the WCDs [151].

The neutrino, indeed, is more likely that interact in the rock of the Earth a few degrees below the horizon (Earth-skimming mechanism). The possible interaction with the rock of the

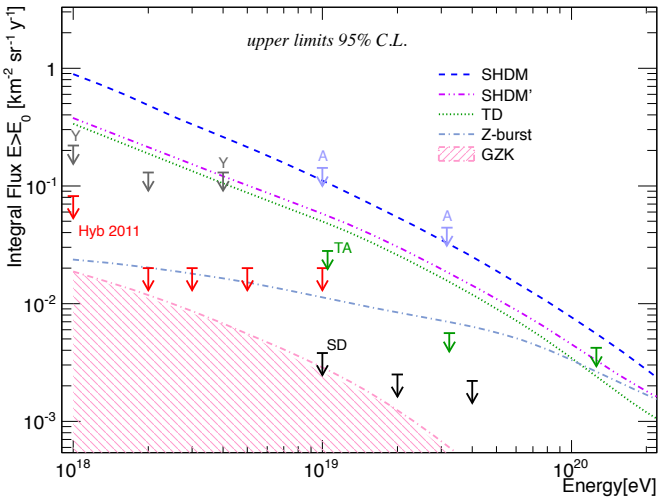

Figure 3.10 Upper limits to the integral photon flux derived by Auger with the hybrid measurements (Hyb 2011, red) and SD alone (SD, black). The Auger results are compared with those by AGASA (A, blue), Yakutsk (Y, grey) and Telescope Array (TA, green). The shaded region and the lines give the predictions for the GZK photon flux and for *top-down* models. From [149].

Earth is used to search for τ neutrinos. They are rarely produced in particle interactions, but they might be the result of oscillations in the propagation to Earth. While at production the neutrino flavour ratio (ν_e:ν_μ:ν_τ) is close to 1:2:0, after propagation it is close to 1:1:1. The τ neutrino may interact with the rock of the Earth and produce a very penetrating τ lepton. This τ lepton, after a few kilometres, may decay producing a very horizontal air shower.

Finally, considering both mechanisms, three different sets of identification criteria were established to maximise the discrimination power. The selections exploit the different characteristics of the showers in each angular bin as determined from MC simulations. The three selection cuts are the Earth-skimming (ES), for $\theta > 90°$, the downward-going high angle (DGH), for $75° < \theta < 90°$, and the downward-going low angle (DGL), for $60° < \theta < 75°$. The analysis in the three sets begin with a trace cleaning to remove, mainly, atmospheric muons. After the inclined showers are identified, and a selection based on the shower shape is done. The MC calculations show that there is no chance for a nucleus or a photon to generate a shower with a $length(L)/width(W)$ ratio higher than 5, for the ES, or 3, for the DGH. The speed of the shower through the array is also used to select event in the ES and DGH. The arrival times at the stations are requested to be compatible with the time that the light takes to go from one station to the next, selecting showers that move through the array at roughly the speed of light. Selection criteria based on the ToT and area over peak (AoP) of the signals are also carried out in the three sets.

The absence of candidates in these searches is used to place an upper limit to the diffuse flux of the neutrinos at EeV energies [152–154]. The most recent neutrino limit published from Auger data is shown in figure 3.11.

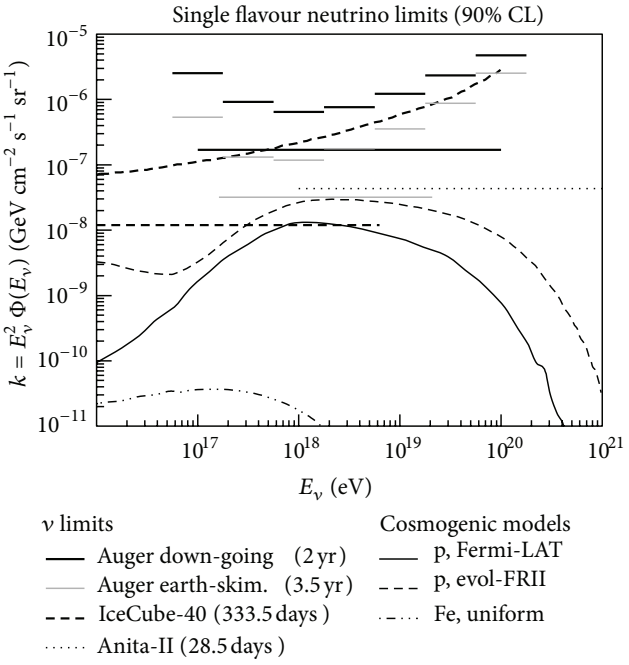

Figure 3.11 The neutrino integrated limits scaled to single flavour published by Auger and other ultra-high energy cosmic ray experiments compared with different cosmogenic models. From [154].

As for the photons, a search for point-like sources of ultra-high energy neutrinos has been performed. Upper limits at 90% CL have been established [155].

Neutrons

Although the neutrons search is more a search for point sources than a composition problem, it is still worthy to be mentioned. Extensive air showers induced by neutrons are not distinguishable from those induced by protons. The only difference does not reside in the development, but in its way from the source to Earth. Whereas protons and other charged nuclei are affected by the Galactic and extragalactic magnetic fields, neutrons are not. An excess of cosmic ray air showers arriving from a specific astrophysical source could spot a neutron source. Since free neutrons undergo beta decay with a mean lifetime of about 886 s at rest [27], the mean travel distance for relativistic neutrons is $9.2 \times E$kpc, where E is the energy of the neutron in EeV. The distance from Earth to the Galactic center is about 8.3 kpc [156], and the radius of the Galaxy is approximately 15 kpc. Sources in part of the Galactic disk, including the Galactic center, should be detectable via neutrons above 1 EeV. Above 2 EeV, the volume for detectable neutron emitters includes most of the Galaxy. The search for these spots has been performed focusing on the Galactic center and the Galactic plane. Each candidate source is weighted in proportion to its electromagnetic flux, its exposure to the observatory, and its flux attenuation factor due to neutron decay. The search has not found evidence for a neutron flux

from any class of candidate sources, establishing only upper limits to the fluxes. These limits on fluxes of neutrons significantly constrain models of EeV proton emission from non-transient discrete sources in the Galaxy [157].

3.4 Implications of the composition measurements

Astrophysical implications

Several results have been presented in this chapter. Any interpretation derived from the data at ultra-high energies needs a caveat: the mass can only be inferred under assumptions on the models, being these only extrapolations from measurements at lower energies. Regarding the mass determination of the hadronic primaries, this can be summarized in two important items. First, the proton fraction has been determined for different energies, rising to over 60% around the *ankle*, dropping to near zero above and showing a possible resurgence at higher energies. And second, the interpretation of Auger $X_{\max}$ data in terms of fractions of different primary nuclei suggests the presence of other different primaries with intermediate masses heavier than proton and lighter than iron, even if the models do not agree on the suggested primary. Whereas the light composition observed around 10^{18} eV is in agreement with the results published by HiRes and Telescope Array, at higher energies the suggested heavier composition cannot either be confirmed or disproved by the other observatories. It is important to remark that the level of agreement depends on the interaction model used to interpret the results [109].

The *ankle transition models* predict a heavy Galactic component and a proton extragalactic component, being the *ankle* the transition between them. The *dip model* predicts pure proton composition for the extragalactic component, and it extends their dominance to energies below the *ankle* (see section 2.1). The predictions of these two models do not agree with the high proton fraction in the energies of the *ankle* and the heavier composition in energies above, as suggested by Auger. An important implication of the heavier composition for the extragalactic cosmic rays is that the possibility to identify the sources is reduced as the magnetic deviation is stronger.

The limits established for photons and neutrinos have already ruled out most of the *top-down* models, but they are not yet at the level to elucidate the existence of the GZK by-products. Nevertheless, the flux limit has been set so close to that expected by the GZK effect, that a confirmation or discard of their existence will be possible in the near future.

Implications on the methodology

There are not many observables available for the determination of the composition of cosmic rays. The FD estimation of $X_{\max}$ is, until now, the one with the best resolution, but it is limited in the duty cycle, and hence in the number of events. The observables extracted from the SD analysis do not have a resolution good enough to distinguish proton from iron. The $X^{\mu}_{\max}$, extracted in horizontal air showers, has a relatively good resolution, but the condition on the zenith angle also limits the number of events, and the current level of systematic uncertainties associated with its determination also limits possible conclusions on the composition. Besides,

possible estimations for N_μ have been shown to be a promising opportunity. The combination of a measure of the muon number with $X_{\max}$-related parameters would improve significantly the mass determination. To develop a combined analysis, the measure of N_μ and $X_{\max}$ has to be carried out by independent methods, and to increase the statistics, with a 100% duty cycle.

The importance of the mass determination has been shown along the last two chapters. The current methods to infer the mass of the hadronic primaries are, despite the efforts done in different approaches, insufficient to clarify the questions discussed above. This thesis proposes three approaches to improve the measurements of the mass composition in the cosmic rays observatories in general, and in the Pierre Auger Observatory in particular. The first approach is to propose the magnetic deflection of secondary particles in horizontal air showers as an alternative method to extract $X^{\mu}_{\max}$. The second approach is to explore the potential of the radio detection to access the longitudinal profile of the extensive air shower with a 100% duty cycle. And the third one is to propose a new kind of WCD with sensitiveness to the muonic component of the shower. These three approaches are conveniently expounded in chapters 4, 5 and 6, respectively.

Chapter 4

Magnetic deviation in horizontal air showers

As seen in chapter 3, the muonic atmospheric depth of maximum ($X^{\mu}_{\max}$) is a parameter with sensitiveness to the mass of the primary particle. The Pierre Auger Collaboration has published a study of $X^{\mu}_{\max}$ (figure 3.8), by analysing the arrival times of muons in horizontal air showers. The current level of uncertainties in the extraction of $X^{\mu}_{\max}$ prevents the Collaboration from making conclusive statements on mass composition. The extraction of this parameter by alternative methods could reduce this uncertainty level, and allow for a statistically based analysis of the mass composition with the muonic atmospheric depth of maximum.

The first approach in this thesis to determine the mass composition is to propose an alternative method to extract the $X^{\mu}_{\max}$ from horizontal air showers. This new analysis can be applied to the data already collected by the Observatory. The magnetic deviations that muons suffer in horizontal air showers are the basis of this alternative method.

The physical effect of the Earth magnetic field on the muons of the extensive air shower is detailed in section 4.1. The indicators proposed to measure this effect are described in section 4.2. The details of the simulations and the data set are explained in section 4.3. The dependencies of these indicators on different observables (φ, θ, energy) are exposed in section 4.4. The dependence of the deflection on the muon profile and the construction of an estimator for the $X^{\mu}_{\max}$ are detailed in section 4.5. The dependence of the deflection on the transverse momentum is studied in section 4.6. Finally, the conclusions and open questions derived from this study are exposed in section 4.7.

4.1 Earth magnetic field and extensive air showers

Nearly horizontal extensive air showers (here they will be considered as those with $\theta > 63°$) have to travel a long path through the atmosphere. The electromagnetic component of the extensive air shower is extinguished in a few hundreds of g/cm^2, so only high energy muons arrive at the detector. The muons are deflected by the transverse component of the Earth magnetic field. In a first approximation, neglecting the energy loss, the transverse displacement (δ) is proportional to the magnetic field perpendicular to the shower axis ($B_{\perp}$),

to the inverse of the muon energy (E_μ) and to the square of the path from production to the ground (L_μ):

$$\delta \propto \frac{B_\perp}{E_\mu} L_\mu^2 \tag{4.1}$$

An evidence for the magnetic distortion in data was first shown inside the Pierre Auger Collaboration [158], and more recently the same analysis was applied to a larger sample of events [159]. In the left panel of figure 4.1 the transverse magnetic field seen by a particle parallel to the shower axis is represented. Muons with opposite charges are deviated in opposite directions, deforming the shape of the shower front. This is the physics principle of the deflection and the basis of the study carried out in this chapter. The shower frame is defined by a polar axis along the shower axis. In the shower plane (perpendicular to the axis) the distance to the axis (r) and the azimuthal angle in the shower plane (ζ) are used. The magnetic North at the Auger site is at $\varphi = 86.5°$ and $\theta = 54.8°$, and the value $\varphi = 0°$ corresponds to the East direction. In the right panel of figure 4.1 it is shown the intensity of $B_\perp$ as a function of the arrival direction of the shower. The intensity of $B_\perp$ changes with both the arrival zenithal angle (θ) and the arrival azimuthal angle (φ). This is important because the deflection suffered by the muons is proportional to the intensity of the magnetic field.

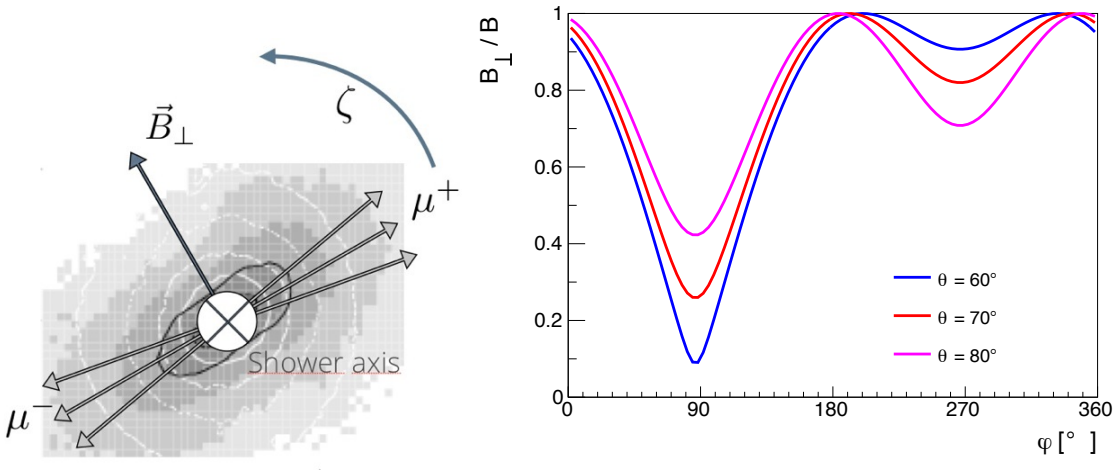

Figure 4.1 Left: deflection due to the geomagnetic field suffered by muons travelling along the shower axis. Right: intensity of the transverse magnetic field as a function of the arrival direction: θ is the zenith angle, φ is the azimuthal angle. The magnetic North at the Auger site is at $\varphi = 86.5°$ and $\theta = 54.8°$, and the value $\varphi = 0°$ corresponds to the East direction.

For horizontal air showers, the distance between the production point of the muons and the ground is large, so the transverse deviation may be large. In fact, it is expectable that the larger the path the muons have to traverse, the larger the deviation they suffer. This deviation is related, then, with the muon production depth, therefore with the $X^\mu_{\max}$.

4.2 Indicators of the deflection

The deflections indicated can be measured with the SD. As the showers to be analysed are inclined, the whole signal in the stations is attributed to the muon component. The methods explored to extract indicators of the deflections are two: the shower shape and the parameterization of the lateral distribution.

Shower shape

The first method to measure the deformation of the ground spot is the determination of the *shower shape*. This parameter has already been introduced in the previous chapter in section 3.3, used for the neutrino searches. The *shower shape* is defined by the width (W) and the length (L). To obtain this parameter it is necessary to determine the main axes of the matrix of inertia of the detectors hit in the event, weighted by the integrated signals S_i produced in each one:

$$I_{xx} = \sum_i S_i(x_i - \overline{x})^2 \ ; \ I_{yy} = \sum_i S_i(y_i - \overline{y})^2 \ ; \ I_{xy} = \sum_i S_i(x_i - \overline{x})(y_i - \overline{y}) \tag{4.2}$$

where $\overline{x}$ and $\overline{y}$ are the barycentres of the stations weighted by S_i. The eigenvalues of this matrix are:

$$\frac{I_{xx} + I_{yy}}{2} \pm \sqrt{\left(\frac{I_{xx} - I_{yy}}{2}\right)^2 + I_{xy}^2} \tag{4.3}$$

The largest eigenvalue is L^2, whereas the smallest is W^2. The angle ϕ of the main axis with the x-axis is such that 2ϕ is the direction of the vector $(2I_{xy}, I_{xx} - I_{yy})$. It should be noted that ϕ does not coincide with the arrival azimuthal angle (φ) of the shower: the tilt ϕ - φ is one of the manifestations of the magnetic distortion.

The matrix of inertia in projection onto the shower plane (perpendicular to the shower axis) is computed to notice the relation between the distortion and the transverse magnetic field. In the absence of magnetic deviation, the projected footprint is practically isotropic around the shower core, except for a slight forward/backward asymmetry which is compensated, at first order, by a translation of the core. In these conditions, the magnetic distortion is characterized by the deviation from 1 of the ratio L/W, and by the value of the direction ϕ of the axis of the ellipse with respect to $B_\perp$.

These quantities are highly sensitive to missing stations, either because the footprint extends beyond the array, or because some stations are missing or not working at the time of the event. This occurs frequently because the horizontal events have a large longitudinal extension, which is not negligible compared to the size of the array. Losing a part of the footprint as indicated in figure 4.2 (right) makes the evaluation of W and L difficult to recover.

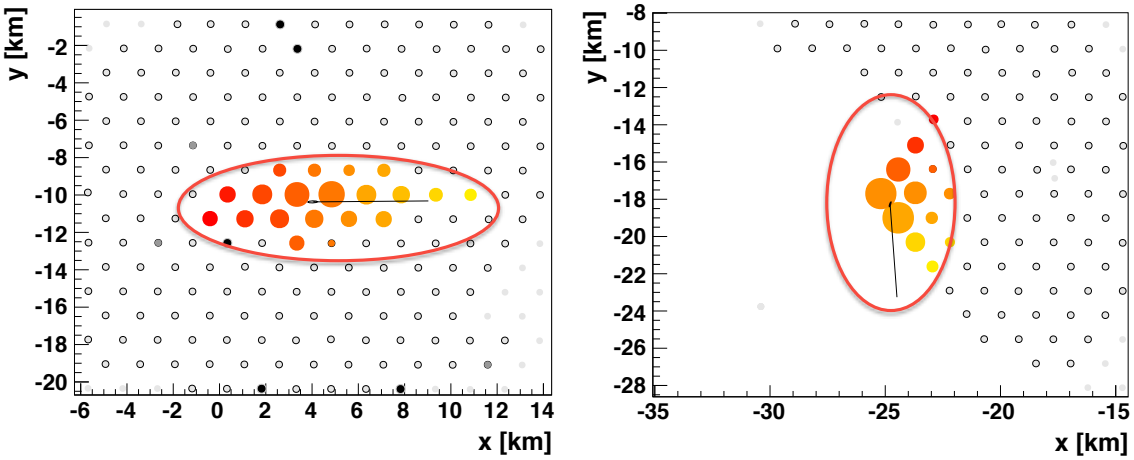

Figure 4.2 Footprints of inclined events detected in the SD. Left: extensive air shower footprint inside the array with 20 triggered stations. Right: extensive air shower footprint in the edge of the array with the shape compromised by the limitation of the latter. The black line in both panels marks the φ angle obtained from the arrival times of particles in the station.

Parameterization of the lateral distribution

To be less sensitive to an incomplete coverage of the hit stations, a second method is proposed. This method is based on a fit of a LDF of the station signals, mostly muonic component. Two parameters to describe both the spread of the muons and the magnetic distortion have been included in the function. Billoir, Deligny and Letessier-Selvon [160] showed that, for horizontal air showers, the dependence of the station signal on the distance to the axis is well approximated by an empirical exponential function of $\sqrt{r}$. Besides, the angular distribution is essentially modified by a quadrupolar term, with a main axis perpendicular to $B_\perp$. The following parameterization in a station of coordinates (r, ζ) in the shower frame is proposed:

$$S(r,\zeta) = S_{1000}\, e^{-\lambda\left(\sqrt{\frac{r}{1000}}-1\right)} \left(1 + \alpha \cos\left(2(\zeta - \zeta_B)\right)\right) \tag{4.4}$$

where ζ_B represents the direction of the magnetic field. The direction is properly determined by the geometrical fit of a front on the start times, so the parameters in the LDF fit are the core position (X_c, Y_c), the average signal at 1000 m (S_{1000}), the lateral extension parameter (λ) and the angular distortion parameter (α). λ and α are the key of this analysis. They represent the change in the size of the footprint (λ) and the change in its form (α). Note that, with the definition in equation 4.4, these parameters are lower for higher deviations of the particles. The selected events must have then at least 5 stations to allow these parameters to be fitted; in practice, at least 6 stations are requested.

4.3 Simulation details and data set

Tools for a fast simulation

For this study there is no need to follow the development of the showers down to low energies. Only muons and their by-products can reach the ground. Besides, photons and electrons of energy below 500 MeV have practically no chance to produce an interaction generating a muon. Moreover, the electromagnetic by-products (decay or radiative interactions) follow closely the direction of the generating muons and have a relatively short range. The contribution of the electromagnetic by-products to the signal does not modify significantly the lateral distribution of the muonic signal. In this study only the trajectory of the muons is followed, assuming that the electromagnetic halo results just in a constant multiplicative factor in the average signal (between 1.15 and 1.20 according to simulations). The code of the air shower simulator AIRES has been modified to extract the muons at their production point, where the magnetic effect on the shower is still negligible.

This sample of muons is then propagated to the ground, taking into account the magnetic deviation, energy loss, multiple scattering and decay in flight. Instead of simulating the traces in the WCD, a different procedure is followed: muons hitting the station are sampled, and the resulting signal is obtained by summing FADC traces extracted from a library generated from a simulation of single muons injected in the detector in various directions.

Simulation set

Different sets of proton and iron showers with different energies (6 EeV, 10 EeV, 30 EeV) have been simulated at different arrival zenithal angles (70°, 74°, 80°). The azimuthal arrival direction, without importance in other analyses, is fundamental in this study, as the intensity of the magnetic field seen by the particles in the shower depends on it. Showers with $\varphi = 10°, 30°, ..., 350°$ have been simulated, and a detailed range between 170° and 190° has been covered with showers at every 1°. The analysis is focused in this region, because it is one of the two regions where the influence of the magnetic field is larger (see right panel of figure 4.1). The hadronic interaction models used are QGSJet01 and Sybill 2.1. Each shower has been injected 10 times at random positions, to smooth the influence of the array.

Data set

The data set is composed by the inclined events ($\theta > 63°$) collected at the Pierre Auger Observatory between January 1st, 2007 and August 31st, 2013. The number of collected events (N_{data}) is 116065. However, for this study only fixed values of the three observables (E,θ,φ) have been used, with the corresponding selection cut for each one. The necessity to meet 3 selection cuts implies that the final number of available events for the study after the cuts be very reduced. Nevertheless, the selection criteria were flexible enough to guarantee the maximum number of events without polluting the data sets.

As the reconstruction of the energy implies more incertitude, the energy is not reconstructed in the data set. Instead, to compare the data against the simulations, a match in S_{1000} (see section 1.4) is requested, as S_{1000} is an estimator for the energy. For every fixed energy in the

simulation set, a range in S_{1000} is defined as $\overline{S_{1000}} \pm 1.5 \times \sigma(S_{1000})$. The selection ranges and their respective number of events are described in table 4.1 and represented in figure 4.3.

Table 4.1 Intervals of S_{1000} [log(VEM)] for different energies ($E_{\rm sim}$) [EeV]. Based on the mean and the rms of the distributions in figure 4.3.

$E_{\rm sim}$	$\overline{S_{1000}}$	$\sigma(S_{1000})$	S_{1000}^{min}	S_{1000}^{max}	N_{data}
6	2.58	0.21	2.26	2.89	6816
10	2.92	0.22	2.59	3.25	3892
30	4.07	0.16	3.83	4.31	336

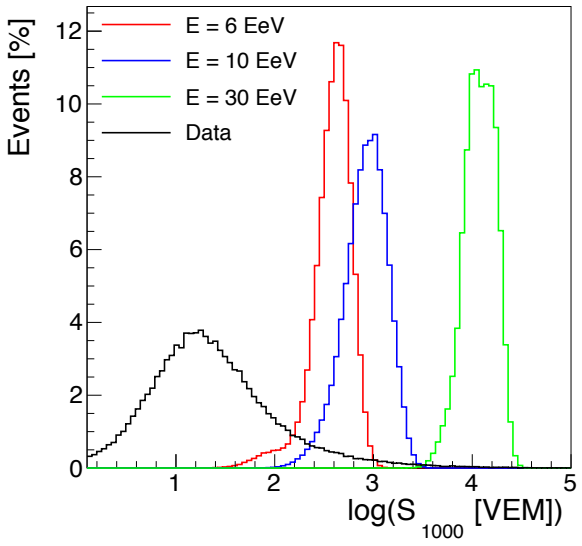

Figure 4.3 Distributions of the S_{1000} for simulated events with different energies (6, 10 and 30 EeV) and for the whole data set. Intervals of S_{1000} (see table 4.1) for different energies are derived from these distributions.

The number of events decreases with θ. The selection has been carried out in ranges of $\pm 2^\circ$ around the simulated θ. The number of events available (N_{data}) for the lowest (70°), intermediate (74°) and highest (80°) zenith angles are 27549, 24820 and 14239, respectively.

A flat distribution is found in the φ angle of the data set. For the analysis in φ, the whole range (0°,360°) has been divided in 12 bins. For other analyses, the selection criterion for the azimuthal arrival direction is based on the magnetic field, selecting the directions for which $B_\perp$ is higher than 0.9.

4.4 Characterization of the deflections for α and λ

The angular distortion parameter α (see equation 4.4) plays a role similar to W/L, as both measure the angular distortion of the shower produced by the effect of the magnetic field. The study of the characterization of the deflection is focused, then, only on parameters α and λ.

To characterize them, different dependencies are studied: the modulation over φ, the influence of the energy and θ, and the possible dependence on a non-perfect array.

Dependence on the arrival azimuthal angle (φ)

From figure 4.1 (right) a dependence of the deflection parameters on the arrival azimuthal angle is expected. This dependence is expected as a modulation and it is interpreted as originated exclusively by the change in the intensity of the magnetic field seen by the particles in the shower for different arrival azimuthal angles. This effect of a φ modulation is shown in figure 4.4 for simulated proton and iron nuclei primaries using the QGSJet01 hadronic interaction model. The simulated energy is 10 EeV and the arrival zenithal angle is 74°. The parameters reconstructed for the Auger data are also shown. Data are selected within the ranges detailed in the previous section (cuts for energy and θ). A quality cut excluding events with relative uncertainty on λ and α larger than 40% is also applied. In the end, a few hundreds of events are available in the whole range of φ, leaving a few tens of events in each bin.

Both α and λ parameters are shown in figure 4.4. It is important to remember that lower values of α and λ indicate a stronger deflection. The angular distortion parameter α (figure 4.4, left) shows a clear modulation in the simulation for both primaries, with small differences between the primaries in the arrival azimuthal angle regions where the deflection is higher. The data are, in the majority of the bins, in agreement with the modulation shown in the simulation, if the error bars are taken into account. This error bars represent the dispersion of the value divided by the square root of the number of events in the bin, because the aim is a statistical analysis. The lateral extension parameter λ (figure 4.4, right) shows the same clear modulation in the simulation for both primaries, but the difference between them is not appreciable except for the φ regions where the deflection is lower. Regarding the data, a general shift can be observed when comparing the selected events with the simulated ones. The lateral extension observed in the data is broader (lower value of the parameter) than the lateral extension predicted by the simulation, and this shift for the case of $E = 10$ EeV and $\theta = 74°$ will be also seen in next analyses in the next subsections. It will also be seen that this shift is not found in all the energies or arrival zenithal angless. The expected modulation is not clearly observed in the data.

As the sensitivity to φ consists in a modulation, and different values of φ return the same deflection, the dependence on this angle, for the following analyses, is considered as the dependence on the perpendicular magnetic field, real source of the studied feature. Thanks to this consideration, it is possible to include in the analyses different ranges of φ corresponding to the same deflection, increasing the statistical power. Besides, for the following analyses, the attention is focused only on the region where the deflection is higher. This region is around both $\varphi = 180°$ and around $\varphi = 0°$, and the selection is carried out by requesting for a $B_\perp$ higher than 90% of the maximum.

Dependence on the arrival zenithal angle (θ)

The dependence of the deflection parameters on the arrival zenithal angle is expected in two senses. First, the perpendicular magnetic field, for a fixed φ, variates according to θ. This

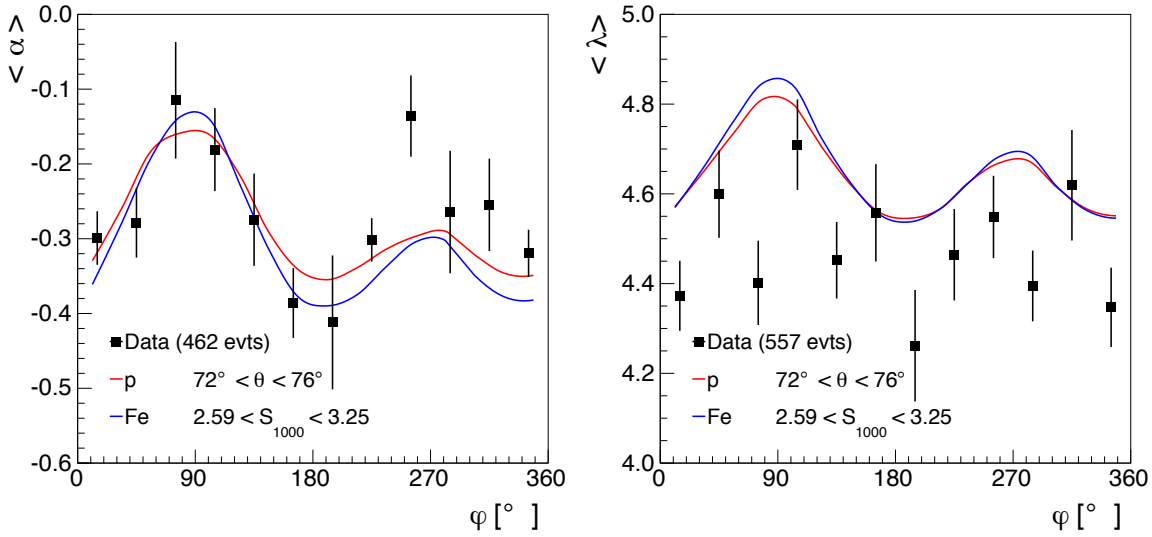

Figure 4.4 Angular distortion parameter α (left) and lateral extension parameter λ (right) for different values of the arrival azimuthal angle, for extensive air showers induced by proton (red curve) and iron nuclei (blue curve) primaries with 10 EeV energy and zenith angle 74° (simulations performed with QGSJet01). A range in energy and θ is chosen (see text) to select the events in the data (black squares). A quality cut in the uncertainty of the parameter is introduced excluding those events with a relative uncertainty larger than 40%. The error bars represent the dispersion of the value divided by the square root of the number of events in the bin.

variation with θ also changes for the different selected φ. For some φ, $B_\perp$ increases with θ, for other it decreases, and for some regions, as the region selected for this study ($B_\perp > 0.9|B|$), it is stable (see figure 4.1, right). Second, and even more important, air showers with higher arrival zenithal angles traverse a longer path through the atmosphere, increasing the exposure to the deflection.

The histograms for the three values of θ ($\theta = 70°, 74°, 80°$) are shown in figure 4.5, where the simulations are compared to data. In the three cases, proton showers have been simulated with QGSJet01, at 10 EeV of energy and $B_\perp > 0.9|B|$. The scarcity of the available events is evident for the largest θ.

A strong dependence of the deflection on θ is clearly appreciated in both parameters, where higher values of θ correspond to lower values of α and λ, and consequently, to higher deflection. The dispersion of the parameter α is clearly smaller for the largest θ, when considering the simulations. This improvement in the resolution with θ is very slightly appreciated for the other two angles, and it is not appreciated in the data, so a general conclusion is difficult to achieve. The data return the values predicted by the simulations for both parameters, with the exceptions of the cases of λ at 74°, where the deflection shown in the data is higher than the prediction, and α at 80°, with a deflection lower than the predicted one. This was also observed in the previous figure. However, this needs to be interpreted carefully, as the statistics available are small.

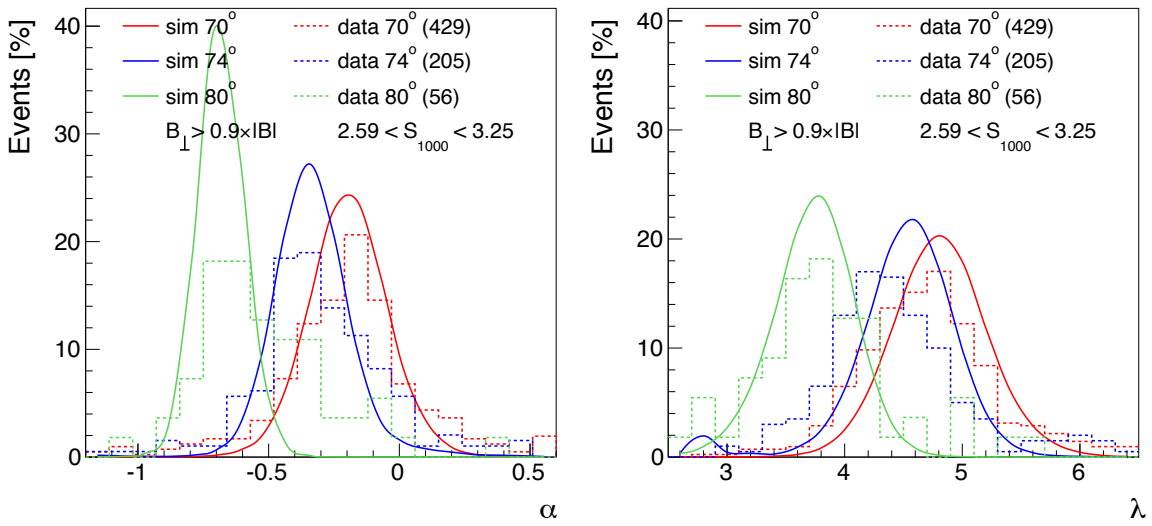

Figure 4.5 Angular distortion parameter α (left) and lateral extension parameter λ (right). Histograms for different zenith angles and same energy (10 EeV) and $B_\perp > 0.9|B|$ for protons generated with QGSJet01 and for the Auger data. The sizes of the distributions are normalized to facilitate the comparison, but the decreasing of the available events with higher θ is clear: the numbers between parenthesis indicate the statistics.

As the changes in the parameters with θ are affected not only by the changes in perpendicular magnetic field, but also by the changes in the traversed atmospheric path, the selection in θ can not be carried out by the selection in $B_\perp$, like it is done for the φ dependence, so the selection is carried out in θ. A selection carried out in $B_\perp$ instead of θ would allow to reduce the number of cuts, as both θ and ϕ would be selected at once.

Dependence on the energy

To study the dependence of the deflection parameters on the energy, three values of energy have been selected (6, 10 and 30 EeV). The primaries are protons simulated with QGSJet01. The mean θ is 74° with the cited width of ±2°. The condition on $B_\perp > 0.9|B|$ is also requested.

The distributions of the corresponding parameters are shown in figure 4.6 for data and simulations. The mean of the angular distortion parameter α (left) remains unaffected if the energy of the primary is changed, but the dispersion is reduced for higher energies. This prediction by the simulation is confirmed in the data. On the contrary, the lateral extension parameter λ (right) reveals a small dependence on the energy of the primary particle. This dependence with the energy may be related to the fact that the range in r for triggered stations increases with energy, so a small deviation from the LDF shape results in a r-dependent effective slope of the exponential, hence a bias on the fitted value λ. When comparing data to simulations with the same lateral extension, this bias is not a real problem. It may also be sensitive to the handling of non-triggered stations in the fit; these technical problems are beyond the scope of this analysis. At the same time, with higher energies the resolution

improves, due to the availability of more stations in the fit. A relatively good agreement between the data and the simulation is also found, except for the bias in λ.

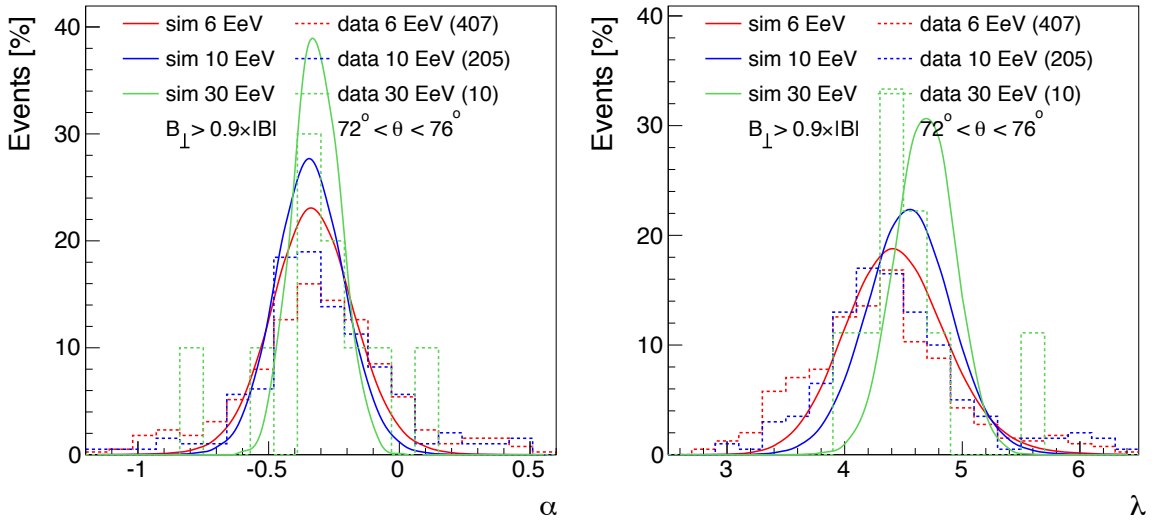

Figure 4.6 Angular distortion parameter α (left) and lateral extension parameter λ (right). Normalized histograms for different energies and same zenith angle (74°) and $B_\perp > 0.9|B|$. The data are normalized and the lack of large statistics is clear for higher energies, as it is for larger θ. The number of events is shown between parenthesis. The simulated primaries are protons generated with QGSJet01.

Dependence on a limited surface detector array

The shower shape expressed with W and L was discarded for the clear dependence on a limited array. Horizontal events are long spots hitting a large number of stations and the chance to hit a border station is larger than in vertical showers. Moreover, the possibility of having one or several stations non functioning in the event, is not negligible. The proposed parameterization (equation 4.4), a priori, does not depend on the array. However, the possible bias on the fitted values of the parameters α and λ with the array imperfections needs to be investigated.

A study has been conducted to account for the imperfections of the array in two senses. First, forcing the spot of the shower to be at the border: a line is drawn with a random position (from 0 to 1000 m from the core) and random orientation (from 0° to 360°) inside the spot. The stations above the line are discarded. And second, removing 20% of the stations randomly from the list, even if the expected missing station rate in Auger is not that high. Finally, after the two introduced imperfections, four configurations of simulations are carried out: perfect array; array with borders; array with holes; array with borders and holes. The same conditions established for previous analyses have been requested: E = 10 EeV, $\theta = 74°$ and $B_\perp > 0.9|B|$, with the corresponding ranges for the data. In figure 4.7 it is shown how the parameters α and λ are stable against the imperfections of the array, but their distributions are broadening. The mean of the different cases remains mostly identical, even if the number of fitted stations

changes in all the cases.

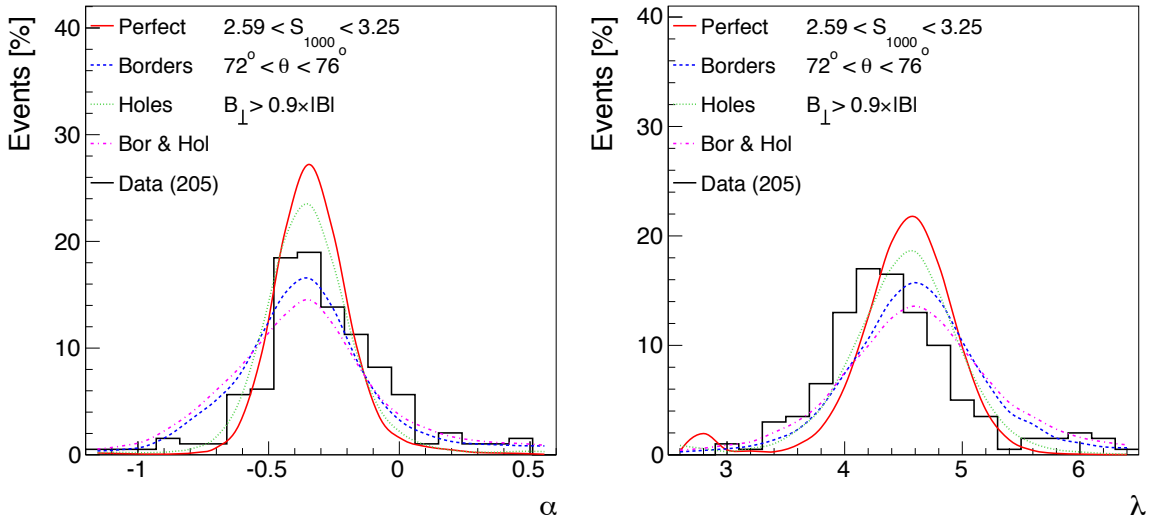

Figure 4.7 Parameters α (left) and λ (right) for different array assumptions. Perfect array (solid red line), events at the border (dashed blue line), events with missing stations (dotted green line) and events at the border and with missing stations (dotted and dashed pink line). The Auger data are also shown (solid black line). QGSJet01 simulated proton at E = 10 EeV, $\theta = 74^\circ$ and $B_\perp > 0.9|B|$.

4.5 Dependence on the muon production profile

A relation between the angular distortion α and the muon path is expected, allowing the access to $X^\mu_{\max}$ through an observable measured with SD. However, as exposed above, this distortion also depends on the arrival direction (θ,φ), whereas it has been found to be independent of the energy of the primary particle. If θ and φ are precisely measured using the arrival times of the particles at the detector, the sensitivity on $X^\mu_{\max}$ for the angular distortion can be exploited. In this analysis, the value of $X^\mu_{\max}$ for the simulation set is taken directly from the MC simulation. Using this analysis, an estimator for $X^\mu_{\max}$ will be constructed, and it will be applied to both simulation and data.

Even if the independence of α on the energy is shown in figure 4.6, the study of the possible dependence of α on the muon profile is carried out for different energies (by the mentioned selection in S_{1000}), evaluating the energy with the LDF analysis. In the left panel of figure 4.8, the distortion for events with different $X^\mu_{\max}$ is shown, for protons, irons and a mix simulated with QGSJet01 at 10 EeV. The arrival zenithal angle is 74° and the condition of a perpendicular magnetic field higher than the 90% of the maximum is also requested. The correlation between the distortion and the observable $X^\mu_{\max}$ is clear. The difference (for the same $X^\mu_{\max}$) between proton and iron is small enough to observe this correlation with any other proportion chosen in the mix. However, as the error bars in α (for data) are larger (for single events) than the

difference between proton an iron (see figure 4.4), an event-by-event analysis is not possible. But a statistical analysis of the average values of α, and consequently, $X^{\mu}_{\rm max}$, is still possible.

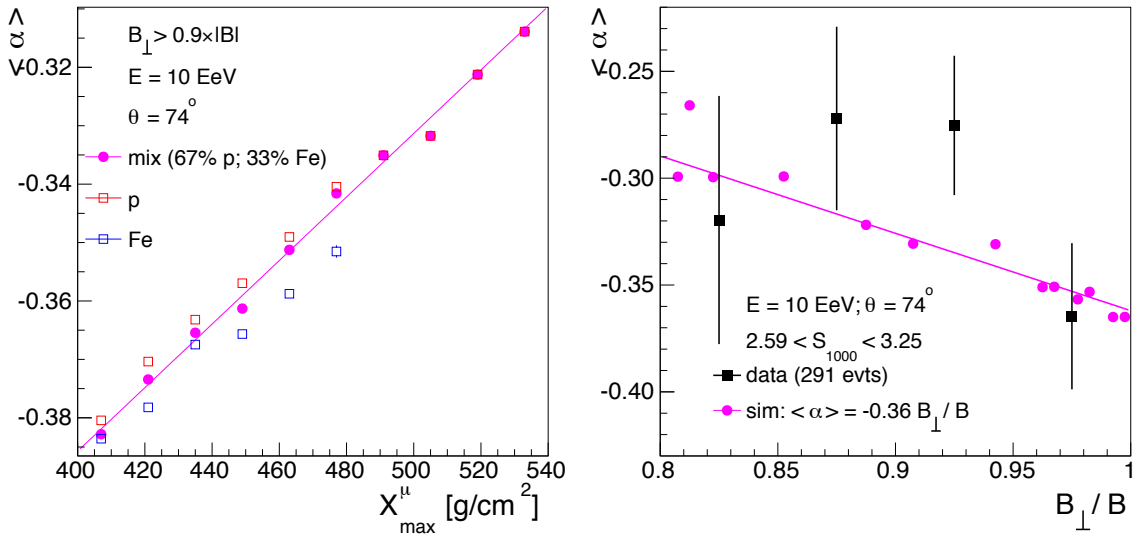

Figure 4.8 Left: correlation between the angular distortion α and $X^{\mu}_{\rm max}$ for showers at E = 10 EeV, $\theta = 74°$ and $B_{\perp} > 0.9|B|$, simulated with QGSJet01. Protons (empty red squares), iron (empty blue squares) and a mix of the two (solid pink circles; 2/3 protons 1/3 irons). The line is the fit of the points of the mix. Note that both primaries are not equally distributed along $X^{\mu}_{\rm max}$, and for the simulation set for irons, the maximum $X^{\mu}_{\rm max}$ is about 480 g/cm^2, so above this value (last four bins) the mix represents only protons. Right: parameter α for different intensities of the magnetic field for a fixed energy and θ. A mix (2/3 protons 1/3 irons) simulated with QGSJet01 at E = 10 EeV and $\theta = 74°$. The points are fitted to a line, fixing the second parameter (y-intercept) to zero. The slope resulting from the fit is indicated in the legend. The data for the indicated energy and θ are also represented.

For given values of E, θ, $B_{\perp}$, the variation over the mean α ($\Delta\alpha = \alpha - \bar{\alpha}$) is expected to depend on $X^{\mu}_{\rm max}$. Besides, as the relation between α and $X^{\mu}_{\rm max}$ has been found to be linear, the relation between this deviation from the mean ($\Delta\alpha$) and $X^{\mu}_{\rm max}$ is also expected to be linear. By fixing (E,θ) to certain values, it is possible to study the evolution of the mean of α over all possible $B_{\perp}$. This is represented in the right panel of figure 4.8, focusing the attention in the region with more deflection. The points are fitted to a line ($\bar{\alpha} = a_1\, B_{\perp}$) with the y-intercept equal to zero. The absence of a second parameter is due to the fact that α should be equal to zero in absence of magnetic field. This fitted line, and the calculated parameter a_1, allow the calculation of a mean expected distortion ($\bar{\alpha}$), dependent on $B_{\perp}$, for every combination of values of (E,θ). Finally, the difference between the measured value of α and the calculated mean ($\Delta\alpha = \alpha - \bar{\alpha}$) is expected to be correlated with $X^{\mu}_{\rm max}$ (see left panel of figure 4.9).

This relation can be parameterized. The values of $\Delta\alpha$ versus $X^{\mu}_{\rm max}$ are in figure 4.9 (left) for the case of E = 10 EeV and $\theta = 74°$. These points are fitted to a line ($\Delta\alpha = a_2 \times X^{\mu}_{\rm max} + b_2$). The parameters obtained (in addition to a_1 already known) allow the construction of an

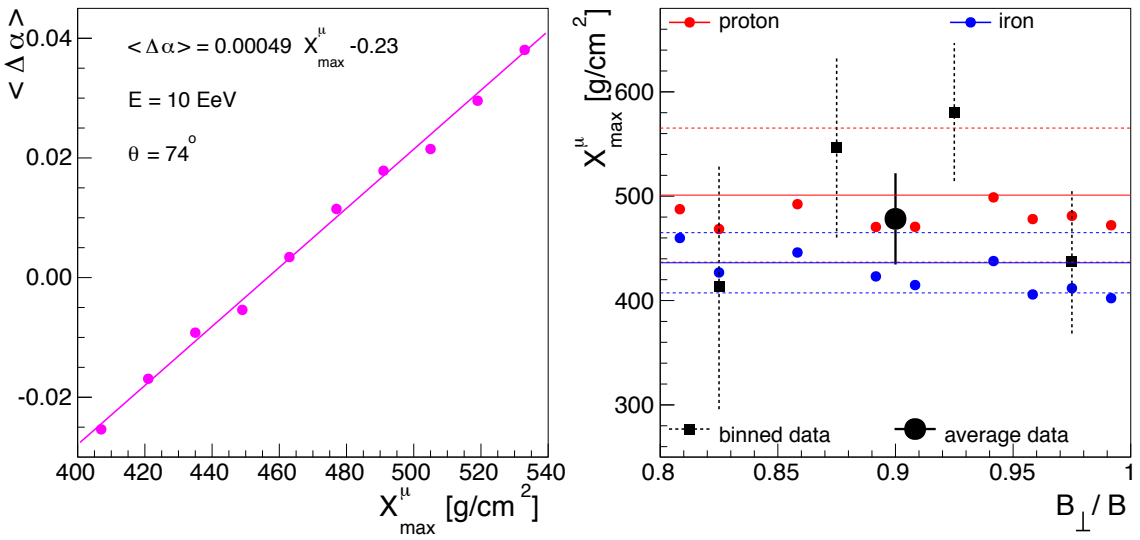

Figure 4.9 Left: correlation between the proposed parameter $\Delta\alpha$ against $X^{\mu}_{\max}$. The shape is fitted to a line, with the parameters indicated in the legend, for a mix of 2/3 protons and 1/3 irons. Right: estimated $X^{\mu}_{\max}$ (with estimator in equation 4.5) for different values of the $B_{\perp}$. Estimated value for proton (red circles), iron (blue circles), and data (small black squares). An average value for the data is also shown (big black circles). The horizontal lines indicate the simulated $X^{\mu}_{\max}$ for proton (red) and iron (blue), where the solid lines indicate the mean and the dashed lines indicate the $mean \pm rms$. Simulated with QGSJet01 for E = 10 EeV, $\theta = 74^{\circ}$.

estimator for $X^{\mu}_{\max}$, based on α and $B_{\perp}$, with the following shape:

$$X^{\mu}_{\max} \;=\; a\;\alpha \;+\; b\;B_{\perp} \;+\; c \tag{4.5}$$

where the parameters a, b and c are specific for every combination of E,θ.

$$a = \frac{1}{a_2}\;;\; b = -\frac{a_1}{a_2}\;;\; c = -\frac{b_2}{a_2} \tag{4.6}$$

The application of this estimator to the Auger events with E = 10 EeV and $\theta = 74^{\circ}$ is shown in the right panel of figure 4.9, with the parameters obtained as explained above. The estimation of $X^{\mu}_{\max}$ carried out with the distortion of the simulations is in the range expected for both primaries. Regarding the estimated $X^{\mu}_{\max}$ for the Auger data, the mean is in the middle of the proton distribution, and a bit too deep with respect to the iron case, but inside the distribution if the error bar is considered.

4.6 Dependence on the transverse momentum

If α measures the angular distortion, λ measures the lateral extension. It is expected that this parameter bring to the ground information about the development of the shower. To study the possible influence of hadronic processes in the lateral extension parameter, different tests have been performed.

With the same initial conditions for the primary particle (protons with E = 10 EeV, $\theta = 74°$ and $B_\perp > 0.9|B|$), some changes in the development assumptions have been simulated. First, two different models, Sybill 2.1 and QGSJet01, were used to simulate the showers. And second, two different transverse momentum (P_T) were assigned: the nominal one, or a factor 1.1 on the P_T of all muons (without changing the energy).

In figure 4.10, the deflection parameters for the four combinations of the model and the P_T factor are shown. The Auger data are also shown. Even if a priori only λ was expected to show an appreciable change, the means of the distributions for the different combinations change either for α (left) as for λ (right). This proves the dependence on the models of the analysed parameter. In QGSJet01 larger values of λ and smaller values of α are found than in Sybill 2.1, while different P_T provokes a change in both models.

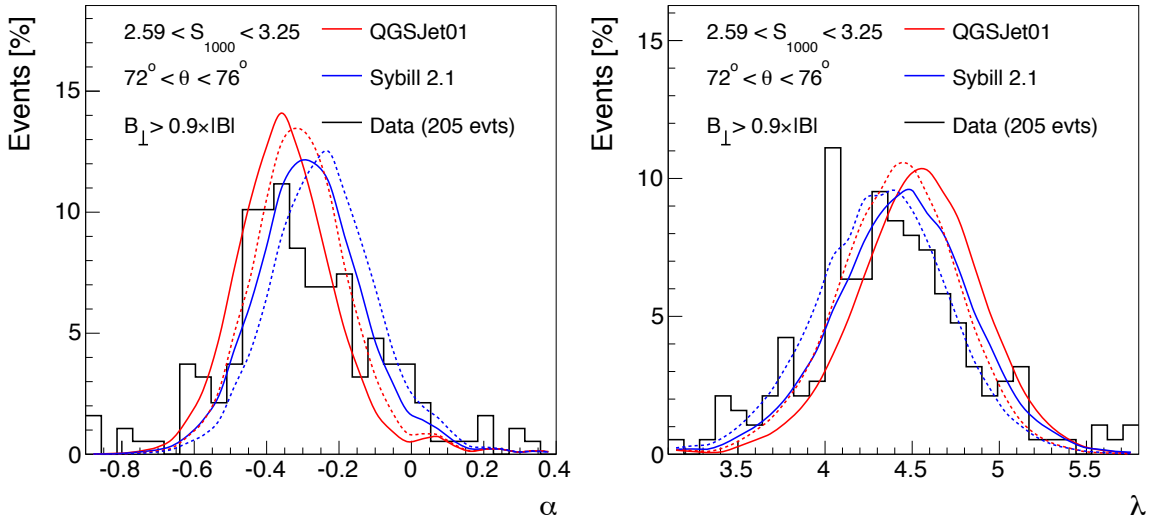

Figure 4.10 Distributions of the parameter α (left) and parameter λ (right) for different models (red and blue lines). Dashed lines indicate a 10% incremented P_T factor. Simulations have been done for protons at E = 10 EeV, $\theta = 74°$ and $B_\perp > 0.9|B|$. Auger data are also shown (black histogram).

To quantify this change, in a first approximation, it is possible to use the Kolmogorov-Smirnov (KS) test [161]. This test is based on the maximum distance of the empirical cumulative distribution function (ECDF) of the two compared distributions. This test takes into account in the comparison the mean, the rms and the type of distribution. Several comparisons are of interest: between the two models, between the two different P_T, and how

similar all the simulated distributions are to the data. In table 4.2 the different values for the maximum KS distance (D_{KS}) are shown. For completeness, the means and the rms are also shown (see table 4.3).

Table 4.2 Maximum KS distance between distributions of α and λ from different assumptions in the development of the shower, two hadronic interaction models and different P_{T}. The results of the KS tests are shown also after comparing the four simulated distributions with that given by the data.

Case	Comparison	$D_{KS}(\alpha)$	$D_{KS}(\lambda)$
1	QGSJet01 Vs Sybill 2.1	0.20	0.10
2	QGSJet01 Vs QGSJet01 high P_{T}	0.14	0.14
3	Sybill 2.1 Vs Sybill 2.1 high P_{T}	0.11	0.12
4	Data Vs QGSJet01	0.15	0.20
5	Data Vs Sybill 2.1	0.13	0.10
6	Data Vs QGSJet01 high P_{T}	0.10	0.11
7	Data Vs Sybill 2.1 high P_{T}	0.22	0.06

Table 4.3 Mean and rms for α and λ for different assumptions in the models.

	α		λ	
	mean	rms	mean	rms
QGSJet01	-0.34	0.15	4.53	0.36
Sybill 2.1	-0.28	0.15	4.44	0.39
QGSJet01 high P_{T}	-0.30	0.14	4.42	0.35
Sybill 2.1 high P_{T}	-0.24	0.15	4.33	0.38
Data	-0.30	0.22	4.37	0.47

By analysing the angular distortion, the distributions due to different hadronic interaction models have a D_{KS} between them of 0.20 (see case 1 in table 4.2), deflections being higher for QGSJet01. A higher P_{T} slightly decreases the deflection (cases 2 and 3). This effect is observed in both hadronic interaction models. Furthermore, out of the 4 combinations, the data distributions are more similar to that based on QGSJet01 with increased P_{T} (0.10, case 6). Sybill 2.1 with increased P_{T} shows a D_{KS} of 0.22 (case 7) far from the data, whereas the other two combinations yield in intermediate values of D_{KS}.

By analysing the lateral extension, the difference between the models is found lower than in the α case. Muons in the simulations performed with QGSJet01 suffer a lower deflection quantified in a D_{KS} of 0.10 (case 1 in table 4.2) when comparing with those simulated with Sybill 2.1. In both hadronic interaction models, a higher deflection is observed when P_{T} is increased (cases 2 and 3). The data are more likely to be represented by the Sybill 2.1 model with increased P_{T} (case 7), according to D_{KS}, whereas QGSJet01 (case 4) is the one with a larger distance between the distributions.

All these quantifications have to be considered very carefully, as the uncertainties in the presented method are large. However, the influence of the changes in the model assumptions in both deflection parameters is proven. The sense of this influence (either increasing or decreasing the deflection) is also characterized.

4.7 Conclusions

The shape of the shower spot at ground, measured by two different parameters (α and λ) has been proven to be dependent on different extensive air shower observables. The angular distortion parameter α is dependent on the azimuth angle φ and the zenith angle θ, but not on the energy (see figures 4.4, 4.5 and 4.6, left). In contrast, the lateral extension λ is dependent on the azimuth angle φ, the zenith angle θ, and also on the energy (see figures 4.4, 4.5 and 4.6, right).

However, the dependence of these parameters on more interesting shower properties is more relevant. The parameter α is correlated with $X^{\mu}_{\max}$, an observable used for composition analyses (see figure 4.8, left), that has been proven difficult to extract. Using this dependence, an estimator of $X^{\mu}_{\max}$ for a statistical analysis has been constructed (see equation 4.5), providing an alternative approach to composition analyses (see figure 4.9, right). This approach is complementary to other MPD approaches (see section 3.2 or [144]). The zenith angle used for this analysis (74°) is larger than those used in the other approaches ($55° < \theta < 65°$), having access to a different set of data. The larger zenith angle also implies that the muons arriving to the ground are those with higher energies, accessing to earlier stages of the development of the hadronic cascade.

Furthermore, α and λ are sensitive to the simulation model and to other different assumptions taken in the cascade process, like the P_{T} distribution of the muons. The study of these dependences could lead to an improvement of the knowledge about the cascade development (see figure 4.10).

The deflections observed are stronger for larger zenith angles. However, for this inclination, the Auger events available are very reduced, and a compromise has to be found between the size of the data sample and the studied deflection. $\theta = 74°$ has been chosen as a valid middle point.

In general, data and simulations are in an acceptable agreement for the deflection parameters. The parameter λ is affected by the chosen model and by the P_{T} distribution, so the models have to be adjusted to find the best representation of real events. As a future perspective, different parameterizations of the signal (see equation 4.4) can be tried to improve the method.

Chapter 5

Radio detection

The second approach to improve the mass composition identification capabilities of Auger is the use of new detection techniques with access to the longitudinal development of the shower in a full duty cycle operation. The radio emission in extensive air showers is the physical effect to be explored in this chapter. Different emission processes are examined, particularly focusing on the Molecular Bremsstrahlung Radiation (MBR). The MBR represents the most promising emission to be used as a new technique in ultra-high energy cosmic rays detection.

The proper understanding of the radio emission processes in extensive air showers is a gigantic task. Several research groups are currently working on this subject from very different perspectives. The research lines followed by the Extensive Air Shower Identification using Electron Radiometer (EASIER) group and the author are described in this chapter, along with other experiences that can help the reader to contextualize the whole subject of radio detection in extensive air showers.

The different emissions at radio frequencies and their characteristics are described in section 5.1. The initiatives of the Pierre Auger Collaboration on this topic are summarized in section 5.2. The section 5.3 briefly describes the instrumentation to equip a WCD with an antenna for radio detection. The different efforts done are detailed in sections 5.4, 5.5 and 5.6. Finally, the conclusions are presented in section 5.7.

5.1 Radio emission

The physical effect to be explored in this chapter is the radio emissions by secondary particles in the extensive air showers. The measurement of the radio signal is a calorimetric measurement of the electromagnetic profile, that contributes to the mass composition analysis in two senses. First, the maximum of the radio trace is directly related with the depth of shower maximum. And second, the muonic signal can be deduced by the subtraction of the estimated radio signal from the SD signal. These measurements would have similar characteristics to those of the FD, without the limitations in the duty cycle.

In the 1950s, the detection of Cherenkov emissions in the optical frequencies in extensive air showers was discovered and found to be concentrated in the forward direction [17]. After this discovery, the question was opened about the possibility to detect this radiation also in the

microwave region of the spectrum [18]. A coherent Cherenkov emission at lower frequencies was pointed out by Askaryan [162] in 1962, as result of a negative charge excess arising from the accumulation of Compton scattered electrons and positron annihilation. The first radio pulses detected from extensive air showers were reported by Jelley and collaborators in 1965 [19, 163]. In this first detection, the frequency was 44 MHz, but frequencies from a few MHz to 3 GHz were explored in the next years. A geomagnetic effect as origin of the radio emission was pointed out by Askaryan and further developed by Kahn and Lerche [164]. Despite these successful detections, the development of the detection techniques based on radio signals produced by extensive air shower was left aside in favour of detections based on particle detectors and fluorescence observations.

More recently, the problems with the FD duty cycle and the little longitudinal profile information in extensive air showers provided by the particle detector arrays renewed the interest of the community in the radio detection, in particular along three research lines.

Geosynchrotron emission

The first research line was open after the successful experiences of CODALEMA [62], a radio array working in coincidence with scintillators, and those of LOPES [63], also working in coincidence with the KArlsruhe Shower Core and Array DEtector (KASCADE) array. Both experiments explored the mentioned geosynchrotron emission proposed by Kahn and Lerche [164].

The geosynchrotron emission (white arrows in figure 5.1) is the dominant contribution to the radio emission in the atmosphere. It is caused by the acceleration of electrons and other charged particles in the geomagnetic field. The geomagnetic field contributes to separate the charged components in the shower. This electric dipole, and its transverse current, provide an additional emission mechanism. Particles of opposite charge emit a radiation in opposition of phase that cancels out. However, if the charges are spaced at a distance d, the phase difference is shifted by a factor of d/λ, where λ is the wavelength of observation. A wavelength greater than the physical dimensions of the emitting region would lead to a coherent emission. The longitudinal dispersion of the shower particles is considered as the thickness of the shower disk (< 3 m), so frequencies lower than 100 MHz are required to have a coherent emission. Besides, the constant deflection of the charged particles generates a transverse current, source of magnetic field. When this element of current is moving faster than the speed of light in the medium, a shock wave is produced and the radiation is amplified.

In this first research line, the radio detection is focused on the MHz range. The experiences of CODALEMA and LOPES have been more recently followed by AERA [165], measuring geosynchrotron emission at Auger. The efforts made by the EASIER group and the author about this topic are detailed in section 5.4.

Askaryan effect

The second research line was opened after the verification in accelerator experiments of the mentioned Askaryan effect, predicted in 1962 [166].

Askaryan suggested that the extensive air showers in dense media could not be electrically

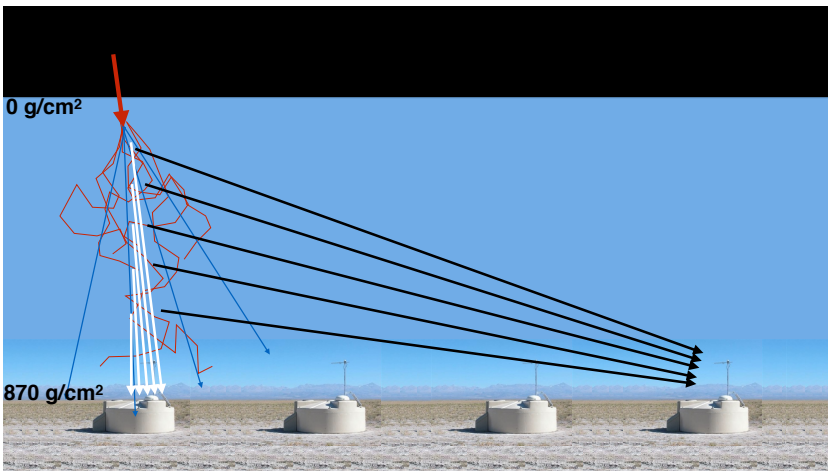

Figure 5.1 Sketch of the different kind of radio emissions in the extensive air shower. Geosynchrotron and Askaryan are beamed emissions (white arrows), whereas the MBR is an isotropic emission (black arrows). Note that for the MBR only the emissions that arrive to the antenna are represented, but they are emitted in all directions. The electromagnetic component of the shower (red scattered lines) and the muonic one (blue arrows) are also represented. The big red arrow represents the primary particle. The sketch is not scaled.

neutral, as Compton scattering could knock electrons from the material into the shower. Besides, positrons in the shower could annihilate in flight. The number of moving electrons in the shower can exceed the number of positrons by some ten percent. This excess should lead to a strong coherent radio and microwave Cherenkov emission (white arrows in figure 5.1) for showers that propagate within a dielectric.

Although the dominant source of radio emission is due to the geomagnetic separation of charges, rather than to the Askaryan effect, the fact that this effect is more intense in dense media (like ice) has triggered experiments at the South Pole like RICE [65], ANITA [66], ARIANNA [67] and ARA [68].

Molecular Bremsstrahlung Radiation (MBR)

The third research line was triggered by the observations of microwave continuum emission in the GHz band [1-10 GHz] from the free charges in the air shower, due to MBR, in the experiments at Argonne Wakefield Accelerator Facility (AWA) and SLAC National Accelerator Laboratory (SLAC) [82].

The ionization process is the main mechanism of the atmosphere to absorb the energy of the extensive air shower, resulting in numerous low energy electrons. The MBR is a continuous Bremsstrahlung emission (black arrows in figure 5.1) produced in weakly ionized air, and created by these free secondary electrons through quasi-elastic scattering in the fields of neutral molecules of the atmosphere, mainly with nitrogen, and to a lesser extent, oxygen [167]. This emission in the GHz range is expected to be isotropic and unpolarized, allowing extensive air showers to be detected, in theory, far from the shower core. MBR emission can be compared,

in terms of experimental measures, with fluorescence emission. The MBR emission intensity is expected to be proportional to the extensive air shower ionization rate, consequently to the total number of charged particles in the shower, and therefore to the shower energy. The intensity of this emission is still not very well established, although several efforts have been carried out by different research groups [82, 167–170].

In addition to the AWA and SLAC experiments, Air Microwave Yield (AMY) [169] and Microwave Air Yield Beam Experiment (MAYBE) [168] were also set up to confirm and characterize the MBR emission. Besides, AMBER, Cosmic Ray Observation via Microwave Emission (CROME), MIDAS and EASIER have been exploiting this detection option. The different efforts done by the author in the AMY experiment and, mostly, with the EASIER group, are detailed in sections 5.5 and 5.6.

Detection of radio signals

As a summary of the different physical effects described above and their characteristics, it is worthy to focus on how these different effects can be detected. The geosynchrotron emission is searched in the MHz range and the MBR in the GHz range, whereas the Askaryan effect is searched in a wide range between the two.

Both geosynchrotron and Askaryan emission are beamed, so the usage of these methods to detect extensive air showers is very limited around the shower core, discouraging their application to detect ultra-high energy cosmic rays. On the contrary, the MBR emission, being isotropic and unpolarized, would provide a relatively cheap detector analog to the FD with the added benefits of having nearly 100% duty cycle and being unaffected by atmospheric attenuation (less than 0.05 dB/km) or clouds. The consolidation of this detection technique would be a great step to determine the mass composition of cosmic rays.

The disadvantages of a beamed emission are two. First and most evident, the antenna need to be close to the core, reducing a lot the spacing between antennae, needing a large number of them to cover large surfaces like the one in Auger. Second, from a geometrical point of view, the antennae close to the core have a limited perspective of the profile of the shower (see white arrows in figure 5.1). The radio emissions produced all along the development of the shower arrive to the detector in a very short window of time, since their velocity is c/n, and from very similar directions. Actually, they arrive after the shower, as the particles of the shower travel at ultra-relativistic speed. This disadvantage does not completely prevent the reconstruction of the $X_{\max}$, but it makes it more difficult, needing several measures in a very small region, increasing even more the needed density of detectors. As a result, the number of antennae needed for the detection of ultra-high energy cosmic rays based on beamed radio emissions is too high, being unfeasible. On the contrary, antennae far from the shower detecting MBR emission (see black arrows in figure 5.1) have a better perspective that allow a more precise reconstruction of the $X_{\max}$ of the shower, and they can detect showers at, in principle, several kilometres.

The possibility of an extension of the emission due to geomagnetic effect (normally associated with the MHz range) to higher frequencies has been suggested by the analysis of simulations [171]. The detection of this effect in the GHz range is possible at short distance from the shower axis. MBR emission is expected to be isotropic and unpolarized, while the possible

geomagnetic emission is beamed and polarized, as pointed above. These two parameters, the distance of detection and the polarization, are the key to understand the mechanism responsible for the detected emission.

5.2 Radio efforts at Auger

As described in section 1.4, four different R&D projects are being developed inside the Pierre Auger Collaboration, to improve the capabilities of the Observatory to measure the radio emissions of extensive air showers (see figure 5.2).

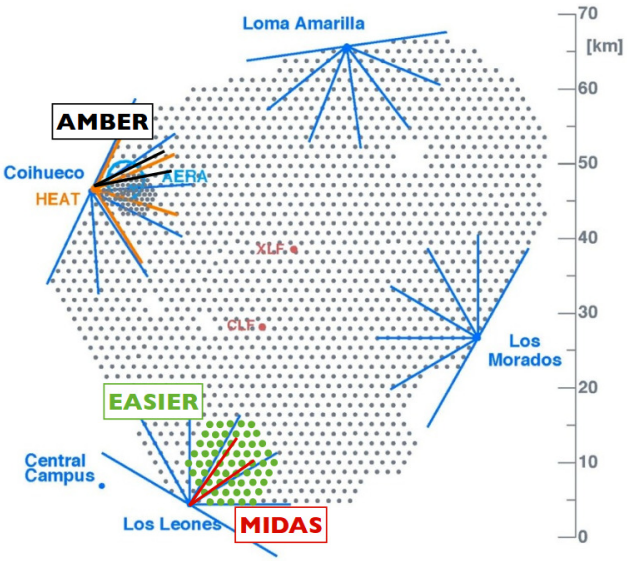

Figure 5.2 Map with the different experiments measuring radio emissions of extensive air showers at Auger.

The AERA final configuration consists in 160 antennae over a surface larger than 15 km^2. Up to now 124 have been installed. The radio detection is focused on the MHz range (from 30 to 80 MHz), benefiting from the geosynchrotron emission of the extensive air showers. The initial idea of AERA was to operate with an independent trigger based on the radio detection, but finally an external trigger based on the SD trigger will be implemented. The first important result of this R&D is the characterization of the radio emission in the explored range, where the emission is normally attributed to geomagnetic effect. The measurements done by AERA suggest the existence of another component that cannot be described by the geomagnetic emission process. This measured component is polarized radially with respect to the shower axis, in agreement with the Askaryan effect. This Askaryan component is established and represents a fraction of 14% of the measured emission [165].

AMBER and MIDAS focus their attention on the GHz range, and they search the detection of the MBR emission. These R&D projects are designed replicating the techniques of the

fluorescence detectors [172]. AMBER is a radio telescope of a 2.4 m diameter parabolic dish. In the focus of the dish parabole there are 16 antennae functioning as a camera. The twelve outer pixels are single-polarized C-band feed-horns, while the four inner ones are dual-polarized and dual-band (C-band and Ku-band). The field of view (FoV) is $14^\circ \times 14^\circ$ at 30° of elevation. AMBER operates with a SD dependent trigger. The AMBER prototype was tested at the University of Hawaii during 2010, and finally installed in the Auger site in 2011. MIDAS has a bigger parabolic dish (4.5 m) and a camera with 53 pixels. Each pixel is a C-band LNBF covering $\sim 1.3^\circ \times 1.3^\circ$ of the sky, for a total FoV of $20^\circ \times 10^\circ$, and it has an autonomous trigger. Initially installed at the University of Chicago, it was re-commissioned in September 2012 at the Auger site, where its performances are expected to improve in this radio quiet environment, and profiting from measurements in coincidence with the FD and SD.

The EASIER project is the fourth Auger R&D project. EASIER is an alternative approach, as it is designed with the purpose of detecting extensive air shower radio signals in a complementary way to the Auger SD. Two frequency regions are chosen as possible ranges to detect the radio emissions of the extensive air showers: the MHz range and the GHz range. The EASIER project was already started at the beginning of this thesis in 2012, and the results regarding the activities previous to this work are well described in the Ph.D. thesis of Romain Gaïor [69] and other publications [172, 173]. The last attempts to measure the radio emissions in extensive air showers with the EASIER project are described in the following sections. Brief details on the general state of the art regarding the MBR emissions are also included.

5.3 Instruments for the radio detection

The radio emission search in EASIER is developed in different frequency bands and with different devices and configurations, but the strategy for the implementation of the testing prototype is very similar in all the cases. In this section, the basic elements used in the installation of the antennae for the radio detection are briefly described.

In all the different EASIER configurations, the radio detection system is integrated in the WCD. The main reasons for the integration of the antenna in the WCD are the triggering of the radio detection (the WCD is the one that detects the presence of cosmic ray events), and the possible combination of the signals to have multicomponent information of the shower. But there are also technical reasons as powering the antenna or registering the signal, among others. The powering of the antenna is carried out with a power supply adapter. The consumption of the antenna and the added electronics is acceptable by the station power system. The data collected with the radio system are transmitted by one of the channels of the station. To minimize the impact, the radio signal uses the low gain channel, used only when the high gain channel is saturated. A study has been conducted to find out if the reconstruction parameters are affected with this modification. The study shows that the main reconstruction parameters remain mostly unaffected if one of the low gain channels is not available [174].

The different antennae (see figure 5.3) are installed, in all the cases, at the top of the station. In the first step after the antenna there is a low noise amplifier (LNA), as the amplitude at the output of the antenna is expected to be very low. This is followed by a filter. The signal is then integrated over the whole band and no offline filtering is possible. The selection of the frequency band is important to avoid the contributions coming from local emitters. It is also

Figure 5.3 Left: fat dipole antenna installed in the hexagon in 2011 for MHz measurements. Middle: feed horn *LNBF GI-301SC* antenna installed (7 in 2011 and 54 more in 2012) for the GHz measurements. Right: one of the butterfly antennae installed in 2013 for MHz measurements.

important to know with precision the working range when performing the signal integration. The radio frequency (RF) signal needs to be transformed from the frequency range in which it is detected to a shape that can be acquired by the Auger system. A logarithmic amplifier returns in the output a voltage proportional to the logarithm of the input power. After this logarithmic amplifier, an electronic board adjusts the signal to the final dynamic range of Auger through a linear transformation. The gain and the offset for this transformation have to be calibrated for each equipment at the laboratory previously to the installation in the field, and set up to a configuration that gives, at the end of the chain, a voltage between -2 and 0 V. Once the signal is transformed as described, it is integrated in the standard Auger chain of data acquisition.

Regarding the inclusion of the antennae in the actual array, the strategy followed in all the cases is to first install an hexagon test. If this experiment is successful, it is followed by a larger configuration. An hexagon is formed by seven detectors (6+1 in the center) in the standard array, with WCDs spaced 1500 m, covering $\sim 5.8\,\mathrm{km}^2$. This configuration allows for the detection of the event with different antennae and, potentially, the reconstruction of the event with the observables derived from the testing instrument.

5.4 Radio emission in the MHz band

In the MHz range, the first attempt was focused on the frequency range between 30 and 80 MHz, by filtering the signal with an electronic board. The receiver chosen was a fat dipole antenna (see figure 5.3, left) as the one tested and used in the CODALEMA experiment. An hexagon with seven of these antennae was installed in 2011 and the data collection lasted 8 months: 36 radio events were recorded in coincidence with extensive air showers detected by the SD. The energy of these events was from a few 10^{17} eV to more than 3×10^{19} eV. The

detection was proven to be possible and efficient, but the prototype had several deficiencies. First, the electronic connections were fragile. Second, the wind load of the antenna was too high in the Auger site for the position of the antenna. Third, the position of the antenna on the tank influenced the power pattern, making the efficiency of the detection anisotropic. The recorded signal was always very close to the shower axis in events with large zenith angle and the detection for vertical events at distances larger than 200 m was not achieved [69].

After the decommissioning of the seven fat dipole antennae, new efforts have been done to measure an extensive air shower emission in the MHz range, after the evaluation of the first test. The antenna design was changed to a butterfly antenna, following the evolution of CODALEMA (see figure 5.3, right), chosen to optimize the sensitivity between 30 and 80 MHz [175]. Other improvements were also included. First, the cable transporting the RF signal from the antenna to the electronic board was shielded to avoid its radiation and amplification, as it happened in the first installation. Second, a customized filter was ordered with a steep cut at 30 MHz and 60 MHz (see figure 5.4, right), as in the the first installation the band was found too large and several peaks were observed. A loss of 40 dB is reached at 3 MHz out of the selected frequency band. And third, the electronics was separated into two boards, to insure that no electronic noise from the power supply (in an independent box in the new configuration) can affect the data acquisition. The two boxes are connected with a cable equipped with ferrite to filter low frequency modulation from the power supply board to the EASIER board.

Calibration

During the fall of 2012 and the beginning of 2013, the calibration work of the EASIER electronic boards in the laboratories of the LPNHE was developed. The calibration was performed with sine waves simulating the detected radio emission. Eight boards were calibrated with two procedures. In the first procedure (figure 5.4, left panel), the output power, that it is tuned to be between -2 and 0 V, was measured in function of the power input (in dBm). A dBm is the power ratio in decibels (dB) of the measured power referenced to one milliwatt (mW). The linear relation between the input and the output in the studied range is clearly shown. Besides, it was observed that the output is identical for the different studied frequencies. In the second calibration procedure (figure 5.4, right panel), the output power was measured as a function of the frequency of the simulated sine wave. The chosen input power was -40 dBm. The sweep in frequency shows the effect of the filter reducing signals lower than 30 MHz and higher than 60 MHz. The mean of the output values inside the frequencies of the filter is in evident agreement with the output value measured in the first procedure. These two procedures allow the determination of the gain and offset described in section 5.3.

Installation and maintenance

In February 2013, five butterfly antennae were installed and in the next 6 months several events were registered. Several signal noises were observed in part of the traces. A dedicated work in the field was developed in November 2013 to understand the origin of the noises and to complete the installation of the initially proposed hexagon. Regarding the noises, their identification was found to be a very difficult task. Different kind of noises were found,

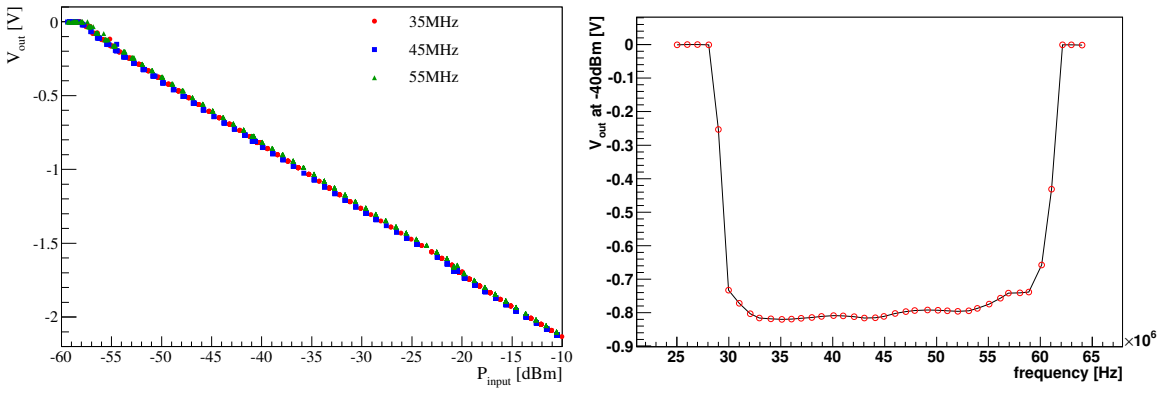

Figure 5.4 Example of one of the calibrated boards. Left: output voltage as a function of the input power for 3 frequencies: 35, 45 and 55 MHz. Right: voltage output as a function of the frequency for an input power of −40 dBm.

repetitive and at different locations (see figure 5.5). Several test were carried out at the station, far from the station, near the high voltage wires for the local usage and in an isolated room. The repetitive noises have a period shorter than the trace length, being found in every trace, so their identification and elimination is crucial. Not only the noises were difficult to identify, but other electronic problems appeared: several LNA boards were malfunctioning and the reparation on site was not possible. The static electricity generated by the wind in the tank of the WCD was identified as a possible source of the LNA problems, but this was not confirmed. As a summary, only two of the five installed antennae were able to properly register signals at the end of the mission, in November 2013.

Decommissioning

In March 2014 the MHz hexagon was decommissioned. The noise problems of the frequency band and the electronic failures discouraged the continuity of the project. These problems were added to the fact that AERA planned to also use the WCD trigger, so the differences between the MHz mission of EASIER and AERA become smaller. But the main reason was the constatation by the events registered, that the detection is not feasible far from the shower axis. The fact that the signal is beamed leads to focus the attention on the GHz band, where a detection of the isotropic MBR is expected.

5.5 Radio emission in the GHz band

The possibilities of using the radio detection to measure ultra-high energy cosmic rays are based on an isotropic emission that allows the detection of the extensive air shower from large distances. The expected isotropic emission in MBR process is the key of the concentration of efforts in the GHz band. Although some emissions have been detected in this band, their MBR origin is not well proven.

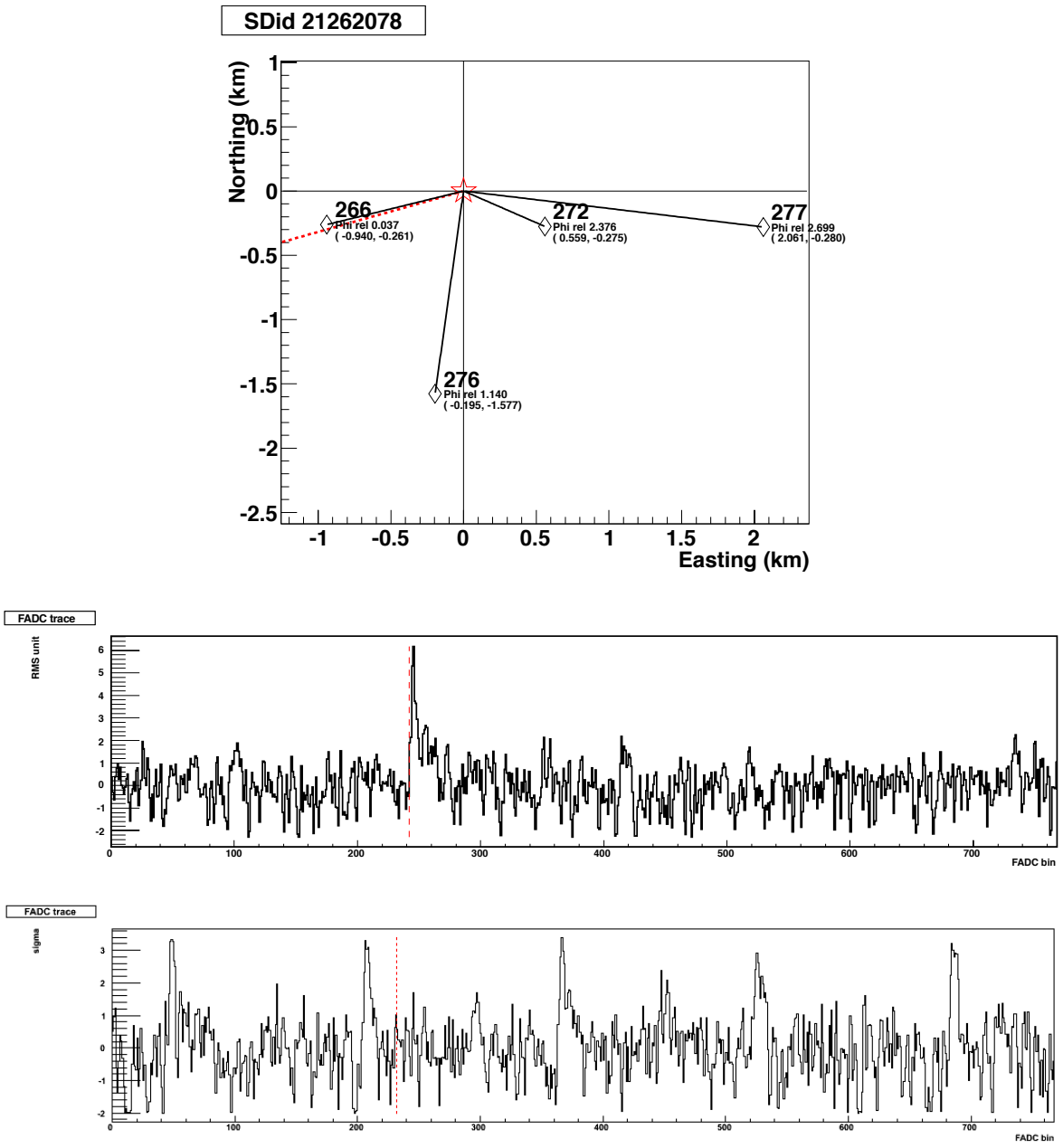

Figure 5.5 Above: map of an event with $\theta = 74.3°$, $\varphi = 196.6°$ and $E = 6.21 \times 10^{18}$ eV measured with the MHz antennae. Centre: raw FADC trace of the event above in the station with ID 266, close to the shower axis. Below: raw FADC trace (from a different event) with a repetitive noise every 4 µs. Each FADC bin corresponds to 25 ns.

In the publication by Gorham et al. [82], which motivated the opening of the MBR detection search, the received intensity reported was $F_{ref} = 4 \times 10^{-16}\,\mathrm{W/m^2/Hz}$. This intensity corresponds to a reference distance $d = 0.5\,\mathrm{m}$, from the showers produced by an electron beam of $2.8 \times 10^{10}\,\mathrm{eV}$. The measured flux integrated for the used frequency band [1.5-6 GHz] is shown in figure 5.6. The signal is measured using a cross-polarized antenna which is insensitive to radiation polarized with the electron beam. The intensity of the electron beam was 1.2×10^7 e/pulse, so the equivalent energy in an extensive air shower was $E_{ref} = 3.36 \times 10^{17}\,\mathrm{eV}$. To compute the corresponding flux for an air shower (F_{shower}), the following expression can be used [69]:

$$F(t) = F_{ref}\Gamma\frac{\rho}{\rho_{ref}}\left(\frac{d}{r(t)}\right)^2\left(\frac{N(t)}{N_{ref}}\right)^{\alpha} \tag{5.1}$$

where ρ/ρ_{ref}, $d/r(t)$ and $N(t)/N_{ref}$ account for the different air densities, distances and number of particles in the observed shower and the reference laboratory experiment, respectively. α is a measure of the coherence of the emission, equal to 1 for a non coherent emission and equal to 2 for full coherence. In the case of the MBR emission, the emission is expected to be isotropic, so no coherence is expected ($\alpha = 1$), as no direction is favoured in the emission. $\Gamma = 4.62$ [82] accounts for the ratio between the shower lengths in both cases. The flux estimated at 0.5 m can be scaled to an equivalent flux in an extensive air shower at a distance of 10 km. The flux predicted at this distance, using the reference flux measured in this experience, is $F_{shower} = 2.77 \times 10^{-24}\,\mathrm{W/m^2/Hz}$.

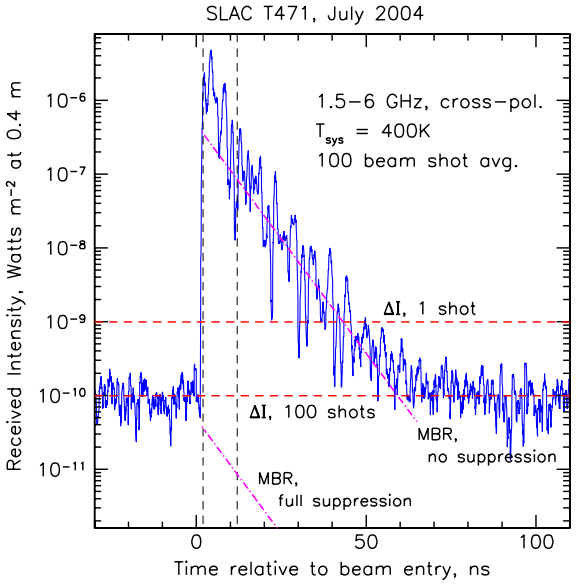

Figure 5.6 Integrated flux measured at the SLAC experiment with a cross-polarized antenna, from the showers produced by an electron beam of $2.8 \times 10^{10}\,\mathrm{eV}$. The frequency band is [1.5-6 GHz]. From [82].

The development of an instrument to measure the radio emissions of the extensive air showers

in this frequency range is the key to either the detection of the MBR emission, or the imposition of a superior limit to the intensity of the emission. Nevertheless, other approaches to this emission are also possible. In the following subsection, an estimation of the limit, a laboratory experiment to measure MBR emission, and an extensive air shower detection experiment are described.

Estimation of the MBR spectral intensity

In the line of the establishment of a superior limit for the MBR flux, the estimation conducted by Al Samarai et al. [167] is noteworthy, as the calculation taking into account the effects in the whole process has not been done before. A detailed calculation of the spectral intensity of photons at ground level, for a vertical shower with energy $10^{17.5}$ eV, was conducted. The calculated spectral intensity at ground at 10 km from the shower axis is lower than that expected by Gorham et al. [82]. At this distance, the flux calculated by the authors is $F_{shower} = 4.8 \times 10^{-26}\,\mathrm{W/m^2/Hz}$ (see figure 5.7), concluding that microwave detectors with good sensitivity should detect the expected MBR emission.

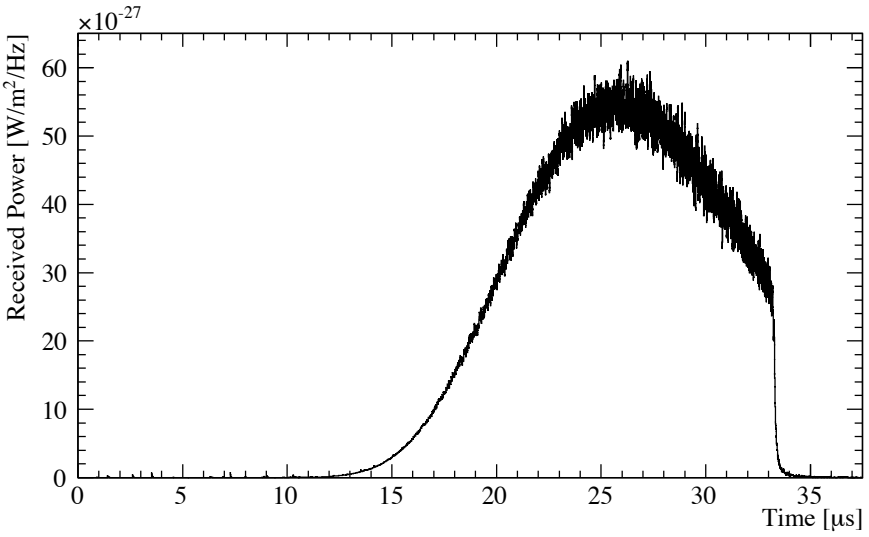

Figure 5.7 Estimated intensity of the MBR emission as a function of time expected at 10 km from the shower core at ground level, for a vertical shower with energy $10^{17.5}$ eV. From [167].

To compare with the reference flux at 0.5 m, again the equation 5.1 can be used. The same considerations as those assumed by Gorham et al. [82] are considered here. The distance (from 10 km to 0.5 m), the energy (from 3.16×10^{17} eV to 3.36×10^{17} eV), the lower density expected for a typical 5 km air shower altitude (a ratio of 0.6), and the factor $\Gamma = 4.62$ accounting for the ratio between the shower lengths in both cases. The result is a calculated flux of $F_{ref} = 7.36 \times 10^{-18}\,\mathrm{W/m^2/Hz}$.

AMY

Laboratory experiments have also been conducted to measure the radio emission in the GHz range in accelerator facilities. In this frame, the AMY experiment [84, 169, 176, 177], whose collaboration includes the author of this thesis, is designed to characterize the process of emission of MBR. In the AMY experiment, this was carried out by measuring radio emissions produced by an electromagnetic air shower in the wide band from 2 to 20 GHz, by using a beam of 510 MeV electrons at the Beam Test Facility (BTF) at Laboratori Nazionali di Frascati, Italy.

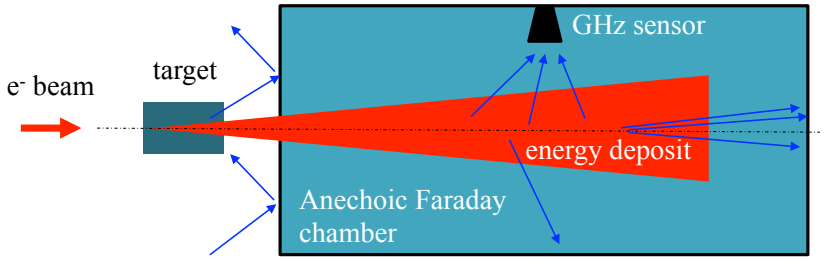

Figure 5.8 Sketch of the AMY experiment. The chamber is a copper anechoic chamber (2 m × 2 m × 4 m) whose interior was covered with pyramidal RF absorbers. From [177].

The beam was deviated to a copper anechoic chamber (2 m × 2 m × 4 m) whose interior was covered with pyramidal RF absorbers, and can hold up to 5 antennae (see figure 5.8). The kind of antennae used was *Rohde&Schwarz (R&S) HL050* log-periodic antennae and *RF Spin Double Ridged Waveguide Horn DRH20*. The beam particles were colliding with an alumina target of variable thickness placed between the beam pipe exit and the chamber, varying the target thickness from 2.5 cm to 45 cm, corresponding from less than 1 to 7 interaction lengths. Different data taking periods have taken place with different bunch lengths in December 2011 (10 ns), May 2012 (3 ns) and December 2012 (1.5 ns).

The AMY experiment has not found evidence of MBR emission, concluding that the MBR might not be useful for cosmic rays detection. The data analysed until the writing of this work (more data collection is booked for the end of 2014) show a density flux (at 4.7 radiation lengths) of approximately $F_{ref} = 5 \times 10^{-17}\,\mathrm{W/m^2/Hz}$, as transformed from the conditions at the AMY experiment to those at SLAC by Gorham et al. [82], and to make possible the comparison.

GHz array at Auger

The final and direct method to evaluate the MBR emission is the development of a ultra-high energy cosmic rays radio detector. To search for this emission in the GHz band, according to the atmospheric transparency and the availability of low cost commercial equipement, the chosen band was the C-band, between 3.4 and 4.2 GHz. In the MHz band, the ground affects the radio measurements because it reflects the emission coming from the source, and the radiation length is comparable to the distance between the antena and the ground (typically 3 m). In the GHz band, the distance from the antenna to the ground is large enough to

make that the direct signal and the reflection are not in phase anymore, so the reflection is not an issue. On the contrary, the antenna is sensitive to the emission of the ground at the temperature of the site. In the GHz range, the ground is a source at $T \approx 270\,\mathrm{K}$.

Regarding the previous efforts carried out by the EASIER group, another hexagon with feed horn antennae was installed in april 2011, and it was completed with 54 more a year later, covering a surface of $91\,\mathrm{km}^2$. This array is located in the south west part of the Observatory, in the field of view of one of the four fluorescence detectors (Los Leones), and in the field of view of the MIDAS telescope (see section 5.2). In June 2011, the first evidence of radiation emitted in the GHz range by an extensive air shower was observed. The calibration was conducted using an external source carried by an octocopter flying above the station. Three clear candidates were analysed at distances to axis smaller than 300 m, although more events have been registered after this analysis. The comparison with simulation for these specific cases was done to infer the emission process responsible. Some of the parameters, taken alone, could be compatible with an isotropic emission, like the amplitude. However, the amplitude of the signal, time length and distance to the axis, analysed together, favoured a beamed emission as dominant emission process. Also the orientation of the antenna that detected the radio signals (East-West) favours a geomagnetic origin.

Several conditions were requested to reject possible geomagnetic effects in the detected signal. Besides, a minimum energy of $10^{19}\,\mathrm{eV}$ was also a requirement. In the absence of MBR candidates, an upper limit was calculated simulating proton and iron showers with a scan in F_{ref} and α. The limits on the reference flux F_{ref} as a function of the coherence index α (see equation 5.1) are given in figure 5.9. It was found that $F_{ref} \leq 8 \times 10^{-16}\,\mathrm{W/m^2/Hz}$ for $\alpha = 1$ and 95% CL [69].

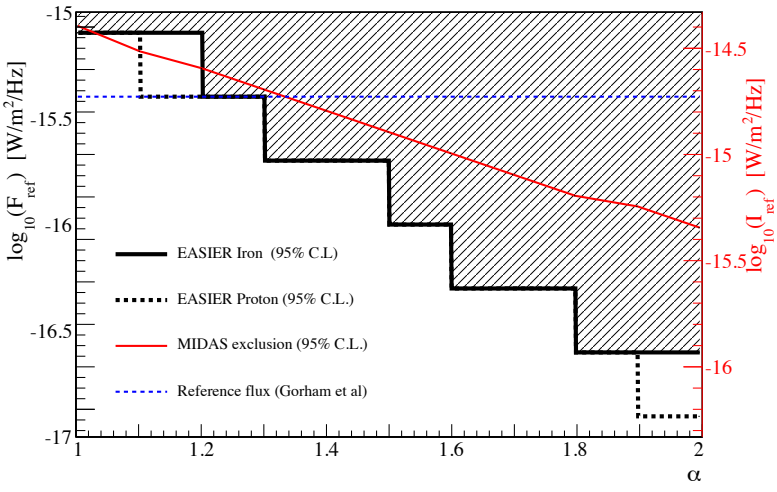

Figure 5.9 Limits set on the MBR flux with EASIER GHz array as a function of the coherence parameter α. The dashed blue line represents the flux measured by Gorham et al. [82]. The solid red line represents the upper limits set with MIDAS detector. The right axis shows $I_{ref} = F_{ref} \times 4.62$. From [69].

The GHz array is still collecting data, and small changes have been conducted to improve the

noise reduction and the data acquisition. Nevertheless, the absence of clear MBR candidates leads to a new configuration of the detector to optimize the detection at large distances from the shower axis. This ongoing work is detailed in the next section.

5.6 The Giga Duck array

The EASIER experiment is currently focused on the study of the detection of the MBR emission. Several modifications over the GHz configuration are conducted in the search of larger statistics, resulting in the new Giga Duck configuration. The two major changes are the lowering of the operating frequency and the new configuration in the orientation of the antennae.

New antenna and operating frequency

The former central frequency was 3.8 GHz, in a band from 3.4 to 4.2 GHz, with a *LNBF GI-301SC* antenna. This range is also studied in the Giga Duck, but with a new sensor, a Pyramidal 15 dB Horn antenna coupled with a Norsat antenna.

In a second hexagon test, a new range is added around the central frequency of 1.2 GHz. The reason for this change in frequency is that the effective area increases for larger wavelengths. The final working frequency range is $[1.05 - 1.45\,\mathrm{GHz}]$, selected with a band-pass filter. In this second range the antenna used is a High Gain Directional Helix antenna [178], and it will be referred as helix antenna (see figure 5.10, left). To improve the sensitiveness of the system, a parabolic dish has been attached to the antenna. This dish is designed to be light and to present a minimal wind resistance. The simulated radiation pattern of the antenna (without the parabolic dish) is represented in the right panel of figure 5.10. The forward direction (0 in the polar diagram) shows a maximum in the pattern.

Change in the array configuration

To maximize probability to detect the MBR emission, the antennae will no longer be in the vertical position, but pointing to the center of an hexagon, as described in figure 5.11 (left). The chosen zenith angle for this configuration is $\theta = 20^{\circ}$, except for the central antenna, in vertical position. This configuration is favoured by the higher directionality of the helix antenna. Although the benefit in the Horn+Norsat antenna is not that big, the configuration is maintained for the two hexagons.

To find the optimal position of the antenna, high frequency structural simulator (HFSS) simulations have been conducted, with different inclinations, in order to obtain the received signal at different distances from the shower axis. The simulations show that an inclination of $\theta = 20^{\circ}$ gives a gain factor of 2.5 with respect to the vertical position (see figure 5.11, right).

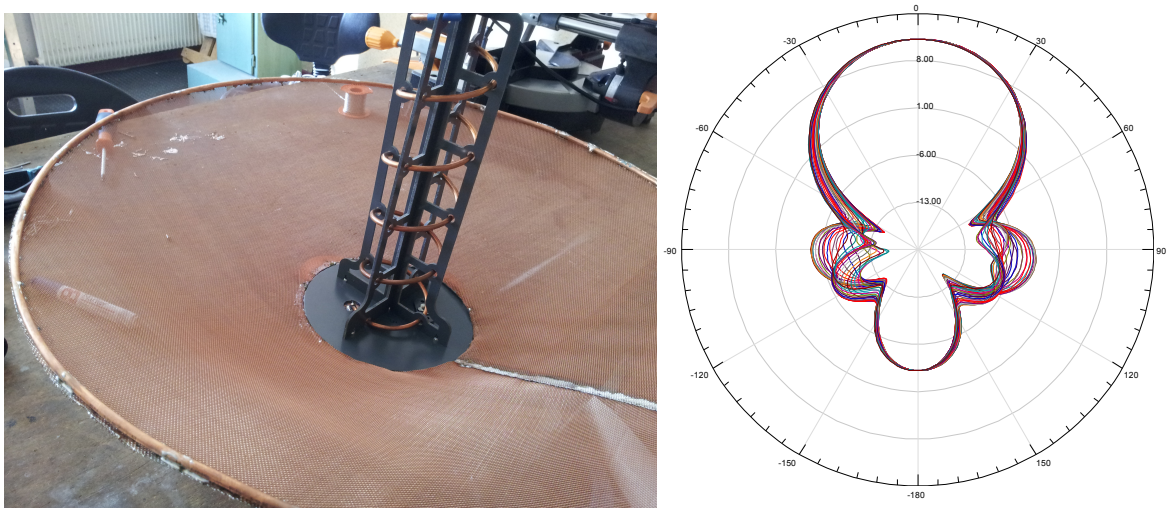

Figure 5.10 Left: High Gain Directional Helix antenna [178] (helix antenna) used in the Giga Duck configuration, attached to a parabolic dish. Right: simulated radiation pattern of the helix antenna. The azimuth of the polar diagram represents the angle with respect to the axis of the antenna. The radius in the polar diagram represents the gain. The different lines represent the angle around the axis of the antenna. Simulations by C. Bérat and P. Stassi.

Background noise

Background noise rejection is a key step in radio detection. There are several possible sources of noise. The first possibility is a noise coming from the normal functioning of the WCD during the trigger. To know if the electronics of the station could provoke the radio signal, a study was conducted by the EASIER group in 2011, by inducing fake signals in the WCD [179]. The result was negative, discarding this source as noise. Despite this, one of the main problems in the MHz attempt was the non identified background noise. Facing the Giga Duck project, one of the first steps has been to be sure that the frequency band is clean.

A campaign of background measurements was performed in february 2014 at Auger. The chosen helix antenna, with a detection maximum in the range between 1.0 and 1.6 GHz, was used to this purpose. In the set up of the measurement (see figure 5.12), an amplifier between the antenna an the spectra analyser amplifies the signal with a gain of 25 dBm. The spectrum analyser (Anritsu Spectrum Master MS2723B [180]) records the amplified signal detected by the Helix antena. The chosen range is between 800 MHz and 2200 MHz. Two different locations were studied. The first was at a few metres from Lina SD station (ID 266, GPS location 35.407 627°S 69.254 665°W), where the MHz hexagon had been installed. The background noise was measured in the four cardinal directions (NSEW) and at different zenith angles. The second location was on the roof of Los Leones FD building (GPS location 35.495 818°S 69.449 746°W, FoV direction: 30°, between NNE and NE). Measurements were performed for four different zenith angles, pointing always to the direction of the array, that is to the center of the field of view of the FD station.

As shown in figure 5.13, a wide range from 1000 MHz to 1900 MHz is clean of disturbing

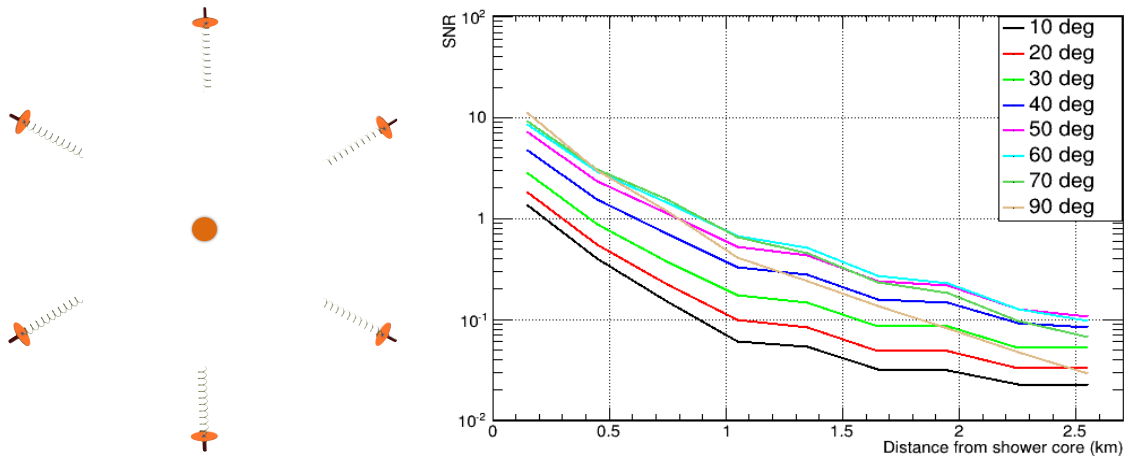

Figure 5.11 Left: configuration of the Giga Duck hexagon, with the exterior antennae pointing to the center at 20° of zenith angle. Right: signal-to-noise ratio (SNR) for the helix antennae for different zenith angles. In the figure is represented $90 - \theta$. Simulations by Al Samarai.

background noise that could spoil the data. Then, a detection project in this range is possible. However, some characteristics of these background measurements are worthy to be explained. First, the signals in both panels of figure 5.13 detected at 900 MHz (only seen for $\theta = 90°$ in the left panel) are caused by the communication system of the SD. The stations send pulses every time a T2 event is detected. Second, the peaks registered around 1950 MHz in the right panel of figure 5.13 are also caused by the communication system, more complex in the case of the FD station. Finally, the noise floor found in the whole range of frequency with value between -65 and -70 dBm, could be due to noise induced by the detection system.

Final configuration and future installation

The Giga Duck hexagon is planned to be installed during the first months of 2015. Seven SD stations will be equipped with a High Gain Directional Helix antenna, six of them oriented to the center of the hexagon at 20° of zenith angle, and one of them, in the centre, at vertical position. The signal will be filtered by a pass band filter in the frequency range of $[1.05 - 1.45\,\text{GHz}]$.

The fluxes already measured in other experiments suggest that this technique is very limited for extensive air shower measurements. Aware of this limitation, the main purpose of this project is to better describe the process, by, mainly, establishing a limit in the MBR emission.

5.7 Conclusions

The access to the longitudinal profile of the extensive air shower is a key step to infer the mass of the primary particle. The study of the radio emission of the shower has been proposed as an alternative with full duty cycle to the fluorescence technique. The processes of radio emission

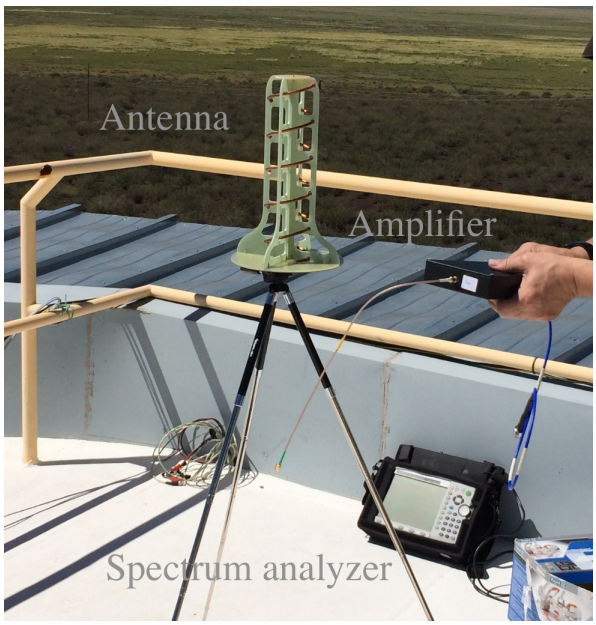

Figure 5.12 Background noise measurements: High Gain Directional Helix antenna, amplifier box (25 dBm) and Anritsu spectrum analyser.

investigated in this thesis are two: the geosynchrotron emission and the MBR emission. The former is a beamed emission and the latter is isotropic.

The different trials at Auger did not reveal any detection far from the shower axis, favouring, along with other analysis, a geosynchrotron interpretation of the emissions detected. This emission process has been proven to be detectable in the MHz frequency range, but limited in the application to infer the mass in ultra-high energy cosmic rays, as it requires a large sample of radio detectors to cover the large surface that it is needed.

The MBR emission, being isotropic, is much more interesting to help in the identification of the mass of the primary particle. This topic has been attacked from different points of view. Analytical calculations of the expected flux have been carried out and the intensity has been measured in accelerator experiments, whereas limits on this flux have been established in extensive air showers detection experiments at the Auger site. All these results are summarized in figure 5.14 and in table 5.1. A correct determination of the MBR flux will put light on the feasibility or not of this technique to be used in the detection of ultra-high energy cosmic rays, as the detection experiences do not reveal, up to now, a significant flux that could confirm this emission as a future technique.

The Giga Duck project is also presented, where the MBR emission is aimed to be detected with radio antennas in the GHz frequency range. The antenna, the orientation and the general configuration of the testing array have been optimized to maximize the number of detected showers. The principal objective of this ongoing project is to properly characterize the MBR emission.

Table 5.1 Different fluxes measured or estimated by different publications or experiences. For a reference distance of $d_{ref} = 0.5\,\mathrm{m}$, an energy of $E_{ref} = 3.36 \times 10^{17}\,\mathrm{eV}$ and $\alpha = 1$.

Experience or author	F_{ref} at $d_{ref} = 0.5\,\mathrm{m}$	
SLAC [82]	$4 \times 10^{-16}\,\mathrm{W/m^2/Hz}$	Measured in accelerator experiment
AMY [169]	$5 \times 10^{-17}\,\mathrm{W/m^2/Hz}$	Measured in accelerator experiment
Al Samarai et al. [167]	$7.36 \times 10^{-18}\,\mathrm{W/m^2/Hz}$	Estimation
EASIER [69]	$8 \times 10^{-16}\,\mathrm{W/m^2/Hz}$	Upper limit (95% CL) measured at Auger
MIDAS [181]	$10^{-15}\,\mathrm{W/m^2/Hz}$	Upper limit (95% CL) measured at Auger

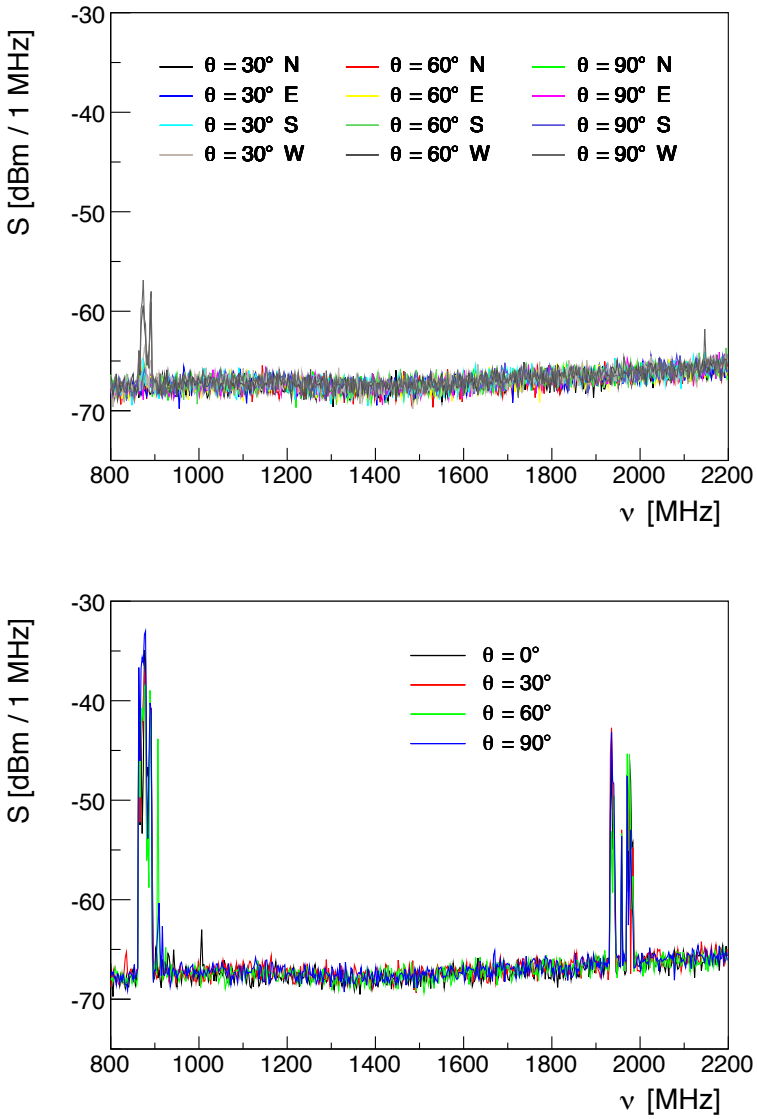

Figure 5.13 Above: background noise in the Lina SD station for 12 different arrival directions. Below: background noise in Los Leones FD station for 4 different arrival directions.

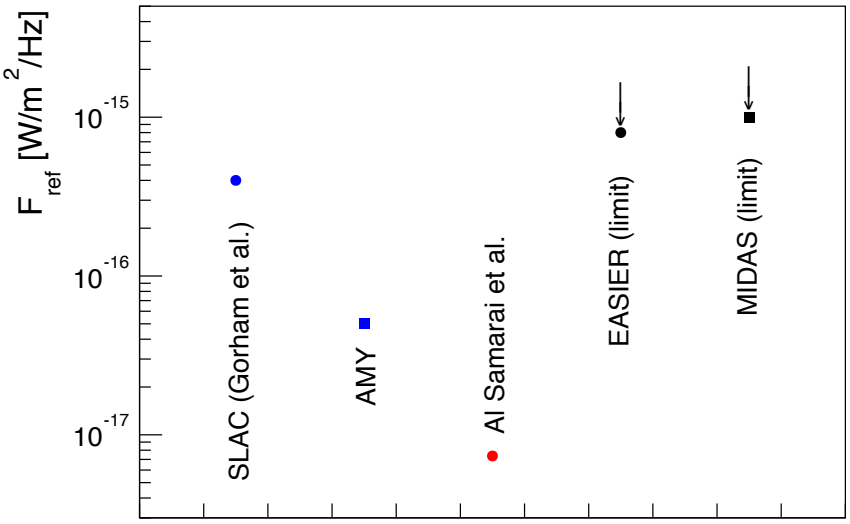

Figure 5.14 Different fluxes measured or estimated by different publications or experiences. For a reference distance of $d_{ref} = 0.5\,\mathrm{m}$, an energy of $E_{ref} = 3.36 \times 10^{17}\,\mathrm{eV}$ and $\alpha = 1$.

Chapter 6

Layered Surface Detector

The third approach to attack the mass composition problem is the proposal of a new kind of detector with sensitiveness to the muon component of the extensive air shower. As shown in figures 3.2 and 3.3, the separation between primaries can be achieved by the knowledge of N_μ- or $X_{\max}$-related parameters.

As described in chapter 1, the WCDs currently used in cosmic ray observatories as HAWC or Auger do not distinguish between the different components of the extensive air shower, measuring a unique signal. A novel design for future WCDs is proposed here. This design will allow the future cosmic ray observatories to measure the muonic and electromagnetic components independently. This measurement will allow for composition analyses without suffering from the duty cycle limitations of the fluorescence detectors.

The design concept of the proposed detector, the Layered Surface Detector (LSD) [182], along with the application to the WCDs of the Pierre Auger Observatory, is described in section 6.1. The properties and performances for mass composition studies are discussed in section 6.2. The calibration strategies are detailed in section 6.3. The construction and installation of several prototypes and the data collected with them are detailed in sections 6.4 and 6.5, respectively. The design concept, the simulation studies and the prototypes data analysis are included in a recent publication [182].

6.1 Design principles

Physical Principle

Two parameters are needed to have sensitiveness to the two different components of the extensive air shower (muonic and electromagnetic). The basis of the idea is to separate the WCD in two different volumes, each of them responding differently to the incoming particles.

The physics principle that allow to distinguish between different particles is the energy absorption in the WCDs. Muons deposit their energy in a long or deep path inside the WCD, whereas the electromagnetic particles (electrons, positrons and photons) are absorbed in the first part of the water volume.

Muons of a few GeV energy (figure 1.4) deposit 2 MeV/g/cm^2 in the water of the detector. The muons are minimum ionizing particles and they pass through the water leaving an amount of energy proportional to their track length. A vertical muon leaves on average 240 MeV (see section 1.4 for the definition of the VEM unit).

Electrons and positrons deposit much more energy in water than muons, due to the different ratio between mass and charge. The energy they carry when arriving at the surface ($\sim$ 10 MeV, figure 1.4) is deposited in less than 5 cm.

Photons deposit their energy over a radiation length ($\sim$ 36 cm in water). Other components of the extensive air shower are negligible.

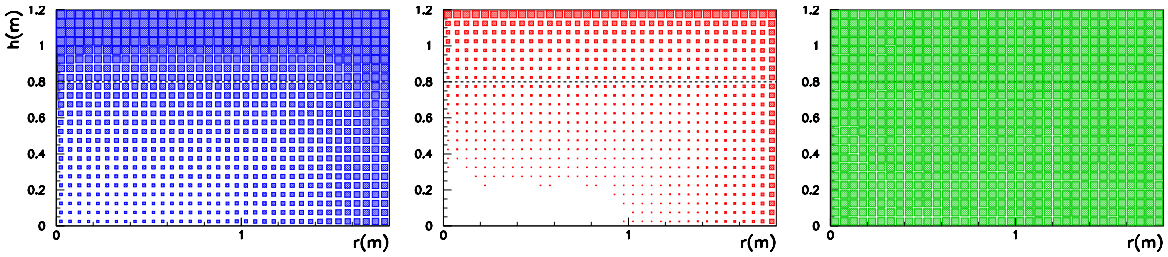

Figure 6.1 Distribution of the production points of Cherenkov photons in an Auger WCD (1.2 m height, 1.8 m radius). h represents the height of the detector and r the radius. Different incoming particles are represented: (left) photons, (center) electrons and positrons and (right) muons. Those secondary particles come from a 30 EeV extensive air shower with 45° zenith angle.

To support this first approximation analysis, the production points of Cherenkov photons produced by different incoming particles in a water volume equivalent to that of an Auger detector is shown in figure 6.1. For photons (left), electrons and positrons (center) and muons (right). The incoming particles are the secondary particles produced by a 30 EeV extensive air shower with 45° zenith angle. As predicted, the muons deposit the energy all along the volume, while electromagnetic particles deposit it in the top and side.

Layered design

Based on the physical principle of the different absorptions, a new WCD can be designed. If the water volume of the WCD is split horizontally in two parts, the two volumes will respond differently to the same extensive air shower. The muonic component will produce Cherenkov light in both volumes whereas the electromagnetic one will do it, essentially, in the first one.

A LSD can access to both the electromagnetic and the muonic component of an extensive air shower. The simplest design for a LSD is a cylindrical WCD split in two volumes separated horizontally, but extra shielding for the volume below (more sensitive to the muonic component) can be imagined.

A modification of an Auger WCD has been done to illustrate the performances based on this

design. As described in section 1.4, the Auger WCD has a water volume with 1.2 m height and 1.8 m radius. The detector can be converted into a LSD by inserting a horizontal reflective layer at an appropriate distance (this will be defined in next subsections) from the bottom.

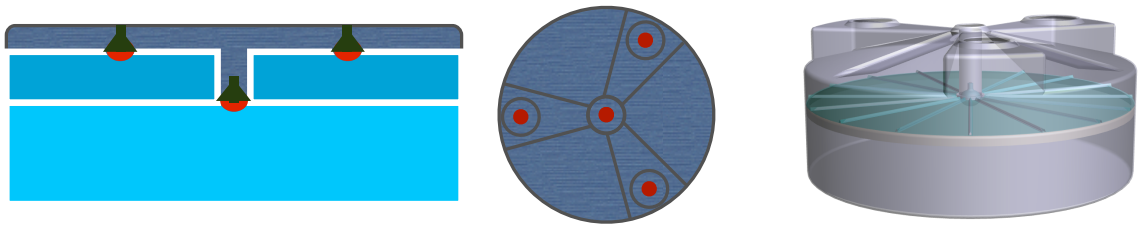

Figure 6.2 Sketch with different perspectives of the proposed design of the LSD built from a standard Auger WCD.

The proposed design is composed by two liners one above the other. The bottom liner has a single PMT (identical to the current Auger PMTs) at the top center. The top liner has a 10 inches cylindrical hole in the middle, to ensure the access to the bottom PMT. The three current PMTs remain in the same position for the top liner (figure 6.2).

Signals of the muonic and electromagnetic components

In the LSD two different signals are registered: the signal in the top liner (S_{top}) and the signal in the bottom liner (S_{bot}). The signal in both liners is given by the muonic and electromagnetic component. Each component contributes to the total signal with the muonic signal (S_μ) and the electromagnetic signal (S_{em}), respectively. The system relies on the fact that the two components deposit different amount of energy in each liner. The signal in the top liner is:

$$S_{top} = a\ S_{em} + b\ S_\mu \tag{6.1}$$

leaving the rest of the energy of each component to the signal in the bottom liner:

$$S_{bot} = (1-a)\ S_{em} + (1-b)\ S_\mu \tag{6.2}$$

In the two equations a is the fraction (over the total in the LSD) of energy that the electromagnetic component deposits in the top liner and b is the fraction of energy that the muonic component deposits in the top liner too. Neglecting the influence of other components of the extensive air shower, the total signal of the station is obtained equally by summing the signal in the two liners (*top + bottom*) or the signal of the two components (*muonic + electromagnetic*).

$$S_{station} = S_{top} + S_{bot} = S_\mu + S_{em} \tag{6.3}$$

The equations above can be expressed in one single 2×2 matrix:

$$\begin{pmatrix} S_{top} \\ S_{bot} \end{pmatrix} = M \begin{pmatrix} S_{em} \\ S_{\mu} \end{pmatrix} = \begin{pmatrix} a & b \\ 1-a & 1-b \end{pmatrix} \begin{pmatrix} S_{em} \\ S_{\mu} \end{pmatrix} \tag{6.4}$$

If the matrix can be inverted, the muonic and electromagnetic signal can be retrieved as:

$$\begin{pmatrix} S_{em} \\ S_{\mu} \end{pmatrix} = M^{-1} \begin{pmatrix} S_{top} \\ S_{bot} \end{pmatrix} \tag{6.5}$$

The determinant (D) of the matrix is $D = a - b$, and it is maximum for $a = 1$ and $b = 0$. At this maximum all the electromagnetic component would be deposited in the top liner and all the muonic component in the bottom one. This would be the ideal case, but in a realistic situation a is always less than one and b is always larger than zero. The statistical uncertainty in the reconstructed signal for the two components is driven by $1/D$.

Optimal separation height

A first theoretical approach, based on the case of a vertical extensive air shower, can be done to determine the optimal separation height. Modeling the absorption of the electromagnetic component by an exponential decay according to the radiation length X_0, and for a station of height H with a layer interface located at a distance $H - h$ from the bottom, the coefficients a and b, for a vertical case, are:

$$\begin{aligned} a &= 1 - e^{-h/X_0} \\ b &= \frac{h}{H} \end{aligned} \tag{6.6}$$

with $h \in [0, H]$ .The determinant D is maximum for $h = X_0 \ln(H/X_0)$. If H is large enough (with a radius sufficiently large to avoid side contributions) a tends to 1 whereas b tends to 0. This is the ideal case with a determinant $D = 1$. For the particular case of the Auger WCDs, with $H = 120\,\text{cm}$ the determinant is maximum for $h = 43\,\text{cm}$ (see figure 6.3).

The dashed line in figure 6.3 indicates the region where the determinant is higher than 95% of its maximum value. A wide range in h is found over the dashed line, so the layer can be placed at any point between 35 and 50 cm. The value chosen for h is 40 cm. That leaves a bottom liner 80 cm high (2/3 of the total height) and top liner 40 cm high (1/3 of the total height).

However, even if this theoretical approach gives already values for the matrix coefficients a and b, the final values have to be determined by simulation analysis in a more realistic approach. The calculation of the coefficients and the characterization of the performances of the detector by simulation analysis is detailed in the next section.

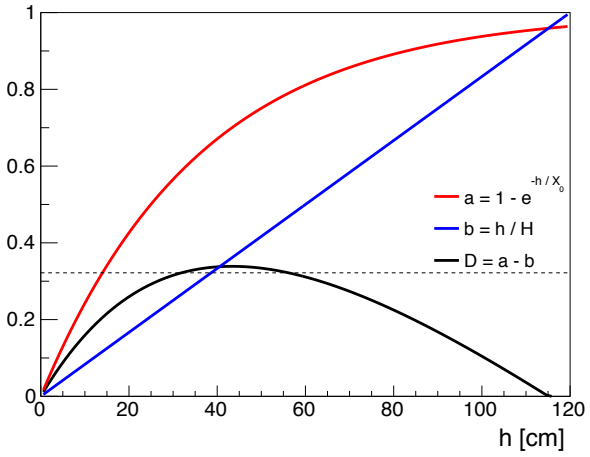

Figure 6.3 The maximum value of the determinant indicates where to split the water volume. A compromise between a high a and a low b is searched. The pointed line marks the 95% of the maximum value of the determinant. The example is done for the particular case of the Auger WCD, where $H = 120\,\text{cm}$. $X_0 = 36\,\text{cm}$.

6.2 Performances

Simulations

To characterize the performances of the LSD, simulations of the detector response have been performed. A set of extensive air showers has been simulated with the CORSIKA code, using EPOS LHC and QGSJet-II-04 as high energy interaction models and FLUKA at low energies. Various libraries have been generated with a uniform distribution in $\cos^2\theta$ for different primary types (proton, helium, nitrogen and iron) and in two energy intervals (from 8 to 13 EeV and from 40 to 60 EeV, uniformly distributed in the logarithm of energy). The first energy range is the a energy taken as reference in Auger due to the spacing between stations. The second energy range is were the suppression of the energy spectrum takes place.

Matrix universality

The matrix coefficients are derived from simulations as the ratio between the photoelectrons collected in the top liner over the total number produced in both volumes for the electromagnetic (a) and the muonic component (b). In figure 6.4, the ratio for the electromagnetic and muonic components is shown for different primaries and hadronic models represented as a function of zenith angle and distance to the axis. A remarkable property is that the values of the matrix coefficients are essentially independent of the primary type, the primary energy, the particular simulation model used to describe the extensive air shower and the distance of the station to the axis. Due to the geometry (ratio between the height and the radius) of the WCDs of Auger, the coefficients are also independent of the zenith angle of the extensive air shower in the range $[0°, 60°]$.

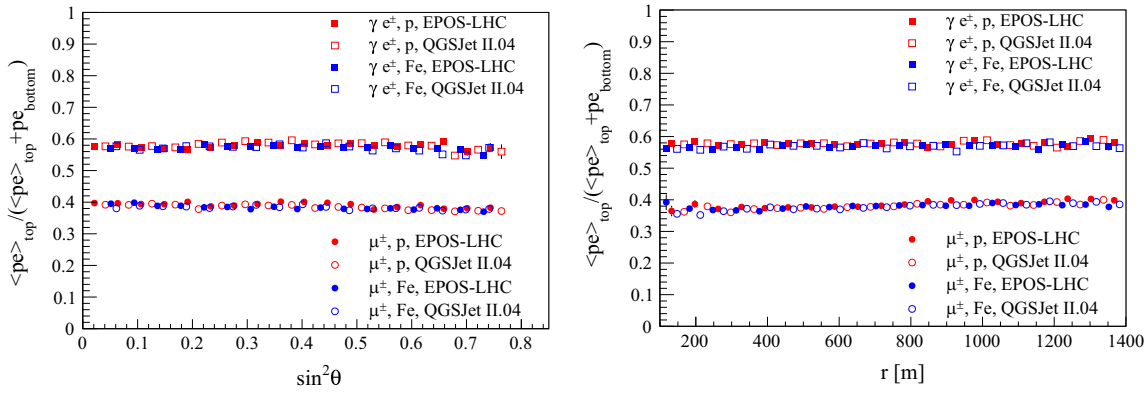

Figure 6.4 Fraction of photoelectrons created by the electromagnetic component in the top liner (a) and fraction of photoelectrons created by the muonic component in the top liner for proton and iron nuclei showers at (b) at different zenith angles (left) and at different distances from the axis (right).

For the particular case of the LSD from the modified Auger WCD the parameter a is nearly 0.6 while b is about 0.4. This leads to a determinant $D = 1/5$.

Signal reconstruction

A well defined matrix gives the possibility to extract the signals due to the two components from each station, by applying the transformation in equation 6.5. An example is shown in figure 6.5 for a 11 EeV shower at 46° zenith angle. The shown agreement between the reconstructed traces of the two components and the generated ones demonstrates the separation power of the LSD.

The muon signal in the LSD can be reconstructed in a wide range of distances from 200 m to more than 2 km for the highest energies (see figure 6.6, left). As shown in figure 6.6 (right), the signal resolution in each detector is better than 25% when more than 20 muons enter the detector. For lower signals the Poisson fluctuations dominate.

Once the electromagnetic and muonic signals are extracted, they can be used for the shower reconstruction. The LDF (see section 1.4) can be reconstructed separately for the two components. Figure 6.6 (left) shows the two reconstructed LDFs, compared with the true signals. The agreement between the true and the reconstructed signal is good at very different distances from the axis. The independent LDFs have several benefits. First, the energy estimator S_{1000} can be calculated using the electromagnetic component, less sensitive to uncertainties derived from interaction models that use mixed electromagnetic and muonic signals. Second, the average muonic signal at 1000 m (S^{μ}_{1000}) can be obtained from the muonic LDF, directly related to N^{μ}_{1000}, and this to N_{μ}, a mass sensitive parameter (see section 3.1).

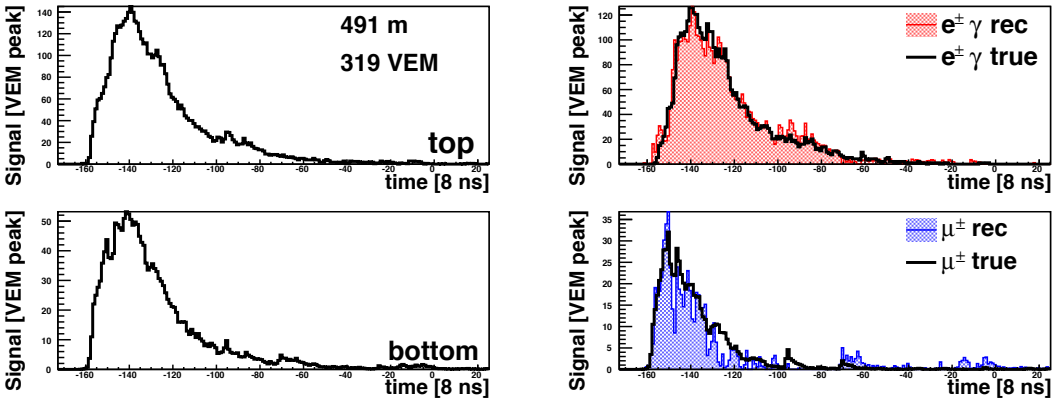

Figure 6.5 Left: simulation of the signal collected in the top and bottom volume of a $10\,\mathrm{m}^2$ LSD for a 11 EeV shower with 46° zenith angle and 491 m away from the axis. Right: the reconstructed muon and electromagnetic traces compared to the generated ones. The agreement is striking both in shape (timing information of the two components) and amplitude.

Observables for composition

The composition analysis relies on two main observables: $X_{\max}$ and N_μ (see chapter 3). The latter can be derived by applying to the muonic LDF the usual approach for shower size in the SD in Auger: the S_{1000} estimator. The reference distance is adopted as that adopted in Auger for the total signal, but optimal values can be derived in the future. This method returns S^{μ}_{1000}, as an estimator for the number of muons, N_μ. In the left panel of figure 6.7 it is shown the distribution of S^{μ}_{1000} for protons and iron nuclei showers. The resolutions of the distributions are 24% for proton and 13% for iron at 30 EeV. This value improves to about 10% for both primaries at energies above 70 EeV. The calculated MF (see its definition in equation 3.1) between the distributions for the reconstructed proton and iron muon size changes with energy and zenith angle. In the case shown in figure 6.7, the value of MF = 1.74, indicates a good separation power.

As an $X_{\max}$-related parameter, the signal start-time at 1400 m (T_{1400}) is used, which measures the delay of the shower particles with respect to the arrival time of an imaginary planar front. This parameter is sensitive to the shower front curvature and correlates with $X_{\max}$. In this particular example we have used a timing resolution of 8 ns, which can be easily achieved with the help of modern GPS receivers. This corresponds to an $X_{\max}$ resolution between 40 and $60\,\mathrm{g/cm}^2$, depending on zenith angle. In the right panel of figure 6.7, the distributions of the estimated T_{1400} are shown. The resolutions of the distributions and the MF are also indicated. The parameter T_{1400}, used in figures 6.7 and 6.8, is given as an example and it is not meant to be considered as the optimal variable for the analysis. Other parameters related with $X_{\max}$ or the age of the shower can be considered, and they can be retrieved following the universality principle of extensive air showers description, using, for example, the approach proposed by Ave et al. [183] or by Maurel et al. [184]. The universality principle says that it is expectable that the cascade description can be modeled from a reduced set of universal functions that

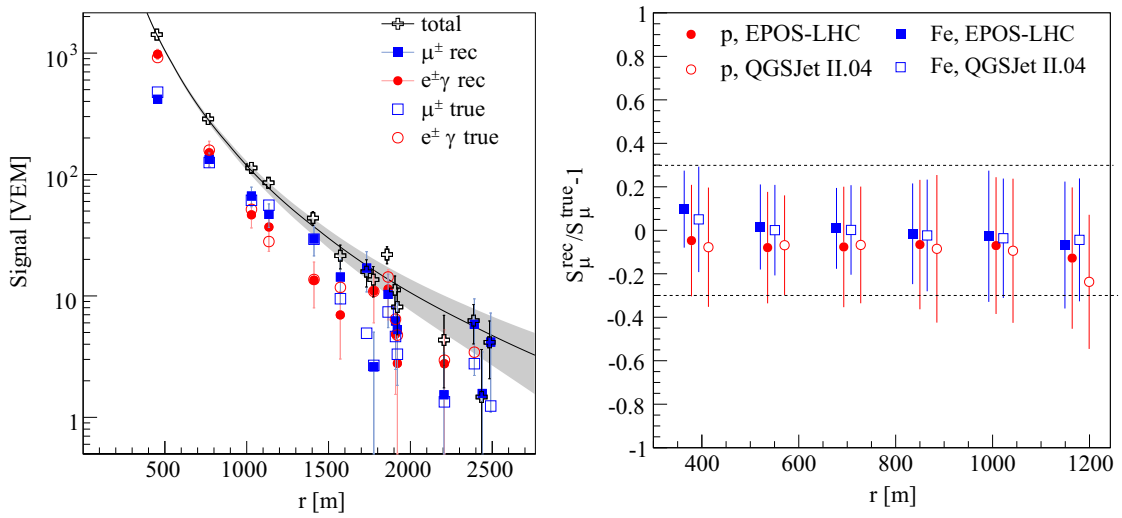

Figure 6.6 Left: example of muonic and electromagnetic independent LDFs reconstructed using the individual signals in each of the detectors. Right: individual LSD muon signal reconstruction as a function of the distance to axis for a shower with 10 EeV of energy. The error bars represent the signal resolution.

will depend on the shower age and whose relative amplitudes will carry the information on the primary type and energy. This concept has been extensively studied and validated with MC simulations and the arrival direction, the $X_{\max}$ and the muon size at ground, along with the energy, contain the essential information about the primary particle.

As indicated in chapter 3 (see figure 3.3), N_μ and $X_{\max}$ are parameters that can be combined. The combination of both of them increases the mass separation capability and it allows the construction of a new variable. In this case, even if the orthogonal observable to S^μ_{1000}, the T_{1400}, is not optimal, the procedure can be followed. The combined analysis is done for a 50% proton 50% iron mixed composition at 30 EeV, and the two ways are shown in figure 6.8. In the left panel the scattered plot for S^μ_{1000} and T_{1400} is shown. The Fisher separation coefficient (S_{fisher}) achieved is indicated in the figure. The dashed line represents the discriminant hyperplane, with which the new observable is constructed. The distributions for proton and iron for this new observable are shown in the right panel of figure 6.8, with the multi-dimensional parameter described in the label of the X-axis. The observable W_m can be used to interpret data in a more powerful way than taking into account S^μ_{1000} and T_{1400} separately.

The MF and the S_{fisher} are calculated as indicated in equations 3.1 and 3.3. For this particular case, S_{fisher} is significantly larger than 2, indicating that an excellent separation power can be achieved. It is worthwhile remarking that here the Fisher separation coefficient is obtained for a fixed primary energy in the simulation. In a realistic scenario both the energy and S_μ are estimated from the LSD data. It is expected that this will diminish the proton-iron separation. However, since it should be possible to experimentally estimate the energy by combining the $X_{\max}$ (or an observable related to it, like T_{1400}) with the shower size of the electromagnetic

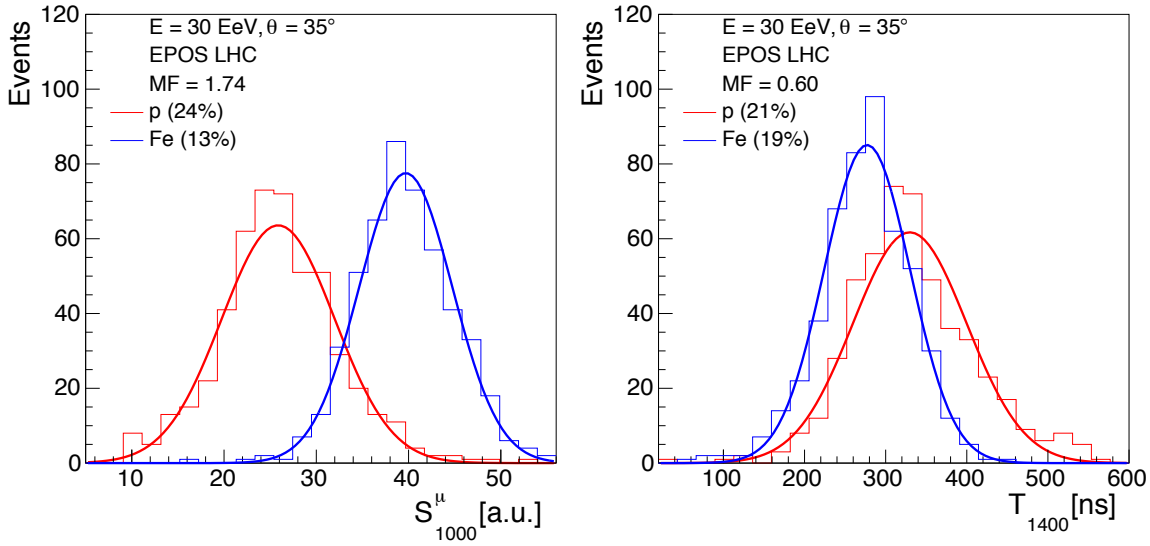

Figure 6.7 Distribution of the observables S^{μ}_{1000} (left) and T_{1400} (right) for the two different primaries. Showers simulated with EPOS LHC with 30 EeV and 35° zenith angle. The resolutions of the distributions (mean over rms) are between parenthesis. The merit factor (MF) is indicated.

component at ground, a Fisher value of about 2 is, in principle, possible.

6.3 Calibration strategy

An important aspect of surface array detectors for ultra-high energy cosmic ray studies is to have a calibration strategy that allows to monitor the conversion of the electronic signals into an equivalent energy deposit. In the case of the LSD the precise knowledge of the geometry of the volumes is a key point. The calibration is important not only because the conversion between the electronic signals into the equivalent energy deposit, but also because the relation between the sizes of the volumes defines the coefficients of the matrix. In the practical case of the prototypes designed in Auger (see section 6.4), even if the designed height (h in equation 6.6) is fixed, the volumes can change, as the current construction design does not allow for a rigid structure to completely fix the intermediate layer.

Muon peak

The calibration of the standard Auger WCD has already been addressed in section 1.4. The strategy described for the standard WCD can be applied to the LSD. This will be shown in the section 6.5, along with other details about the calibration and data of the installed prototypes.

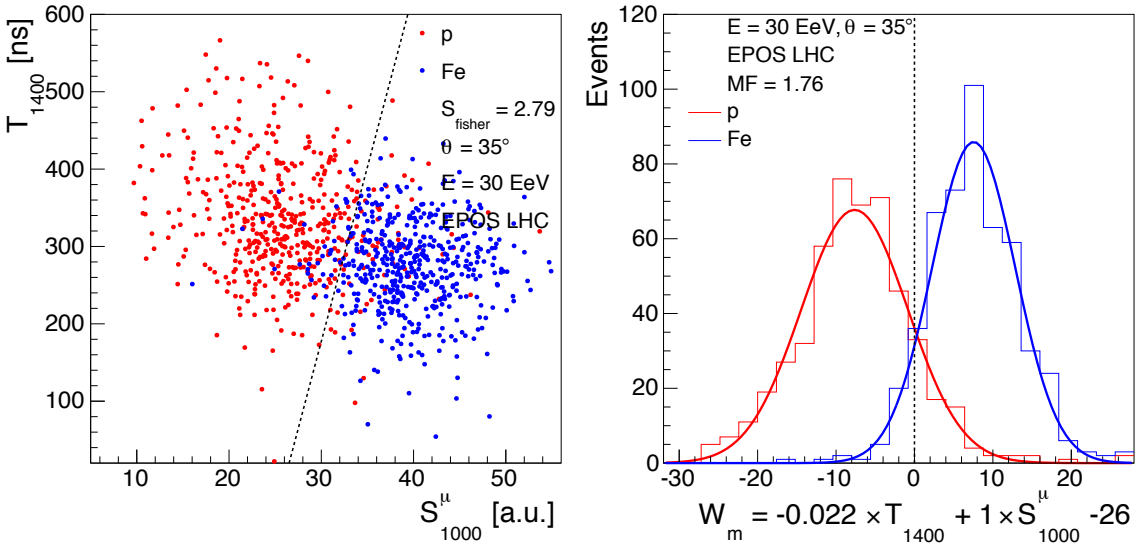

Figure 6.8 Two-dimensional analysis using the LSD reconstructed observables S^{μ}_{1000} and T_{1400}. The scattered plot is shown in the left panel, whereas the combination of both parameters in a new one is shown in the right one. For proton and iron primaries simulated with EPOS LHC in a extensive air shower with 30 EeV and 35° zenith angle. The Fisher separation coefficient and the merit factor are indicated.

Muon decay

An alternative calibration can be obtained using the muon decays that occur in the water volume. Nearly 4% of the muons entering the WCD stop and decay. The Michel electrons deposit on average an amount of energy that can also be used for calibration purposes. For the LSD it is also convenient to determine the water volumes geometry (the precise height of the water separation interface, due to possible imperfections in the prototype) as the matrix coefficients a and b depend on it. The muon decay is identified when two signals are registered in a short window of time, and one of the two signals is compatible with the incoming muon (leaving a signal inferior than a VEM) and the other being compatible with a Michel electron. The muon decay rate in the top and bottom liners is determined by the geometry of the detector and hence allows a precise determination of the position of the intermediate layer. A simulation based on 50,000 muon decays (this can be obtained in about 15 minutes of data taking assuming a decay selection efficiency of 50%) for three different positions of the interface is shown in figure 6.9. A 5 cm difference corresponds to nearly 10 standard deviations. A precision of a few millimetres in the position of the intermediate layer can thus be achieved.

Hybrid events and physics data

A cross calibration of the matrix coefficients within an array of LSD is also possible based on physics results. For each individual LSD, average (top and bottom) LDFs from a set of events can be constructed. From these average LDFs, by applying the matrix, muonic

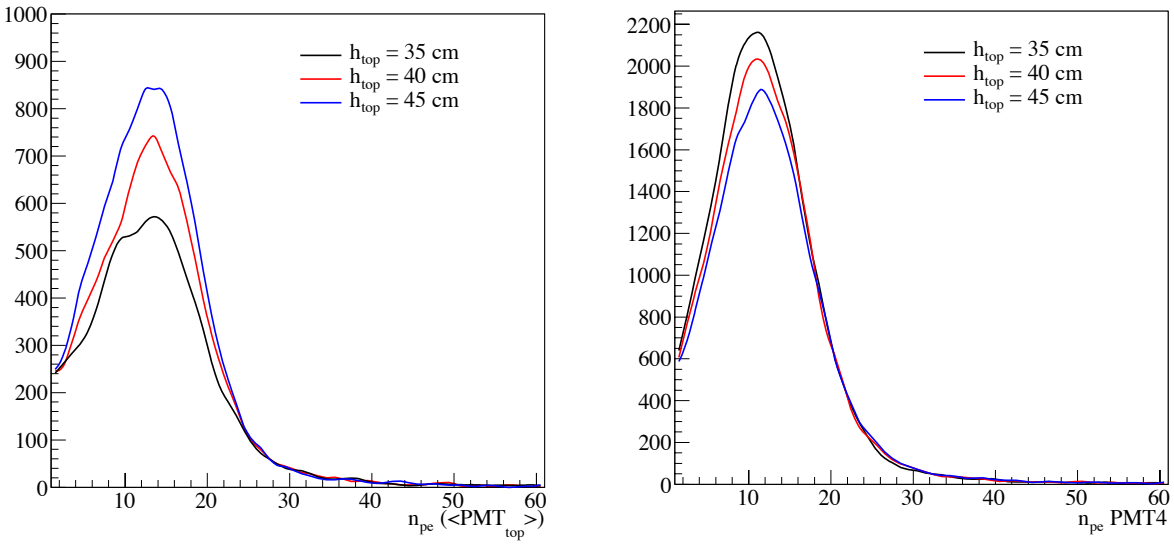

Figure 6.9 Signals from the Michel electrons from muon decaying inside the LSD for three different positions of the interface. Left: average signal in the three top PMTs. Right: signal in the bottom PMT. The statistic in the plot corresponds to about 15 minutes of data taking or 50,000 decays.

and electromagnetic average LDFs can also be independently reconstructed. Since these average LDFs should be identical for all LSDs, this is a mean to cross-calibrate all matrices (see section 6.5 for the mean LDFs of the data collected by the prototypes). Also, in a hybrid observatory such as Auger or the Telescope Array, the electromagnetic LDFs from the LSD can be calibrated using the fluorescence telescope data that give the cosmic ray energy by means of a calorimetric measurement of the electromagnetic energy deposit in the atmosphere [185]. This calibration scheme in Auger uses the total signal in the WCDs. In the LSD, the calibration will benefit from the electromagnetic signal reconstruction, as the uncertainty on the muon number in individual showers will no longer deteriorate the energy resolution of the surface array.

Propagation of uncertainties and systematics

When reconstructing the LDF from individual signals (S) measured in standard WCDs the uncertainty of each measurements is of the order of $\sqrt{S}$, with S expressed in VEM units. This is due to Poisson fluctuations of the number of muons entering the detector and to the fluctuation of the electromagnetic component in its high energy tail, which also introduce VEM-size Poisson fluctuations. The additional uncertainty associated with the signal measurement in the detector is due to the photoelectron statistic. As long as we have a number of photoelectrons per VEM much larger than one, its contribution to the uncertainty budget is negligible. Above 10 EeV, the signal at 1000 m is at least several tens of VEMs and the particle fluctuations due to the detector sampling become negligible compared to the shower-to-shower fluctuations. Indeed, above 10 EeV the energy resolution obtained from the LDF size at 1000 m from Auger SD is 12% while it should be around 5 to 6% if the particle

count was the only responsible for this uncertainty.

In a LSD the situation is similar even though the reconstructed muon and electromagnetic signals are linear combinations of the top and bottom signals with rather large coefficients. For a matrix with coefficients $a = 0.6$ and $b = 0.4$ we have :

$$\begin{aligned} S_{\mathrm{em}} &= 3S_{\mathrm{top}} - 2S_{\mathrm{bot}} \\ S_{\mu} &= 3S_{\mathrm{bot}} - 2S_{\mathrm{top}} \end{aligned} \tag{6.7}$$

However, the particle fluctuations in the top and bottom liners are correlated, whereas the photoelectrons fluctuations are not. In the particular case of the LSD geometry considered here, the contribution of the photoelectrons fluctuations in the reconstructed S_{μ} and S_{em} signals in each detector, although amplified by the large coefficients of equation 6.7, is still less than 25% of the particle fluctuations themselves. This has a little impact on the total uncertainty budget, specially at the highest energies where shower-to-shower fluctuations dominate.

Due to the relatively large coefficients entering in the reconstruction of S_{μ} and S_{em}, one must also consider the effect of a possible systematics in the absolute calibration of the top and bottom segments of the LSD. If the calibration procedure induces a systematic bias of +1% on the top segment with respect to the bottom one over the whole array, the electromagnetic signal from equation 6.7 would be on average 3% too large and the muon signal 2% too small (according to the equation system 6.7). Still, the LSD system can separate heavy from light primaries according to the muonic content of the extensive air shower, as all primaries would suffer the same systematic shift in the energy vs. muon size plane. The comparison with models becomes more difficult since the electromagnetic size, hence the energy, would be overestimated whereas the muon size would be underestimated. Given the calibration strategy introduced above, a maximum of 1% systematic uncertainty between the top and bottom calibration is within reach but requires attention.

6.4 Prototypes

Three LSD prototypes were constructed at the Auger site in Malargüe by inserting a separation made from a Tyvek laminate in standard liners from Auger. These prototypes use the 4 PMTs configuration displayed in figure 6.2 with 3 PMTs looking into the top volume and 1 PMT looking into the bottom one.

Two parallel options have been followed to achieve a prototype design whose installation can be carried out with minimal impact over the current WCD. One of the options contemplates the conversion (from standard WCD to LSD) without emptying the tank. This is the so-called *umbrella* option and it is still under development. The second option is to rebuild the liners, either from scratch, either modifying a current liner. This is the so-called *double liner* option and it has been adopted for the three installed prototypes.

Umbrella prototype

The *umbrella* is an extendable piece of liner that is introduced from a hole in the top centre of the tank (see figure 6.10). This method has two main benefits. The modification required in the original liners and tanks is minimal and the installation can be done in the field without removing the water.

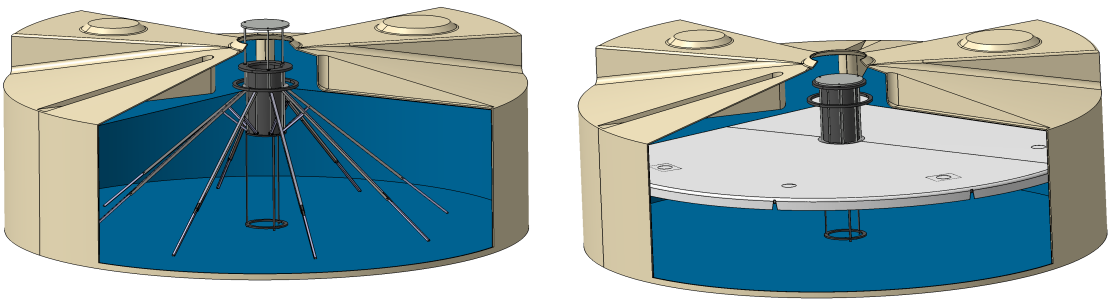

Figure 6.10 Opening process for the umbrella prototype [186].

In November 2013, an umbrella prototype was built at the Auger site but technical difficulties were found in the extendable system from the engineering point of view. The deployment in an empty tank was achieved but we could not go further. A new optimized design for the *umbrella* prototype is still under study [186].

Double liner prototype

In February 2013, a first prototype was built at the site. The configuration chosen was two different liners 40 and 80 cm high placed one on top of the other, with two different water volumes. The stabilization of the top liner (4 tons of water) over the bottom one was achieved by tense strings attached to the wall of the tank forming an hexagram to avoid the center occupied by the PMT. Regarding the PMTs configuration, only two were placed in the top and one in the bottom. A modification in the structure in the tank was needed to place the two PMTs in opposite places.

Although the prototype was built and some data were collected, the installation process was too complicated and the stabilization of the system was too weak, due to the weight of the top liner. The suggested improvement was to make a unique water volume, ensuring the stabilization of the system. The result of the improvement is the current design of the *double liner* prototype.

The renewed design includes the concept of a shared water volume. In a standard liner from Auger, an intermediate layer is introduced, providing optical but not hydraulic isolation. The accurate shape of the double bag ensures the correct position of the intermediate layer. The original liner is split horizontally in two parts of 40 and 80 cm, and sewed again between them and separated by the water transparent layer. A 10 inches PVC tube is inserted inside the top liner and it is glued to the top layer and the intermediate one. In the bottom of the tube

there is a window holding the bottom PMT (figure 6.11, right). The three PMTs of the top liner stay in their original locations.

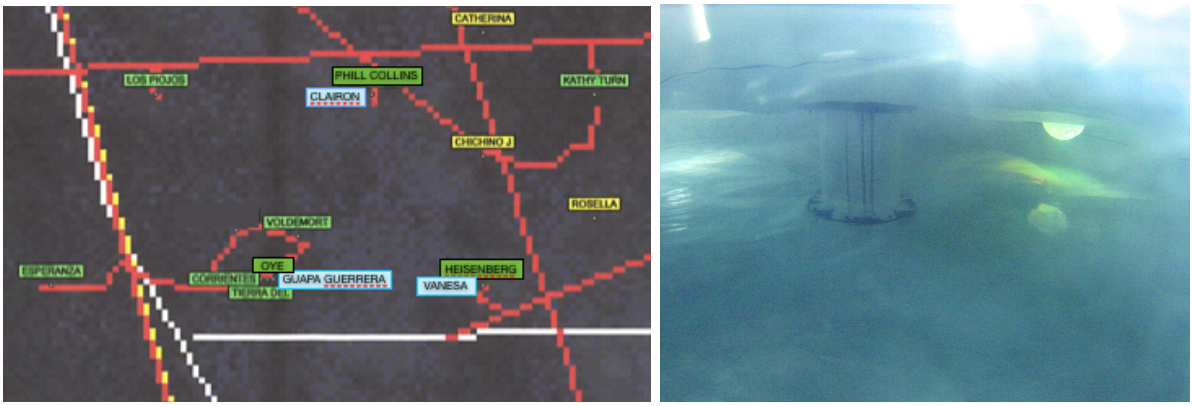

Figure 6.11 Left: maps with the locations of the constructed prototypes (blue tags) and the other Auger WCDs (green tags). Right: interior of the top liner of the first LSD prototype, with detail of the tube (in the centre) and a PMT window (bright hemisphere in the right) before the corresponding PMT were installed.

The first prototype with this design, named *Guapa Guerrera*, was built with success in February 2014 and installed in the field. The staff from the Pierre Auger Observatory has built and installed other two prototypes (*Vanesa* in June and *Clairon* in July) with the same design. The positions of the three prototypes are displayed in the left panel of figure 6.11. Their positions are arranged in a triangular configuration inside the Infill array, a region with a density of WCDs 4 times higher than the regular array (see section 1.4), separated 750 m from each other. They participate in about 100 physics events per day. All of the prototypes are in doublet (located away about 10 m) with a standard Auger SD station. *Guapa Guerrera* is paired with *Oye*, *Vanesa* is paired with *Heisenberg*, and *Clairon* is paired with *Phill Collins*. The purpose of this doublet configuration is the comparison of the signals. The data collected in the three prototypes is discussed in next section.

6.5 Data

The three prototypes have been taking data since their respective installations. In total there have been collected more than 8000 events with $E > 0.03$ EeV in which at least one LSD is affected. In about 300 of them the three prototypes participate in the event. The calibration and comparison with their doublets are presented. The muonic and electromagnetic LDFs for different LSDs is also shown.

Calibration

The peaks showing the most probable value of atmospheric muons appear now, independently, for the two different volumes. The histogram of charge of random signals for the PMT

observing the bottom volume of one of the installed prototypes is shown in figure 6.12 (left). The peak corresponds to the charge deposited by single muons that is roughly one VEM. This value is used for calibration.

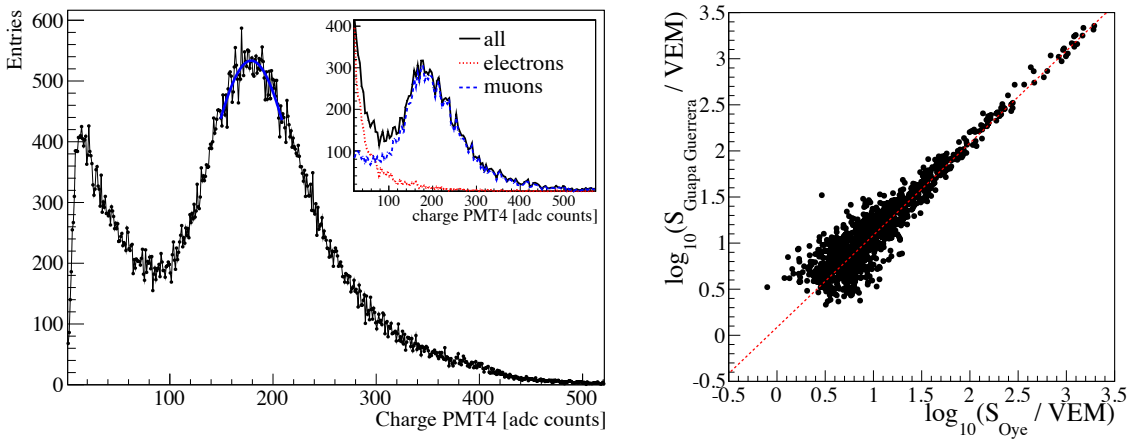

Figure 6.12 Left: muon peak from the charge distribution of the bottom PMT of the prototype data. In the inset, charge distribution from GEANT4 simulations of a LSD for all particles (solid line), muons (dashed) and for the background (pointed) are shown. Right: total signal in *Guapa Guerrera* prototype compared to its doublet *Oye*, located 10 m away. The red line is the fit of the points. As expected, there is a linear relation between the sum of the signals in the two volumes of the LSD and the signal in the standard WCD.

In the same figure (right) it is shown the total signal recorded in the LSD (by summing, after a preliminary calibration, top and bottom signals) versus the signal recorded in the same events by its doublet (*Oye*, in this case), located 10 m away. It is found, as expected, a linear correlation between the two signals over nearly three orders of magnitude. This shows that the LSD can also be used and can perform like a standard WCD.

Muonic and electromagnetic LDFs

An average LDF for the muonic and electromagnetic components can be constructed, as explained in section 6.3. The events were selected with a reconstructed energy between 0.03 and 1 EeV and a zenith angle lower than 45°. It is also requested that the energy deposit in the top part of the detector is larger than 400 MeV or 1.7 VEM. The zenith angle cut ensures that, even for those relatively low energy showers that develop higher in the atmosphere, the electromagnetic component is not completely absorbed before reaching ground. After normalizing the individual LDF of each event at 450 m it is possible to plot, as a function of distance to axis, the signal recorded by the LSD in all of those events. This average LDF for *Guapa Guerrera* and *Vanesa* is shown in figure 6.13. They are obtained by applying the transformation matrix (by the equation 6.7) to the top and bottom average LDFs. This result is preliminary, as nominal values of the matrix coefficients ($a = 0.6$ and $b = 0.4$) have been used. Nevertheless the quality of these results is very promising. In addition, as stated previously, the reconstruction of the average muonic and electromagnetic LDFs using different

LSD stations will allow to cross calibrate the individual matrices.

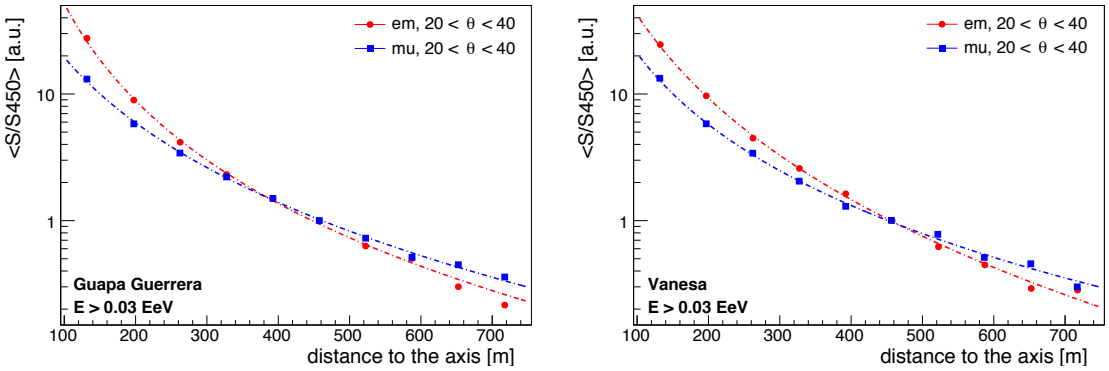

Figure 6.13 Average electromagnetic and muonic LDFs reconstructed applying the matrix with $a = 0.6$ and $b = 0.4$ to the top and bottom signals. Data collected with the LSD prototypes operating at Auger. Events selected with reconstructed energies $E > 0.03\,\text{EeV}$, zenith angle $20^\circ < \theta < 40^\circ$ and the prototype located at a distance of less than 700 m from the shower axis.

The comparison between them is done in figure 6.14. The muonic and electromagnetic average signals of each prototype are compared with the mean of the three. The dispersion remains under 20% between 200 and 600 m, with a higher dispersion at very short distances and further than 600 m.

6.6 Conclusions

The Layered Surface Detector (LSD) is a new concept of WCD that allows for the reconstruction of mass sensitive parameters for ultra-high energy cosmic rays with optimal resolution. The muon size of extensive air showers can be reconstructed with a precision better than 20% above 10 EeV, reaching 10% for energies above 70 EeV. This muon size can be combined with other observables already studied, like X_{max}, to improve the capabilities for composition of the ultra-high energy cosmic rays observatories.

Three prototypes of the LSD, constructed from a modification of Auger WCD, have shown excellent performances in agreement with expectations from MC simulations.

The LSD is a detector that should be considered for any upgrade of existing observatories of ultra-high energy cosmic rays or for the construction of new observatories, either with larger aperture than the current one or dedicated to the study of the second knee to ankle region, that is in the energy range from 0.1 EeV to 10 EeV.

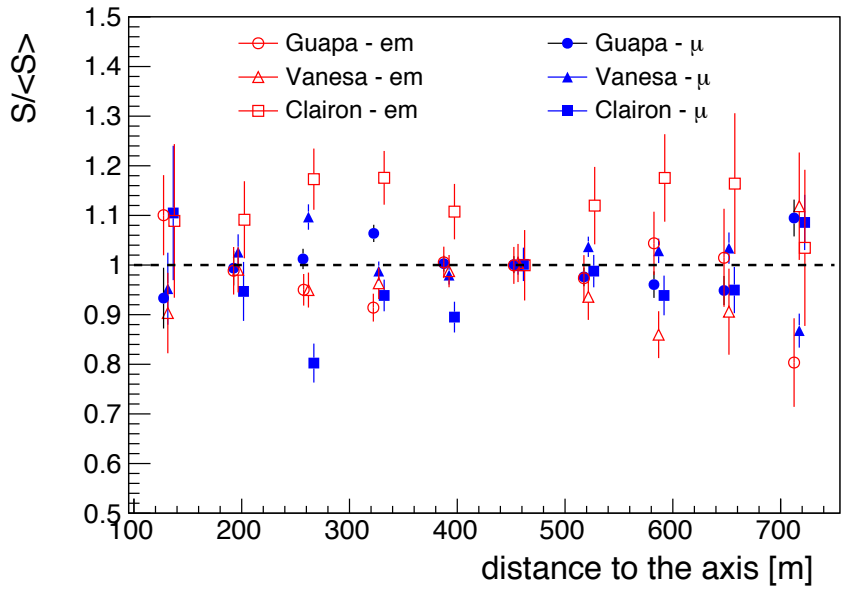

Figure 6.14 Comparison between the average electromagnetic and muonic LDFs reconstructed applying the matrix with $a = 0.6$ and $b = 0.4$ to the top and bottom signals. The calculated average for every prototype is compared with the mean of the three. Data collected with the LSD prototypes running at Auger. Events selected with reconstructed energies between 0.03 and 1 EeV, zenith angle below 45° and the prototype located at a distance of less than 700 m from the shower axis.

Conclusions

In this PhD thesis a brief review of the most important aspects of the physics of ultra-high energy cosmic rays has been exposed, including the general characteristics of the extensive air showers and the main results about the possible origin, propagation through the Universe, energy spectrum and composition of the primary particles.

The problem of the identification of the mass of the primary particle is a difficult task. Up to now, it relies on the observation of the atmospheric depth of maximum ($X_{\rm max}$), mostly based on measurements done by applying the fluorescence technique. The limited duty cycle is an issue, mostly due to the scarceness of these kind of particles. Other detection techniques and the possibility of extracting information about the mass composition with the number of muons in the shower are also being explored by the community and are discussed in this manuscript.

In this scenario, three different approaches to determine the composition of the ultra-high energy cosmic rays in the Pierre Auger Observatory are described, representing the original work of this PhD thesis.

In the first approach (chapter 4) a new analysis has been proposed. The magnetic deviation of the muons, that are dominant in more inclined showers, allows to explore several features of the shower in alternative ways. New parameters, angular distortion (α) and lateral extension (λ), have been investigated. The shape of the shower footprint at ground, measured by these two parameters, has been proven to be dependent on different characteristics of the extensive air shower. The parameter α is correlated with $X^{\mu}_{\rm max}$, and an estimator of $X^{\mu}_{\rm max}$ for a statistical analysis has been constructed, providing an alternative approach to composition analyses. This approach is complementary to others used to infer the muon production depth. Furthermore, α and λ are sensitive to the used hadronic interaction models and to other different assumptions on the cascade process, like the transverse momentum ($P_{\rm T}$) distribution of the muons. The study of these dependencies could lead to an improvement of the knowledge about the cascade development.

In the second approach (chapter 5) the technique of the detection of the extensive air showers based on their radio emissions has been explored. The access to the longitudinal profile of the extensive air shower is a key step to infer the mass of the primary particle. The study of the radio emission of the shower has been proposed as a full duty cycle alternative to the fluorescence technique. The processes of radio emission investigated in this thesis are two: the geosynchrotron emission and the Molecular Bremsstrahlung Radiation (MBR) emission. The former is a beamed emission and the latter is isotropic. The geosynchrotron emission has been proven to be detectable in the MHz frequency range, but limited in the application to infer

the mass in ultra-high energy cosmic rays, as it requires a large and dense sample of radio detectors to cover the large surface that it is needed. The MBR emission, being isotropic, is much more interesting to help in the identification of the mass of the primary particle. This topic has been attacked by the community from different points of view, some of them being revised in this work. Analytical calculations of the expected flux have been carried out, the intensity has been measured in accelerator experiments, and limits on this flux have been established in extensive air showers detection experiments at the Auger site (EASIER and MIDAS). A correct determination of the MBR flux will shed light on the feasibility of the use of this technique in the detection of ultra-high energy cosmic rays, as the detection experiences do not reveal, up to now, a significant flux that can confirm this emission as a prospective detection technique. The Giga Duck project, framed in the EASIER project, has been also presented, where the MBR emission is aimed to be detected with radio antennae installed in the Auger water Cherenkov detector. The principal objective of this ongoing project is to properly characterize the MBR emission.

In the third approach (chapter 6) a new kind of detector has been proposed. The Layered Surface Detector (LSD) is a new concept of water Cherenkov detector that allows the reconstruction of mass sensitive parameters for ultra-high energy cosmic rays. This detector allows for the separation of the two components of the extensive air shower: the electromagnetic and the muonic. Then, the muon size of extensive air showers can be reconstructed. The muon size can be combined with other observables already studied, like $X_{\max}$ or other age-related observables, obtained by different methods, to improve the capabilities to determine the composition of the ultra-high energy cosmic rays observatories. Three prototypes of the LSD have been constructed from a modification of Auger WCD, and they have been collecting data since their respective installations, showing excellent performances and proving that the technique is viable. The LSD is a detector that can be considered for any upgrade of existing observatories of ultra-high energy cosmic rays or for the construction of new observatories, either with larger aperture than the current ones or dedicated to the study of the second knee to ankle region, that is in the energy range from 0.1 EeV to 10 EeV.

The identification of the mass of the primary particle that enters the atmosphere with such a high energy has been proven to be difficult, but it was the aim of this work to show that possible steps in this direction are possible. According to the results shown in chapter 5, the technique of the radio detection still needs much more work to be proven as a viable one, as at present it has not shown clear indications of being an alternative to traditional techniques, like the fluorescence. On the contrary, the new method of analysis proposed in chapter 4 appears as a promising tool to be applied in any observatory of ultra-high energy cosmic rays, and the LSD prototype presented in chapter 6 represents a promising detector to be considered in any future ultra-high energy cosmic rays experiment.

Bibliography

[1] T. Wulf. "About the radiation of high penetration capacity contained in the atmosphere". In: *Physikalische Zeitschrift* 5 (1910), pp. 152–157.

[2] D. Pacini. "La radiazione penetrante alla superficie ed in seno alle acque". In: *Il Nuovo Cimento* 3.1 (1912), pp. 93–100.

[3] V. F. Hess. "Über Beobachtungen der durchdringenden Strahlung bei sieben Freiballonfahrten". In: *Z. Phys.* 13 (1912), p. 1084.

[4] A. A. Watson. "Extensive Air Showers and Ultra High Energy Cosmic Rays". In: *Summer School in Mexico*. 2002, pp. 1–50.

[5] H. Kragh. *Generaciones cuánticas*. Ediciones AKAL, Feb. 2007.

[6] S. H. Neddermeyer and C. D. Anderson. "Note on the nature of cosmic-ray particles. The nature of cosmic-ray particles". In: *Phys. Rev.* 51 (1937), pp. 884–886.

[7] P. V. Auger, R. Maze, and T. Grivet-Meyer. "Grandes gerbes cosmiques atmosphériques contenant des corpuscules ultra-pénétrantes". In: *Annalen der Physic* 32 (1938), p. 161.

[8] P. V. Auger, P Ehrenfest, et al. "Extensive Cosmic-Ray Showers". In: *Rev. Mod. Phys.* 11 (July 1939), pp. 288–291.

[9] K. H. Kampert and A. A. Watson. "Extensive air showers and ultra high-energy cosmic rays: a historical review". In: *The European Physical Journal H* 37.3 (July 2012), pp. 359–412.

[10] W. Bothe. "Zur Vereinfachung von Koinzidenzzählungen". In: *Zeitschrift für Physik* 59.1-2 (1930), pp. 1–5.

[11] H. Geiger and W. Müller. "Elektronenzählrohr zur Messung schwächster Aktivitäten". In: *Naturwissenschaften* 16.31 (Aug. 1928), pp. 617–618.

[12] E. Rutherford and H. Geiger. "An Electrical Method of Counting the Number of α-Particles from Radio-Active Substances". In: *Proceedings of the Royal Society A: Mathematical, Physical and Engineering Sciences* 81.546 (Aug. 1908), pp. 141–161.

[13] R. W. Williams. "The Structure of the Large Cosmic-Ray Air Showers". In: *Physical Review* 74.11 (Dec. 1948), pp. 1689–1706.

[14] P. Bassi, G. Clark, and B. Rossi. "Distribution of Arrival Times of Air Shower Particles". In: *Physical Review* 92.2 (Oct. 1953), pp. 441–451.

[15] N. A. Porter, T. E. Cranshaw, et al. "Observations on extensive air showers VII. The lateral distribution of energy in the electron-photon component". In: *Philosophical Magazine* 3.32 (Aug. 1958), pp. 826–830.

[16] P. M. S. Blackett. "A possible contribution to the night sky from the Cerenkov radiation emitted by cosmic rays". In: *Emission Spectra of the Night Sky and Aurorae*. 1948.

[17] W. Galbraith and J. V. Jelley. "Light Pulses from the Night Sky associated with Cosmic Rays". In: *Nature* 171.4347 (Feb. 1953), pp. 349–350.

[18] J. Jelley. *Cerenkov Radiation and Its Applications*. Pergamon Press, 1958.

[19] J. V. Jelley, J. H. Fruin, et al. "Radio Pulses from Extensive Cosmic-Ray Air Showers". In: *Nature* 205.4 (Jan. 1965), pp. 327–328.

[20] G. Clark, I. Escobar, et al. In: *Interamerican Seminar on Cosmic Rays*. La Paz, Bolivia, 1962.

[21] A. Chudakov. In: *Interamerican Seminar on Cosmic Rays*. La Paz, Bolivia, 1962.

[22] K. Greisen. "Highlights in air shower studies". In: *International Cosmic Ray Conference*. 1965, pp. 609–615.

[23] A. Letessier-Selvon and T. Stanev. "Ultrahigh energy cosmic rays". In: *Reviews of Modern Physics* 83.3 (July 2011), pp. 907–942.

[24] A. Ferrer Soria and E. Ros Martínez. *Física de partículas y de astropartículas*. Ed. by M. Simón. Valencia: Universitat de València, 2005.

[25] M. Risse. "Properties of extensive air showers". In: *Eur.Phys.J.Plus* B35 (2004), pp. 1787–1798.

[26] B. Rossi. *High Energy Particles*. New York: Prentice-Hall, 1952.

[27] K. Nakamura and Particle Data Group. "Review of Particle Physics". In: *Journal of Physics G: Nuclear and Particle Physics* 37.7A (July 2010), p. 075021.

[28] J. Matthews. "A Heitler model of extensive air showers". In: *Astroparticle Physics* 22.5-6 (Jan. 2005), pp. 387–397.

[29] W. Heitler. *The quantum theory of radiation*. The international series of monographs on physics. Oxford: Clarendon Press, 1936.

[30] E.-J. Ahn, R. Engel, et al. "Cosmic ray interaction event generator SIBYLL 2.1". In: *Physical Review D* 80.9 (Nov. 2009), 094003 EP –.

[31] S. Ostapchenko. "QGSJET-II: towards reliable description of very high energy hadronic interactions". In: *Nuclear Physics B - Proceedings Supplements* 151.1 (2006), pp. 143–146.

[32] S. Ostapchenko. "QGSJET-II: results for extensive air showers". In: *Nuclear Physics B - Proceedings Supplements* 151.1 (2006), pp. 147–150.

[33] S. Ostapchenko. "QGSJET-II: physics, recent improvements, and results for air showers". In: *EPJ Web of Conferences* 52 (June 2013), p. 02001.

[34] T. Pierog, I. Karpenko, et al. "EPOS LHC : test of collective hadronization with LHC data". In: *Eur.Phys.J.Plus* hep-ph (2013).

[35] S. Sciutto. *AIRES. A system for air shower simulations*. Tech. rep. La Plata, Argentina: Universidad de La Plata, July 2002.

[36] D. Heck, G Schatz, et al. *CORSIKA: A Monte Carlo code to simulate extensive air showers*. FZKA-6019. 1998.

[37] A. Ferrari, P. R. Sala, et al. *FLUKA: A multi-particle transport code (Program version 2005)*. CERN-2005-010, SLAC-R-773, INFN-TC-05-11. 2005.

[38] J. Allison, K. Amako, et al. "Geant4 developments and applications". In: *Nuclear Science, IEEE Transactions on* 53.1 (Feb. 2006), pp. 270–278.

[39] S. Agostinelli, J. Allison, et al. "Geant4—a simulation toolkit". In: *Nuclear Instruments and Methods in Physics Research A* 506.3 (2003), pp. 250–303.

[40] A. M. Hillas. *Cosmic Rays*. The Commonwealth and International Library: Selected Readings in Physics. Elsevier, Jan. 1972.

[41] P. Billoir for the Pierre Auger Collaboration. "The Cherenkov Surface Detector of the Pierre Auger Observatory". In: *International Workshop on Ring Imaging Cherenkov Detectors*. Hayama, Kanagawa, Japan, Feb. 2014, pp. 1–13.

[42] K. Kamata and J. Nishimura. "The Lateral and the Angular Structure Functions of Electron Showers". In: *Progress of Theoretical Physics Supplement* 6 (Feb. 1958), pp. 93–155.

[43] D. E. Groom, N. V. Mokhov, and S. I. Striganov. "Muon stopping power and range tables 10-MeV to 100-TeV". In: *Atom.Data Nucl.Data Tabl.* 78.2 (2001), pp. 183–356.

[44] Pierre Auger Collaboration. "Properties and performance of the prototype instrument for the Pierre Auger Observatory". In: *Nuclear Instruments and Methods in Physics Research A* A523.1-2 (2004), pp. 50–95.

[45] S. Westerhoff. "HAWC: A next-generation all-sky gamma-ray telescope". In: *Adv.Space Res.* 53 (2014), pp. 1492–1498.

[46] S Yoshida, N Hayashida, et al. "The cosmic ray energy spectrum above $3x10^{18}$ eV measured by the Akeno Giant Air Shower Array". In: *Astroparticle Physics* 3.2 (Mar. 1995), pp. 105–123.

[47] T. Nonaka, T. Abu-Zayyad, et al. "The present status of the Telescope Array experiment". In: *Nuclear Physics B - Proceedings Supplements* 190.C (May 2009), pp. 26–31.

[48] S. Cui, Y. Liu, et al. "Simulation on gamma ray astronomy research with LHAASO-KM2A". In: *Astroparticle Physics* 54.0 (2014), pp. 86–92.

[49] P. A. Cherenkov. "Visible Emission of Clean Liquids by Action of γ Radiation". In: *Doklady Akad. Nauk SSSR* 2 (1934), p. 451.

[50] S. F. Berezhnev, D Besson, et al. "The Tunka-133 EAS Cherenkov light array: Status of 2011". In: *Nuclear Instruments and Methods in Physics Research Section A: Accelerators, Spectrometers, Detectors and Associated Equipment* 692.0 (Nov. 2012), pp. 98–105.

[51] J. A. Hinton for the HESS Collaboration. "The status of the HESS project". In: *New Astronomy Reviews* 48.5-6 (Apr. 2004), pp. 331–337.

[52] T. C. Weekes, H. Badran, et al. "VERITAS: the Very Energetic Radiation Imaging Telescope Array System". In: *Astroparticle Physics* 17.2 (2002), pp. 221–243.

[53] D. Ferenc. "The MAGIC gamma-ray observatory". In: *Nuclear Instruments and Methods in Physics Research Section A: Accelerators, Spectrometers, Detectors and Associated Equipment* 553.1-2 (Nov. 2005), pp. 274–281.

[54] CTA Consortium. "Design concepts for the Cherenkov Telescope Array CTA: An advanced facility for ground-based high-energy gamma-ray astronomy". In: *Eur.Phys.J.Plus* 32.3 (2011), pp. 193–316.

[55] F. Halzen. "Neutrino Astrophysics Experiments beneath the Sea and Ice". In: *Science* 315.5808 (Jan. 2007), pp. 66–68.

[56] ANTARES Collaboration. *A deep sea telescope for high-energy neutrinos*. Tech. rep. 1999.

[57] F Arqueros, F. Blanco, and J. Rosado. "Analysis of the fluorescence emission from atmospheric nitrogen by electron excitation, and its application to fluorescence telescopes". In: *New Journal of Physics* 11.6 (June 2009), p. 065011.

[58] Y Asaoka. "All-sky survey high resolution air-shower detector (Ashra)". In: *Nuclear Science Symposium Conference Record, 2003 IEEE IS* -. 2003, 144–146 Vol.1.

[59] R. M. Baltrusaitis, R Cady, et al. "The Utah Fly's Eye detector". In: *Nuclear Instruments and Methods in Physics Research A* 240.2 (1985), pp. 410–428.

[60] J. H. Boyer, B. C. Knapp, et al. "FADC-based DAQ for HiRes Fly's Eye". In: *Nuclear Instruments and Methods in Physics Research A* 482.1–2 (2002), pp. 457–474.

[61] Y. Takahashi and JEM-EUSO Collaboration. "The JEM-EUSO mission". In: *New Journal of Physics* 11.6 (June 2009), p. 065009.

[62] D Ardouin, A. Bellètoile, et al. "Radio-Detection Signature of High Energy Cosmic Rays by the CODALEMA Experiment". In: *Nuclear Instruments and Methods in Physics Research A* A555.1-2 (2005), pp. 148–163.

[63] H. Falcke, W. D. Apel et al. "Detection and imaging of atmospheric radio flashes from cosmic ray air showers". In: *Nature* 435.7040 (2005), pp. 313–316.

[64] J. L. Kelley for the Pierre Auger Collaboration. "AERA: the Auger Engineering Radio Array". In: *International Cosmic Ray Conference*. Beijing, 2011, pp. 1–4.

[65] I Kravchenko, G. M. Frichter, et al. "Performance and simulation of the RICE detector". In: *Astroparticle Physics* 19.1 (Apr. 2003), pp. 15–36.

[66] P. Gorham and ANITA Collaboration. "The ANITA Cosmogenic Neutrino Experiment". In: *International Journal of Modern Physics A* 21.supp01 (July 2006), pp. 158–162.

[67] L. Gerhardt, S. Klein, et al. "A prototype station for ARIANNA: a detector for cosmic neutrinos". In: *Nucl.Instrum.Meth.* A624 (2010), pp. 85–91.

[68] P. Allison, J Auffenberg, et al. "Design and initial performance of the Askaryan Radio Array prototype EeV neutrino detector at the South Pole". In: *Astroparticle Physics* 35.7 (Feb. 2012), pp. 457–477.

[69] S Gillessen, F Eisenhauer, et al. "MONITORING STELLAR ORBITS AROUND THE MASSIVE BLACK HOLE IN THE GALACTIC CENTER". In: *The Astrophysical Journal* 692.2 (Feb. 2009), pp. 1075–1109.

[70] Pierre Auger Collaboration. "Trigger and aperture of the surface detector array of the Pierre Auger Observatory". In: *Nuclear Instruments and Methods in Physics Research A* A613.1 (2010), pp. 29–39.

[71] Pierre Auger Collaboration. "The Fluorescence Detector of the Pierre Auger Observatory". In: *Nuclear Instruments and Methods in Physics Research A* A620.2-3 (2010), pp. 227–251.

[72] A. Zepeda. "Ultra High Energy Cosmic Rays and the Pierre Auger Project". In: *Third Latin American Symposium on High Energy Physics*. 2000, p. 040.

[73] T. K. Gaisser and A. M. Hillas. "Reliability of the method of constant intensity cuts for reconstructing the average development of vertical showers". In: *International Cosmic Ray Conference*. 1977, pp. 1–5.

[74] M. Tueros for the Pierre Auger Collaboration. "Estimate of the non-calorimetric energy of showers observed with the fluores- cence and surface detectors of the Pierre Auger Observatory". In: *International Cosmic Ray Conference*. Rio de Janeiro, 2013, pp. 1–4.

[75] Pierre Auger Collaboration. "Techniques for measuring aerosol attenuation using the Central Laser Facility at the Pierre Auger Observatory". In: *Journal of Instrumentation* 8.04 (Apr. 2013), P04009.

[76] A. Ferrer Soria. *Física nuclear y de partículas*. Ed. by M. Simón. Valencia: Universitat de València, 2003.

[77] X. Bertou, P. S. Allison, et al. "Calibration of the surface array of the Pierre Auger Observatory". In: *Nuclear Instruments and Methods in Physics Research A* A568 (2006), pp. 839–846.

[78] P. L. Ghia for the Pierre Auger Collaboration. "Testing the surface detector simulation for the Pierre Auger Observatory". In: *International Cosmic Ray Conference*. 2007.

[79] D Newton, J. Knapp, and A. Watson. "The optimum distance at which to determine the size of a giant air shower". In: *Astroparticle Physics* 26.6 (2006), pp. 414–419.

[80] Pierre Auger Collaboration. "Operations of and Future Plans for the Pierre Auger Observatory". In: *Eur.Phys.J.Plus* astro-ph.IM (2009).

[81] A. Etchegoyen for the Pierre Auger Collaboration. "AMIGA, Auger Muons and Infill for the Ground Array". In: *International Cosmic Ray Conference*. Merida, Yucatan, Mexico, 2007.

[82] P. W. Gorham, N. G. Lehtinen, et al. "Observations of microwave continuum emission from air shower plasmas". In: *Physical Review D* 78.3 (Aug. 2008), 032007 EP –.

[83] M. Monasor, I Alekotte, et al. "The MIDAS experiment: A prototype for the microwave emission of Ultra-High Energy Cosmic Rays". In: *Nuclear Physics B - Proceedings Supplements* 215.1 (2011), pp. 63–65.

[84] J. Álvarez-Muñiz, E. Amaral Soares, et al. "The MIDAS telescope for microwave detection of ultra-high energy cosmic rays". In: *Nuclear Instruments and Methods in Physics Research Section A: Accelerators, Spectrometers, Detectors and Associated Equipment* 719.0 (Aug. 2013), pp. 70–80.

[85] W Baade and F Zwicky. "Remarks on Super-Novae and Cosmic Rays". In: *Phys. Rev.* 46.1 (July 1934), pp. 76–77.

[86] V. I. L. Ginzburg and S. I. Syrovatskii. *The Origin of Cosmic Rays*. A Pergamon Press Book. Macmillan, 1964.

[87] M. E. Bertaina. "Cosmic rays from the knee to the ankle". In: *Comptes Rendus Physique* 15.4 (Apr. 2014), pp. 300–308.

[88] A. D. Erlykin and A. W. Wolfendale. "Properties of cosmic ray interactions at PeV energies". In: *Astroparticle Physics* 18.2 (Oct. 2002), pp. 151–164.

[89] K. A. Olive and Particle Data Group. "Review of Particle Physics". In: *Chin.Phys.* C38 (2014), p. 090001.

[90] D. R. Bergman and J. W. Belz. "Cosmic rays: the Second Knee and beyond". In: *Journal of Physics G: Nuclear and Particle Physics* 34.10 (2007), R359.

[91] O. Deligny. "Cosmic rays around 10^{18} eV: Implications of contemporary measurements on the origin of the ankle feature". In: *Comptes Rendus Physique* 15.4 (Apr. 2014), pp. 367–375.

[92] T Antoni, W. D. Apel, et al. "KASCADE measurements of energy spectra for elemental groups of cosmic rays: Results and open problems". In: *Astroparticle Physics* 24.1–2 (2005), pp. 1–25.

[93] W. D. Apel, J. C. Arteaga, et al. "The KASCADE-Grande experiment". In: *Nuclear Instruments and Methods in Physics Research A* 620.2–3 (2010), pp. 202–216.

[94] R Abbasi, Y Abdou, et al. "IceTop: The surface component of IceCube". In: *Nuclear Instruments and Methods in Physics Research Section A: Accelerators, Spectrometers, Detectors and Associated Equipment* 700.0 (Feb. 2013), pp. 188–220.

[95] N Hayashida, K Honda, et al. "Observation of a Very Energetic Cosmic Ray Well Beyond the Predicted 2.7 K Cutoff in the Primary Energy Spectrum". In: *Physical Review Letters* 73.26 (Dec. 1994), pp. 3491–3494.

[96] M Takeda, N Hayashida, et al. "Extension of the Cosmic-Ray Energy Spectrum beyond the Predicted Greisen-Zatsepin-Kuz'min Cutoff". In: *Physical Review Letters* 81.6 (Aug. 1998), pp. 1163–1166.

[97] D. J. Bird, S. C. Corbato, et al. "The Cosmic ray energy spectrum observed by the Fly's Eye". In: *Astrophys.J.* 424 (1994), pp. 491–502.

[98] R. U. Abbasi, T Abu-Zayyad, et al. "First Observation of the Greisen-Zatsepin-Kuzmin Suppression". In: *Physical Review Letters* 100.10 (Mar. 2008), 101101 EP –.

[99] Pierre Auger Collaboration. "Observation of the suppression of the flux of cosmic rays above $4x10^{19}$eV". In: *Physical Review Letters* 101.6 (2008), p. 061101.

[100] A. A. Penzias and R. W. Wilson. "A Measurement of excess antenna temperature at 4080-Mc/s". In: *Astrophys.J.* 142 (1965), pp. 419–421.

[101] K. Greisen. "End to the Cosmic-Ray Spectrum?" In: *Physical Review Letters* 16 (Apr. 1966), pp. 748–750.

[102] G. T. Zatsepin and V. A. Kuzmin. "Upper limit of the spectrum of cosmic rays". In: *JETP Lett.* 4 (1966), pp. 78–80.

[103] K. Kotera and A. V. Olinto. "The Astrophysics of Ultrahigh-Energy Cosmic Rays". In: *Annual Review of Astronomy and Astrophysics* 49.1 (Sept. 2011), pp. 119–153.

[104] D. Harari. "The flux suppression at the highest energies". In: *Comptes Rendus Physique* 15.4 (Apr. 2014), pp. 376–383.

[105] A. M. Hillas. "The Origin of Ultrahigh-Energy Cosmic Rays". In: *Ann.Rev.Astron.Astrophys.* 22.1 (1984), pp. 425–444.

[106] F. H. Zas and E. "Neutrino Fluxes from Active Galaxies: A Model-Independent Estimate". In: *The Astrophysical Journal* 488.2 (1997), p. 669.

[107] E. Waxman. "Cosmological Gamma-Ray Bursts and the Highest Energy Cosmic Rays". In: *Physical Review Letters* 75.3 (July 1995), pp. 386–389.

[108] J Abraham, P. Abreu, et al. "Measurement of the Depth of Maximum of Extensive Air Showers above 10^{18} eV". In: *Physical Review Letters* 104.9 (2010), p. 091101.

[109] P. Blasi. "Origin of very high- and ultra-high-energy cosmic rays". In: *Comptes Rendus Physique* 15.4 (Apr. 2014), pp. 329–338.

[110] A Vilenkin and E. P. S. Shellard. *Cosmic Strings and Other Topological Defects.* Cambridge University Press, July 2000.

[111] G. B. Gelmini, O. E. Kalashev, and D. V. Semikoz. "GZK photons as ultra-high-energy cosmic rays". In: *Journal of Experimental and Theoretical Physics* 106.6 (July 2008), pp. 1061–1082.

[112] J. N. Bahcall and E. Waxman. "Has the GZK suppression been discovered?" In: *Physics Letters B* 556.1-2 (Mar. 2003), pp. 1–6.

[113] V. Berezinsky, A. Gazizov, and S. Grigorieva. "On astrophysical solution to ultrahigh energy cosmic rays". In: *Physical Review D* 74.4 (Aug. 2006), 043005 EP –.

[114] R Aloisio, V Berezinsky, and A Gazizov. "Transition from galactic to extragalactic cosmic rays". In: *Astroparticle Physics* 39-40 (Dec. 2012), pp. 129–143.

[115] D Allard, E. Parizot, and A. V. Olinto. "On the transition from galactic to extragalactic cosmic-rays: Spectral and composition features from two opposite scenarios". In: *Astroparticle Physics* 27.1 (Feb. 2007), pp. 61–75.

[116] R Aloisio, V Berezinsky, and A Gazizov. "Ultra High Energy Cosmic Rays: The disappointing model". In: *Astroparticle Physics* 34 (2011), pp. 620–626.

[117] Pierre Auger Collaboration. "The exposure of the hybrid detector of the Pierre Auger Observatory". In: *Astropart.Phys.* 34.6 (2011), pp. 368–381.

[118] Pierre Auger Collaboration. "Measurement of the energy spectrum of cosmic rays above 10^{18} eV using the Pierre Auger Observatory". In: *Physics Letters B* B685.4-5 (2010), pp. 239–246.

[119] A. Schulz for the Pierre Auger Collaboration. "The measurement of the energy spectrum of cosmic rays above $3x10^{17}$eV with the Pierre Auger Observatory". In: *International Cosmic Ray Conference*. 2013, pp. 1–4.

[120] D. Harari. "Ultra-high energy cosmic rays". In: *Physics of the Dark Universe* 4.0 (Sept. 2014), pp. 23–30.

[121] Pierre Auger Collaboration. "Correlation of the highest-energy cosmic rays with nearby extragalactic objects". In: *Science* 318.5852 (Nov. 2007), pp. 938–943.

[122] Pierre Auger Collaboration. "Correlation of the highest-energy cosmic rays with the positions of nearby active galactic nuclei". In: 29 (Mar. 2008), pp. 188–204.

[123] M. P. Véron-Cetty and P Véron. "A catalogue of quasars and active nuclei: 12th edition". In: *Astronomy & Astrophysics* 455.2 (2006), pp. 773–777.

[124] Pierre Auger Collaboration. "Update on the correlation of the highest energy cosmic rays with nearby extragalactic matter". In: *Astroparticle Physics* 34.5 (Dec. 2010), pp. 314–326.

[125] Pierre Auger Collaboration. "Search for first harmonic modulation in the right ascension distribution of cosmic rays detected at the Pierre Auger Observatory". In: *Astroparticle Physics* 34.8 (2011), pp. 627–639.

[126] I. Sidelnik for the Pierre Auger Collaboration. "Measurement of the first harmonic modulation in the right ascension distribu- tion of cosmic rays detected at the Pierre Auger Observatory: towards the de- tection of dipolar anisotropies over a wide energy range". In: *International Cosmic Ray Conference*. 2013, pp. 1–4.

[127] R. M. de Almeida for the Pierre Auger Collaboration. "Constraints on the origin of cosmic rays from large scale anisotropy searches in data of the Pierre Auger Observatory". In: *International Cosmic Ray Conference*. 2013, pp. 1–4.

[128] R. W. Ellsworth, T. K. Gaisser, et al. "Ultrahigh-energy cross section from study of longitudinal development of air showers". In: *Physical Review D* 26.1 (July 1982), pp. 336–339.

[129] R. M. Baltrusaitis, G. L. Cassiday, et al. "Total Proton-Proton Cross Section at $s^{1/2}$= 30 TeV". In: *Physical Review Letters* 52.16 (Apr. 1984), pp. 1380–1383.

[130] Pierre Auger Collaboration. "Measurement of the proton-air cross-section at $\sqrt{s} = 57\,\mathrm{TeV}$ with the Pierre Auger Observatory". In: *Physical Review Letters* 109.6 (2012), p. 062002.

[131] R. J. Glauber. "Cross Sections in Deuterium at High Energies". In: *Physical Review* 100.1 (Oct. 1955), pp. 242–248.

[132] R. J. Glauber and G. Matthiae. "High-energy scattering of protons by nuclei". In: *Nuclear Physics B* 21.2 (Jan. 1970), pp. 135–157.

[133] Pierre Auger Collaboration. "The muon content of UHECR air showers observed by the Pierre Auger Observatory". In: Submitted (Jan. 2014), pp. 1–5.

[134] Pierre Auger Collaboration. "A Search for Point Sources of EeV Neutrons". In: *Astrophys.J.* 760.2 (2012), p. 148.

[135] Pierre Auger Collaboration. "Depth of Maximum of Air-Shower Profiles at the Pierre Auger Observatory: Composition Implications". In: *Physical Review D* Submitted (Sept. 2014), pp. 1–13.

[136] M. Roth for the Pierre Auger Collaboration. "Measurement of the UHECR energy spectrum using data from the Surface Detector of the Pierre Auger Observatory". In: *International Cosmic Ray Conference*. 2007, pp. 1–4.

[137] R. A. Fisher. "The use of multiple measurements in taxonomic problems". In: *Annals of Eugenics* 7.2 (Sept. 1936), pp. 179–188.

[138] Pierre Auger Collaboration. "Muons in air showers at the Pierre Auger Observatory: Mean number in highly inclined events". In: *Physical Review D* Submitted (Aug. 2014), pp. 1–12.

[139] B. Kégl for the Pierre Auger Collaboration. "Measurement of the muon signal using the temporal and spectral structure of the signals in surface detectors of the Pierre Auger Observatory". In: *International Cosmic Ray Conference*. 2013, pp. 1–4.

[140] Pierre Auger Collaboration. "Depth of Maximum of Air-Shower Profiles at the Pierre Auger Observatory: Measurements at Energies above $10^{17.8}$eV". In: *Physical Review D* Submitted (Sept. 2014), pp. 1–25.

[141] D. J. Bird, S. C. Corbato, et al. "Evidence for correlated changes in the spectrum and composition of cosmic rays at extremely high energies". In: *Physical Review Letters* 71.21 (Nov. 1993), pp. 3401–3404.

[142] High Resolution Fly's Eye Collaboration. "A Study of the Composition of Ultra-High-Energy Cosmic Rays Using the High-Resolution Fly's Eye". In: *The Astrophysical Journal* 622.2 (2005), p. 910.

[143] Pierre Auger Collaboration. "Interpretation of the depths of maximum of extensive air showers measured by the Pierre Auger Observatory". In: *Journal of Cosmology and Astroparticle Physics* 02.0 (Feb. 2013), pp. 026–026.

[144] A Aab, P. Abreu, et al. "Muons in air showers at the Pierre Auger Observatory: Measurement of atmospheric production depth". In: *Physical Review D* 90.1 (July 2014), p. 012012.

[145] M. Risse and P. Homola. "Search For Ultra-High Energy Photons Using Air Showers". In: *Modern Physics Letters A* 22.11 (Apr. 2007), pp. 749–766.

[146] Pierre Auger Collaboration. "Upper limit on the cosmic-ray photon flux above 10^{19} eV using the surface detector of the Pierre Auger Observatory". In: *Astroparticle Physics* 29.4 (2008), pp. 243–256.

[147] Pierre Auger Collaboration. "An upper limit to the photon fraction in cosmic rays above 10^{19} eV from the Pierre Auger Observatory". In: *Astroparticle Physics* 27.2-3 (2007), pp. 155–168.

[148] Pierre Auger Collaboration. "Upper limit on the cosmic-ray photon fraction at EeV energies from the Pierre Auger Observatory". In: *Astropart.Phys.* 31.6 (2009), pp. 399–406.

[149] M. Settimo for the Pierre Auger Collaboration. "Search for ultra-High Energy Photons with the Pierre Auger Observatory". In: *Proceeding of Science*. Paris, 2013, pp. 1–10.

[150] Pierre Auger Collaboration. "A search for point sources of EeV photons". In: *The Astrophysical Journal* 789.2 (July 2014), p. 160.

[151] Pierre Auger Collaboration. "Search for ultrahigh energy neutrinos in highly inclined events at the Pierre Auger Observatory". In: *Physical Review D* 84.12 (Dec. 2011), p. 122005.

[152] Pierre Auger Collaboration. "Upper limit on the diffuse flux of UHE tau neutrinos from the Pierre Auger Observatory". In: *Physical Review Letters* 100.21 (2008), p. 211101.

[153] Pierre Auger Collaboration. "Limit on the diffuse flux of ultra-high energy tau neutrinos with the surface detector of the Pierre Auger Observatory". In: *Physical Review D* D79.10 (2009), p. 102001.

[154] Pierre Auger Collaboration. "Ultrahigh Energy Neutrinos at the Pierre Auger Observatory". In: *Advances in High Energy Physics* 2013.4-5 (2013), pp. 708680–18.

[155] Pierre Auger Collaboration. "Search for point-like sources of ultra-high energy neutrinos at the Pierre Auger Observatory and improved limit on the diffuse flux of tau neutrinos". In: *Astrophys.J.* L4.1 (2012), p. 755.

[156] S. G. Ott, F Eisenhauer, et al. "Monitoring Stellar Orbits Around the Massive Black Hole in the Galactic Center". In: *The Astrophysical Journal* 692.2 (2009), p. 1075.

[157] Pierre Auger Collaboration. "A Targeted Search for Point Sources of EeV Neutrons". In: *Astrophys.J.* L34.2 (2014), p. 789.

[158] P. Billoir. "Curvature and magnetic distortion of horizontal showers: comparison between simulations and real data". In: *Auger Collaboration Meeting*. Malargüe, Mar. 2006.

[159] P. Hansen and J. Álvarez-Muñiz. "Magnetic effects in very inclined showers". In: *Auger GAP Note* 2013.009 (Mar. 2013), pp. 1–14.

[160] P. Billoir, O. Deligny, and A. Letessier-Selvon. "A Complete Procedure for the Reconstruction of Inclined Air Showers". In: *Auger GAP Note* 2003-003 (Mar. 2003), pp. 1–13.

[161] M. S. Nikulin. *Kolmogorov-Smirnov test*. URL: `http://www.encyclopediaofmath.org/index.php?title=Kolmogorov-Smirnov_test&oldid=17054`.

[162] G. A. Askariyan. "Excess Negative Charge of an Electron-Photon Shower And Its Coherent Radio Emission". In: *Soviet Physics - JETP* 14 (1962), pp. 441–443.

[163] T. C. Weekes. "Radio pulses from cosmic ray air showers". In: *Eur.Phys.J.Plus* 579 (2001), pp. 3–13.

[164] F. D. Kahn and I Lerche. "Radiation from Cosmic Ray Air Showers". In: *Proceedings of the Royal Society A: Mathematical, Physical and Engineering Sciences* 289.1417 (Jan. 1966), pp. 206–213.

[165] Pierre Auger Collaboration. "Probing the radio emission from air showers with polarization measurements". In: *Physical Review D* D89.5 (2014), p. 052002.

[166] D. Saltzberg, P. Gorham, et al. "Observation of the Askaryan effect: Coherent microwave Cherenkov emission from charge asymmetry in high-energy particle cascades". In: *Phys.Rev.Lett.* 86 (2001), pp. 2802–2805.

[167] S Gillessen, F Eisenhauer, et al. "Monitoring Stellar Orbits Around the Massive Black Hole in the Galactic Center". In: *The Astrophysical Journal* 692.2 (Feb. 2009), pp. 1075–16.

[168] MAYBE Collaboration. "The Microwave Air Yield Beam Experiment (MAYBE): Measurement of GHz radiation for Ultra-High Energy Cosmic Rays detection". In: *International Cosmic Ray Conference*. Beijing, 2011.

[169] J. Álvarez-Muñiz, M. Blanco, et al. "AMY (Air Microwave Yield) Laboratory Measurement of the GHz Emission from Air Showers". In: *International Cosmic Ray Conference*. Rio de Janeiro, July 2013.

[170] I. Al Samarai, J Aublin, et al. “An estimate of the spectral intensity expected from the molecular Bremsstrahlung radiation in extensive air showers”. In: *ARENA*. Oct. 2014, pp. 1–4.

[171] T. Huege, M. Ludwig, and C. W. James. “Simulating radio emission from air showers with CoREAS”. In: *Eur.Phys.J.Plus* astro-ph.HE (2013).

[172] I. Al Samarai for the Pierre Auger Collaboration. “Radio detection of Cosmic Rays in the GHz band at the Pierre Auger Observatory”. In: *ARENA*. Oct. 2014, pp. 1–6.

[173] C. Berat for the Pierre Auger Collaboration. “Radio detection of extensive air showers at the Pierre Auger Observatory”. In: *Pisa Meeting on Advanced Detectors*. 2012, pp. 471–474.

[174] M. Blanco, A. Letessier-Selvon, and I. C. Maris. “The impact of removing one low gain channel of the surface detector”. In: *Auger GAP Note* 2012-88 (2012).

[175] CODALEMA Collaboration and D. Charrier. “Antenna development for astroparticle and radioastronomy experiments”. In: *Nuclear Instruments and Methods in Physics Research A* A662 (2012), S142–S145.

[176] J. Álvarez-Muñiz, M. Blanco, et al. “The Air Microwave Yield (AMY) experiment - A laboratory measurement of the microwave emission from extensive air showers”. In: *The European Physical Society Conference on High Energy Physics*. Stockholm, Sweden, July 2013.

[177] V. Verzi. “AMY Air Microwave Yield”. In: *CSN V*. Napoli, Apr. 2014, pp. 1–45.

[178] F. C. TBD. “http://www.fpvcenter.com/900-MHz/1-2-ghz-helix-antenna”. In: ().

[179] J Aublin, P. Billoir, et al. “Electromagnetic compatibility of the EASIER MHz antennas and the Auger surface detectors”. In: *Auger GAP Note* 2011.80 (2011).

[180] Anritsu. “http://www.anritsu.com/en-US/Products-Solutions/Products/MS2723B.aspx”. In: ().

[181] J. Álvarez-Muñiz, A Berlin, et al. “Search for microwave emission from ultrahigh energy cosmic rays”. In: *Physical Review D* 86.5 (Sept. 2012), 051104 EP –.

[182] A. Letessier-Selvon, P. Billoir, et al. “Layered water Cherenkov detector for the study of ultra high energy cosmic rays”. In: *Nuclear Instruments and Methods in Physics Research A* A767 (2014), pp. 41–49.

[183] M. Ave, R. Engel, et al. “Extensive Air Shower Universality of Ground Particle Distributions”. In: *International Cosmic Ray Conference*. 2011, pp. 1–4.

[184] D. Maurel, M. Roth, and J. Gonzalez. “Universality of the time structure of ground particle distributions and its application to the reconstruction of extensive air showers”. In: *International Cosmic Ray Conference*. June 2013, pp. 1–4.

[185] T. Abu-Zayyad, R. Aida, et al. “The Cosmic-Ray Energy Spectrum Observed with the Surface Detector of the Telescope Array Experiment”. In: *The Astrophysical Journal Letters* 768.1 (2013), p. L1.

[186] A. Cadiou, C. Carduner, et al. “Tank Separators for the LSD Upgrade”. In: *Auger GAP Note* 2014-057 (June 2014), pp. 1–23.

[187] H. Röttgering. “LOFAR, a new low frequency radio telescope”. In: *New Astronomy Reviews* 47.4-5 (Sept. 2003), pp. 405–409.

[188] A. A. Ivanov, S. P. Knurenko, and I. Y. Sleptsov. "The energy spectrum of cosmic rays above 1015 eV derived from air Cherenkov light measurements in Yakutsk". In: *Nuclear Physics B - Proceedings Supplements* 122.0 (July 2003), pp. 226–230.

[189] M. Conde, W. Gai, et al. "Argonne Wakefield Accelerator Facility Upgrade". In: *Conf.Proc.* C0106181 (2001), pp. 3957–3959.

[190] R. Smída, H. Bluemer, et al. "First results of the CROME experiment". In: *International Cosmic Ray Conference*. Beijing, 2011.

List of Figures

List of Tables

Index

Acronyms and definitions

General acronyms

EAS extensive air shower

LDF lateral distribution function

UHE ultra-high energy

CR cosmic ray

UHECR ultra-high energy cosmic ray

HAS horizontal air shower

PMT photomultiplier tube

NKG Nishimura-Kamata-Greisen

VEM vertical equivalent muon

rms root mean square

T1 first level trigger

T2 second level trigger

T3 CDAS trigger

T4 physics trigger

T5 quality trigger

TH threshold trigger

ToT time-over-threshold trigger

HG high gain

LG low gain

UV ultraviolet

IR infrared

GZK Greisen [101], Zatsepin and Kuzmin [102]

MC Monte Carlo

MBR Molecular Bremsstrahlung Radiation

FADC flash analog digital converter

CDAS central data acquisition system

CMB cosmic microwave background [100]

RF radio frequency

electromagnetic electromagnetic

MIP minimum ionizing particle: particles that have mean energy loss rates close to the minimum. Cosmic ray muons are MIP's

PVC poly(vinyl chloride)

LNA low noise amplifier

HFSS high frequency structural simulator

SNR signal-to-noise ratio

AGN Active Galactic Nucleus

GRB Gamma-ray burst

FoV field of view

pe photoelectron

CL confidence level

LDA linear discriminant analysis

$\vec{w}$ vector normal to the discriminant hyperplane

KS Kolmogorov-Smirnov

D_{KS} maximum KS distance

ECDF empirical cumulative distribution function

VCV Veron-Cetty & Veron

GPS Global Positioning System

ES Earth-skimming

DGH downward-going high angle

DGL downward-going low angle

AoP area over peak

CIC constant intensity cut

Hadronic interaction models and simulation codes

HIM hadronic interaction model

Sybill 2.1 Sybill 2.1 [30]

QGSJet01 QGSJet01

QGSJet-II-03 QGSJet-II-03 [31–33]

QGSJet-II-04 QGSJet-II-04 [31–33]

EPOS LHC EPOS LHC [34]

EPOS 1.99 EPOS 1.99

AIRES AIR shower Extended Simulations [35]

CORSIKA COsmic Ray SImulations for KAscade [36]

FLUKA A Multi-Particle Transport Code [37]

GEANT4 GEANT4 [38, 39]

Detectors, observatories, experiments and institutions

SD surface detector array

FD fluorescence detector

WCD water Cherenkov detector

Giga Duck Giga Duck. Project to measure extensive air shower radio signal between 1.05 and 1.45 GHz

EASIER Extensive Air Shower Identification using Electron Radiometer [69]

CLF Central Laser Facility [75]

XLF eXtreme Laser Facility [75]

ISS International Space Station

ICRC International Cosmic Ray Conference

Auger Pierre Auger Observatory [44]

Auger Collaboration Pierre Auger Collaboration

HEAT High Elevation Auger Telescopes [80]

VERITAS Very Energetic Radiation Imaging Telescope Array System [52]

MAGIC Major Atmospheric Gamma-ray Imaging Cherenkov Telescopes [53]

HESS High Energy Stereoscopic System [51]

TA Telescope Array [47]

Fly's Eye Fly's Eye [59]

HiRes High Resolution Fly's Eye [60]

ASHRA All-sky Survey High Resolution Air-shower Detector [58]

JEM-EUSO Extreme Universe Space Observatory [61]

HAWC High Altitude Water Cherenkov [45]

AGASA Akeno Giant Air Shower Array [46]

LHAASO Large High Altitude Air Shower Observatory [48]

CODALEMA COsmic ray Detection Array with Logarithmic ElectroMagnetic Antennas [62]

LOPES LOFAR PrototypE Station [63]

LOFAR Low Frequency ARray [187]

AERA Auger Engineering Radio Array [64]

RICE Radio Ice Cherenkov Experiment [65]

ANITA Antarctic Impulsive Transient Antenna [66]

ARIANNA Antarctic Ross Ice-Shelf ANtenna Neutrino Array [67]

ARA Askaryan Radio Array [68]

CTA Cherenkov Telescope Array [54]

Ice-Cube Ice-Cube [55]

ANTARES Astronomy with a Neutrino Telescope and Abyss environmental RESearch project [56]

LHC Large Hadron Collider

KASCADE KArlsruhe Shower Core and Array DEtector [92]

KASCADE-Grande KASCADE-Grande. Extension of KASCADE experiment [93]

Tunka-133 Tunka-133. EAS Cherenkov light array at the Tunka Valley [50]

IceTop IceTop. A surface component of the IceCube Neutrino Observatory [94]

Yakutsk Yakutsk [188]

AMBER Air Shower MicroWave Bremsstrahlung Experimental Radiometer [82]

MIDAS MIcrowave Detection of Air Showers [83, 84]

AMY Air Microwave Yield [169]

BTF Beam Test Facility, at Laboratori Nazionali di Frascati (LNF)

MAYBE Microwave Air Yield Beam Experiment [168]

LSD Layered Surface Detector [182]

AWA Argonne Wakefield Accelerator Facility [189]

SLAC SLAC National Accelerator Laboratory, originally named Stanford Linear Accelerator Center

CROME Cosmic Ray Observation via Microwave Emission [190]

LPNHE Laboratoire de Physique Nucléaire et des Hautes Énergies

AMIGA Auger Muon and Infill for the Ground Array [81]

Variables and observables

S station signal. Average signal measured by the PMTs of the station.

axis axis. Line in the atmosphere that defines the center of the extensive air shower. The direction of the shower axis is calculated using the differences of time between the detectors.

r distance to the axis. Distance between the individual station and the axis of the extensive air shower

$N_{\max}$ maximum size

$X_{\max}$ atmospheric depth of maximum

$\sigma(X_{\max})$ dispersion of the atmospheric depth of maximum

$X^{\mu}_{\max}$ muonic atmospheric depth of maximum

MPD muon production depth

D_{10} elongation rate

S_{1000} average signal at 1000 m

S_{38} average signal at 1000 m that the extensive air shower would have produced if it had arrived at the median zenith angle of 38°

E energy

E_{sim} simulated energy

E_{μ} muon energy

θ arrival zenithal angle

φ arrival azimuthal angle

ϕ angle of the footprint main axis

λ lateral extension

α angular distortion

$\Delta\alpha$ deviation of α from the expected value

$X_{\mathrm{c}}, Y_{\mathrm{c}}$ core position

$B_{\perp}$ perpendicular magnetic field

P_{T} transverse momentum

T_{1400} signal start-time at 1400 m

S^{μ}_{1000} average muon signal at 1000 m

N^{μ}_{1000} average muon number at 1000 m

E_0 initial energy

E_{c} critical energy: the energy where the two losing mechanism are equal

E^{π}_{c} critical energy for pions

E_{cal} calorimetric energy

δ transverse displacement

L_{μ} path from production to the ground

ζ azimuthal angle in the shower plane

L length

W width

β shock velocity

R_{M} Molière radius. Is the root mean square distance that an electron at the critical energy is scattered as it traverses one radiation length. A cylinder with this radius holds the 90% of the energy of the extensive air shower; $R_{\mathrm{M}} = X_0 E_{\mathrm{S}}/E_{\mathrm{c}}$ [27]

E_{S} Scale energy; $E_{\mathrm{S}} = \sqrt{4\pi/\alpha} m_e c^2 = 21.2052\,\mathrm{MeV}$ [27]

X_0 radiation length: (1) the mean distance over which a high energy electron loses all but 1/e of its energy; (2) 7/9 of the mean free path for pair production by a high energy photon; $X_0(air) = 36.62\,\mathrm{g/cm^2}$ [27]

λ_I nuclear interaction length; $\lambda_I^{air} = 90.1\,\mathrm{g/cm^2}$ [27]

λ_{π} pion interaction length; $\lambda_{\pi}^{air} = 122.0\,\mathrm{g/cm^2}$ [27]

S_{top} signal in the top liner

S_{bot} signal in the bottom liner

S_{em} electromagnetic signal

S_{μ} muonic signal

N_{μ} muon number

MF merit factor

$\mathbf{S}_{\mathrm{fisher}}$ Fisher separation coefficient

N_{19} relative scale factor

$\mathbf{W}_{\mathrm{m}}$ multi-dimensional parameter